Transient Dynamics of Continuous Systems with Impact and Friction, with Applications to Musical Instruments

by

Chandrika Prakash Vyasarayani

A thesis
presented to the University of Waterloo
in fulfilment of the
thesis requirement for the degree of
Doctor of Philosophy
in
Systems Design Engineering

Waterloo, Ontario, Canada, 2009

I hereby declare that I am the sole author of this thesis. This is a true copy of the thesis, including any required final revisions, as accepted by my examiners.

I understand that my thesis may be made electronically available to the public.

Abstract

The objective of this work is to develop mathematical simulation models for predicting the transient behaviour of strings and beams subjected to impacts. The developed models are applied to study the dynamics of the piano and the sitar.

For simulating rigid point impacts on continuous systems, a new method is proposed based on the unit impulse response. The developed method allows one to relate modal velocities before and after impact, without requiring the integration of the system equations of motion during impact. The proposed method has been used to model the impact of a pinned-pinned beam with a rigid obstacle. Numerical simulations are presented to illustrate the inability of the collocation-based coefficient of restitution method to predict an accurate and energy-consistent response. The results using the unit-impulse-based coefficient of restitution method are also compared to those obtained with a penalty approach,with good agreement.

A new moving boundary formulation is presented to simulate wrapping contacts in continuous systems impacting rigid distributed obstacles. The free vibration response of an ideal string impacting a distributed parabolic obstacle located at its boundary is analyzed to understand and simulate a sitar string. The portion of the string in contact with the obstacle is governed by a different partial differential equation (PDE) from the free portion represented by the classical string equation. These two PDEs and corresponding boundary conditions, along with the transversality condition that governs the dynamics of the moving boundary, are obtained using Hamilton's principle. A Galerkin approximation is used to convert them into a system of nonlinear ordinary differential equations, with time-dependent mode-shapes as basis functions. The advantages and disadvantages of the proposed method are discussed in comparison to the penalty approach for simulating wrapping contacts. Finally, the model is used to investigate the mechanism behind the generation of the buzzing tone in a sitar. An alternate formulation using the penalty approach is also proposed, and the results are contrasted with those obtained using the moving boundary approach.

A model for studying the interaction between a flexible beam and a string at a point including friction has also been developed. This model is used to study the interaction between a piano hammer and the string. A realistic model of the piano hammer-string interaction must

treat both the action mechanism and the string. An elastic stiff string model is integrated with a dynamic model of a compliant piano action mechanism with a flexible hammer shank. Simulations have been used to compare the mechanism response for impact on an elastic string and a rigid stop. Hammer head scuffing along the string, as well as length of time in contact, were found to increase where an elastic string was used, while hammer shank vibration amplitude and peak contact force decreased. Introducing hammer-string friction decreases the duration of contact and reduces the extent of scuffing. Finally, significant differences in hammer and string motion were predicted for a highly flexible hammer shank. Initial contact time and location, length of contact period, peak contact force, hammer vibration amplitude, scuffing extent, and string spectral content were all influenced.

Acknowledgements

Guru (teacher) himself is the Lord Brahma,
Lord Vishnu, and the Lord Shiva (the divine trinity).
He is verily the very transcendental divinity.
My reverential salutations to that glorious teacher.

–Ancient Sanskrit hymn

I would like to acknowledge my supervisors, Stephen Birkett and John McPhee, for their guidance and support. I am thankful to NSERC, Steinway and Sons, and the University of Waterloo for providing me with financial support for my doctoral studies. I would like to thank all the teachers who taught me and have contributed directly to my knowledge.

My friends Tom Uchida and Sukhpreet Sandhu are specially thanked for their continuous encouragement, and for their help in proof-reading several manuscripts that were written during the course of the study.

I thank Eihab Abdel-Rahman, Anindya Chaterrjee, Kingshook Bhattacharyya, and Thangaraj Draviam for the informal discussions I had with them on the subject of impact modelling.

I would like to thank my friends Krishnam Raju Jampani, Murthi Ganti, Ramesh Periasamy, and Varma Nadimpalli, who gave me words of advice and courage during tough times.

I am also thankful to my fellow students in the Motion Research Group for creating a stimulating research environment.

Dedication

Dedicated to my mother **V. Bhagya Lakshmi**.

Contents

List of Figures

List of Tables

Nomenclature

α	Non-dimensional height of the parabolic obstacle
$\beta_k(\tau)$	Modal coordinate for the k^{th} mode of the string during phase-II motion
Δ	Compression in felt
δ	Variation
$\delta_d(\ )$	Dirac's delta function
δ_{jk}	Kroneker's delta
$\dot{(\ )}$	Time derivative of $(\ )$
$\eta_k(\tau)$	Modal coordinate for the k^{th} mode of the string during phase-I motion
Γ	Location of moving boundary
γ	Non-dimensional location of moving boundary
Γ_1	Left termination point of string on the parabolic obstacle
Γ_2	Right termination point of the string on the parabolic obstacle
Λ	Damping coefficient in distribued contact model
λ	Damping parameter in contact model
μ	Coefficient of friction between string and piano hammer
ω^*	Frequency of the external excitation

ω_{1k} Non-dimensional natural frequency for the k^{th} mode of string during phase-I motion

$\omega_{2k}(\tau)$ Time dependent natural frequency for the k^{th} mode of string during phase-II motion

ω_{3k} Non-dimensional natural frequency for the k^{th} mode of the string during phase-III motion

ω_j Natural frequency for the j^{th} mode of the beam

$\phi_k(x)$ Mode shape function for the k^{th} mode of the string during during phase-I motion

Π Lagrangian density

ψ_k k^{th} time dependent basis function used in representing phase-II motion

ρ Density

τ Non-dimensional time

τ_{c1} Time of switchging between phase-I to phase-II motion

τ_{c2} Time of switchging between phase-II to phase-III motion

τ_{c3} Time of switchging between phase-III to phase-II motion

τ_{c4} Time of switchging between phase-II to phase-I motion

$\triangle$ Non-dimensional energy of the beam

φ_k Mode shape function for the k^{th} mode of the string during phase-III motion

ξ_j Modal damping in string

A Area of cross-section

A_1 Parameter in friction model for felt

a_f Parameter in force-compression model for felt

A_p Constant to control the shape of parabola

B Width of the parabolic obstacle

b Non-dimensional width of the parabolic obstacle

B_1 Parameter in friction model for felt

B_2 Parameter in friction model for felt

b_f Parameter in force-compression model for felt

c_f Parameter in force-compression model for felt

D Gap between the beam and the obstacle

d_f Damping parameter in force-compression model for felt

E Young's modulus

E_h Young's modulus of piano hammer

F Non-dimensional amplitude of the forcing function

F^* Amplitude of the forcing function

$G()$ Gap function

h Non-dimensional height of the obstacle

I Area moment of inertia of cross-section

K Penalty parameter

L Length of the beam/string

n Exponent of nonlinearity in the compliance of distribued contact model

P Non-dimensional impulse force on the beam

$q_j(\tau)$ Modal coordinate of the j^{th} mode for the beam

R Coefficient of restitution

$r(\tau)$ Modal coordinate for the k^{th} mode of the string during phase-II1 motion

T Tension in the string

t Time

$W_j(x)$ Mode shape function for the j^{th} mode of the beam

X coordinate along the length of the beam or string

X_f Location of the forcing function along the length of the beam

X_i Location of the rigid obstacle along the length of the beam

x_{ck} Location of k^th collocation point along the length of the beam

Y_1 Deflection of string during phase-I motion

y_1 Non-dimensional deflection of the string during phase-I motion

Y_2 Deflection of string during phase-II motion

y_2 Non-dimensional deflection of the string during phase-II motion

Y_3 Deflection of string about the static equilibrium in phase-II motion

y_3 Non-dimensional deflection of the string about static equilibrium in phase-II motion

Y_4 Deflection of string during phase-III motion

y_4 Non-dimensional deflection of the string during phase-III motion

Y_B Function defining the shape of the parabola

y_B Dimensionless function defining the shape of the parabola

Z Vertical deflection of the beam

Chapter 1

Introduction

Many mechanical systems are subjected to impact loading, either due to their functionality (such as musical instruments, impact dampers, impact hammers, and sports equipment) or due to undesirable phenomena (such as clearance in joints due to wear and rotor-stator impact in rotating machinery). The modelling and simulation of such mechanical systems provides an understanding of their dynamic behaviour, and can assist the engineer in developing better products. The main objective of this research is to develop mathematical models to simulate impacts with or without friction on unidirectional continuous systems (i.e., systems with one independent spatial coordinate) using the modal-based approach. The developed models are used to study the impact behaviour of strings and beams, with applications to musical instruments.

1.1 Background

Continuous systems have an infinite number of degrees of freedom. In reality, all mechanical systems are continuous in nature, and elastic waves are initiated when they are subjected to impacts. The generation of such waves is particularly apparent in highly flexible rods (strings, slender beams, and cables). Since we are mainly focusing on the impact dynamics of uniform slender elastic rods, we exclude the finite element method (FEM) and instead consider global methods using undamped mode shapes as the basis functions for representing their motion.

1.1.1 Modelling point contacts in continuous systems

Three approaches are generally employed for modelling contacts in continuous systems: the coefficient of restitution (CoR) approach, the local compliance approach, and the boundary switching approach. The CoR approach assumes that the impact occurs within an infinitesimal amount of time, and thereby assumes that the configuration of the system is the same immediately before and immediately after impact. The post-impact initial conditions are obtained using momentum and/or energy balance equations. This approach has gained popularity due to its simplicity. Figure 1.1 shows two flexible translating bodies impacting at location P and the direction of their rigid-body velocities before and after impact. In highly flexible structures, the impacts occur in finite time. Since significant deformations can occur during the impact phase, use of the CoR approach is inappropriate in this case.

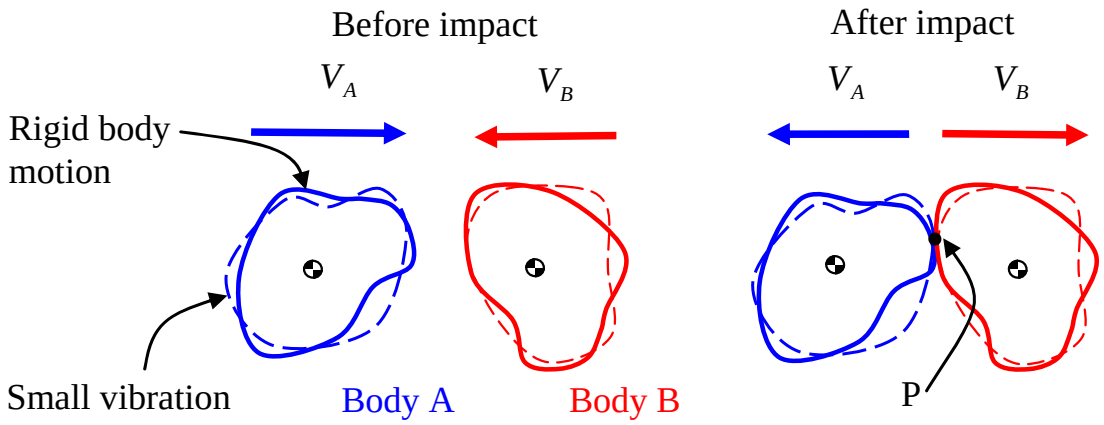

Figure 1.1: Illustration of coefficient of restitution approach.

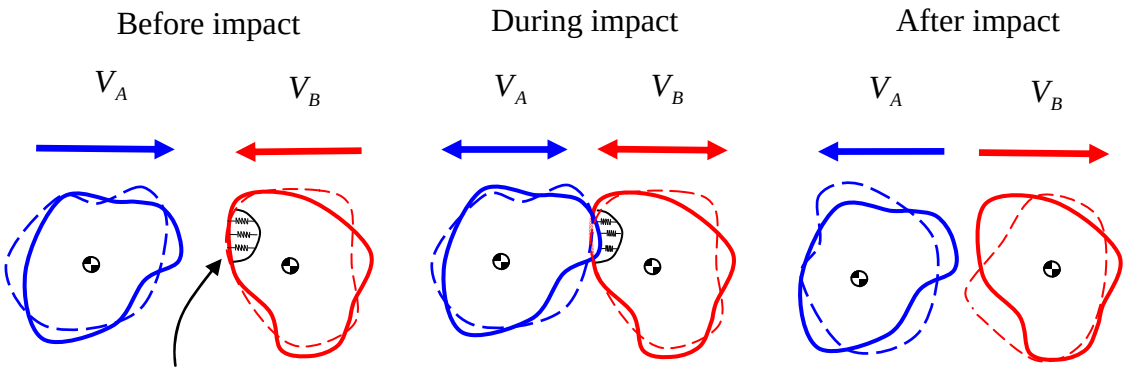

Figure 1.2: Illustration of local compliance approach.

The second approach involves modelling the local contact compliance, as shown in Figure 1.2. When the two bodies come in contact with each other, forces are generated as one body penetrates into the other. This approach requires the integration of the governing equations of motion over the impact phase. Whereas the CoR approach does not provide any insight into the forces generated during impact, the local compliance approach can be used to estimate the contact forces involved in a postprocessing step.

The last approach involves switching between models with different boundary conditions during impact. Figure 1.3 shows a fixed-free beam impacting a point obstacle at its free end. The beam boundary conditions can be considered fixed-free during non-contact phase and fixed-pinned during contact phase. Once the impact occurs, the displacement and velocity distributions of the fixed-free beam are used as initial conditions for the beam model with fixed-pinned boundary conditions. The loss of contact occurs when the reaction force at the pinned end approaches zero. This method completely neglects local compliance and assumes that the global motion is responsible for contact initiation and termination.

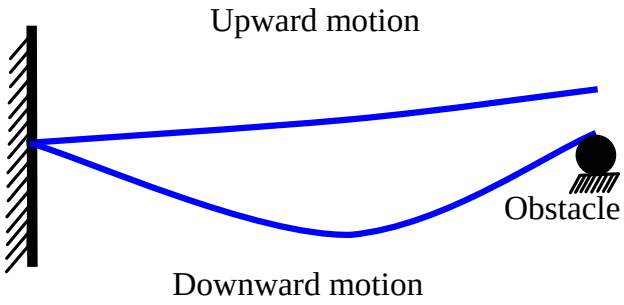

Figure 1.3: Illustration of mode switching approach.

1.1.2 Modelling distributed contacts in continuous systems

It is relatively simple to model point contacts in flexible systems at predefined locations; however, the contact locations are not known a priori in most applications. Many applications involve distributed contacts in which multiple impacts can occur simultaneously at different locations, as shown in Figure 1.4. The beams shown in Figure 1.4 can impact under base-excited motion. This simple mechanical system is a basic model of a heat exchanger, where the tubes

impact each other under fluid-induced vibrations. One approach to model distributed impacts is to assume a distributed compliance function along the normal direction of contact. Damping can also be introduced into the contact model to account for losses during impact.

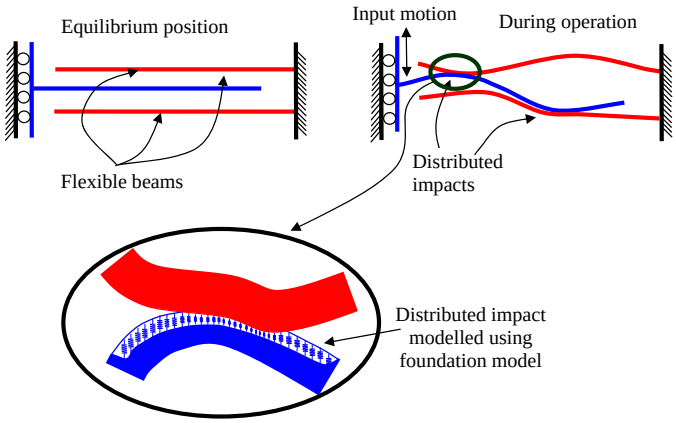

Figure 1.4: Illustration of local compliance approach for distributed impacts.

In special circumstances, a moving boundary formulation can be employed to model wrapping distributed contacts. Wrapping contacts occur when the continuum is vibrating in its lower modes and impacts an obstacle. As an example, Figure 1.5 shows a cantilever beam wrapping against a cylindrical obstacle at its boundary. The motion of the beam during contact can be formulated as a moving boundary problem.

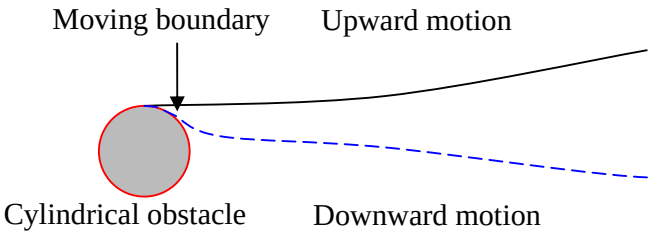

Figure 1.5: Illustration of moving boundary approach.

1.2 Impact modelling in musical instruments

Impact and friction are the basic mechanisms used for tone generation in percussion instruments; Figure 1.6 illustrates the flow of energy in these instruments. The impacts need to be

modelled in as much detail as possible, since this is the main mechanism of energy transfer between the musician and the instrument. Impact is used to excite strings, rods, beams, or membranes, which are attached to a soundboard through a bridge. The soundboard then radiates the sound that is heard by the human ear. The mathematical models developed in this thesis will be used to study the mechanism of tone generation in the piano and sitar. Musical instruments are generally built based on years of experience, and have very subtle designs. Several centuries of design evolution based on intuition makes musical instruments complicated objects for mathematical modelling. The materials used in their construction are also difficult to model: several instruments use bone, leather, hair, and felt along with wood. Felt is widely used in musical instruments as the impacting interface, as in piano hammers and drum mallets. The contact evolution in these instruments during an impact is dependent on both space (the contact location is not known in advance) and time, and is a very complicated process. Traveling waves that are generated during the initial phase of contact travel to the boundary and are reflected back, interacting with the impacting body.

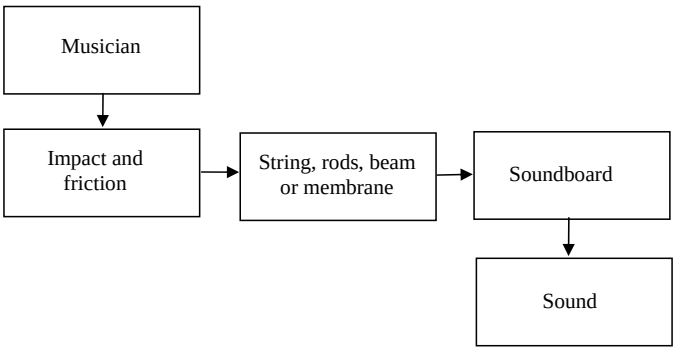

Figure 1.6: Energy flow in musical instruments.

1.2.1 Hammer-string interaction in piano

The action mechanism in a piano converts a mechanical input at the key into motion of the hammer, which then impacts the string to generate sound. A typical configuration of a modern grand (horizontal) piano action is shown in Figure 1.7, and consists of five main components: key, whippen, repetition lever, jack, and hammer. The components of this mechanism interact through felt-lined interfaces providing compliant, and possibly intermittent, contact locations

with friction and damping. Some of these contacts are perfectly transverse and some are oblique. The mechanical properties of the felt will influence the damping of vibrations present in the action components due to their flexibility, as well as the transient vibrations that arise when components separate and re-contact during the operation of the mechanism.

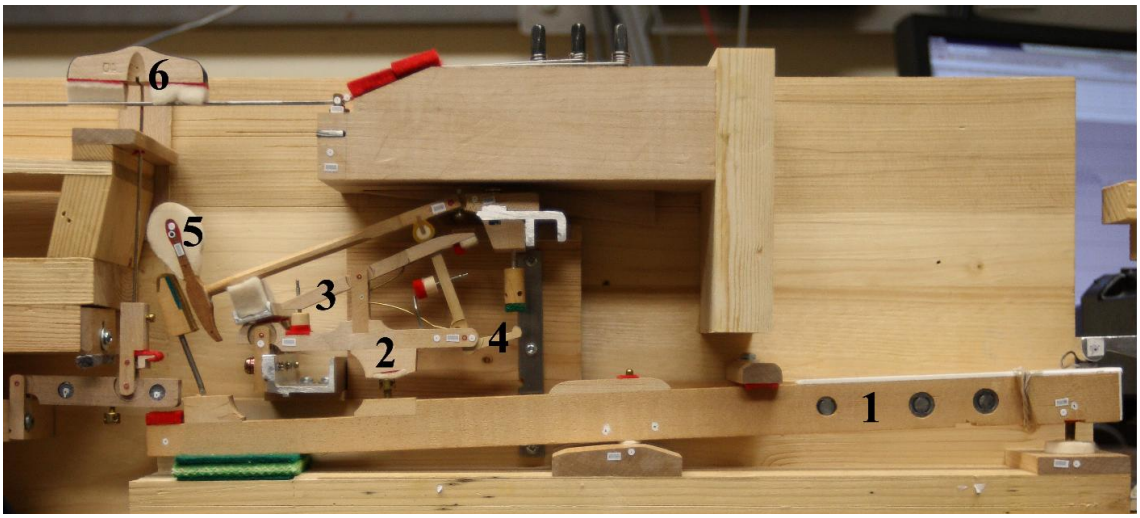

Figure 1.7: Typical modern grand piano action mechanism: key (1), whippen (2), repetition lever (3), jack (4), hammer (5), damper (6).

The driving force on the hammer is transmitted through the jack under the knuckle. Immediately before the hammer impacts the string, the jack is mechanically forced to lose contact with the hammer (called escapement or let-off) so the vibrations generated on the string through the impact will not be immediately damped by the action mechanism.

1.2.2 Bridge-string interaction in sitar

The sitar (see Figure 1.8) is a musical instrument of Indian origin whose plucked strings can interact with a shallow curved ledge located beneath the vibrating strings (see Figure 1.9). The bridge, which includes the ledge as well as grooves to constrain the strings to their evenly-spaced lateral positions for playing, is typically carved from a piece of bone and rests on small wooden feet in contact with the soundboard of the instrument. The tone of the sitar, and other instruments of Indian origin with a similar bridge design (such as the veena and tambura), is markedly different from that of other plucked stringed instruments like the guitar. The

Figure 1.8: The sitar, a stringed instrument of Indian origin.

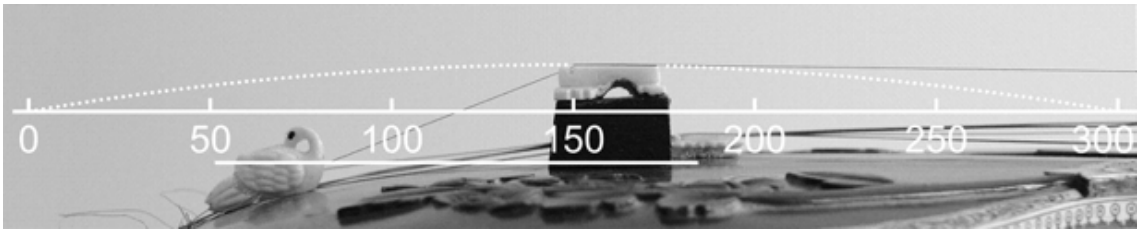

Figure 1.9: The sitar bridge is approximately parabolic.

.

interaction of the string with the bridge generates high-frequency components and creates a characteristic buzzing sound.

This mechanism of sound generation can also be found in Western instruments. The Medieval and Renaissance bray harp, for example, has small bray-pins that provide a metal surface for the vibrating strings to impact near their termination points, increasing the upper partial content in the tone and providing a means for the harp to be audible in larger spaces and in ensemble with other instruments [28]. The arpichordium stop, common on some virginals (plucked string keyboard instruments), imitates the bray harp, using soft metal (lead or brass) pins that can be bent so as to lie close to the vibrating strings (about 15 mm from the termination point) [56].

The distinctive buzzing sound common to all of these instruments is caused by the presence of a physical obstacle that alters the behaviour of a vibrating string by interacting with it close to one of its termination points.

1.3 Organization of this thesis

The second chapter begins with a literature review on general approaches for simulating point contacts in continuous systems using the modal-based approach (Section 2.1). Sections 2.2 and 2.3 discuss the work done by earlier researchers on the bridge-string interaction in a sitar and the hammer-string interaction in a piano. . Chapter 3 presents a new and energy-consistent method for simulating point impacts in continuous systems using a coefficient of restitution. The advantages of the proposed method over existing coefficient of restitution methods are discussed. The simulations obtained using the proposed method to simulate a base- excited cantilever system are compared with the experimental results published in the literature. In Chapter 4, the distributed contact problem of a string impacting a rigid obstacle at its boundary is studied. The developed model is applied to study the mechanism of tone generation of the sitar. Chapter 5 describes the mathematical modelling of, and numerical simulation results for, a complete multibody dynamic model of the piano action mechanism with 1D stiff string contact. Finally, Chapter 6 outlines the major conclusions.

Chapter 2

Literature review

In this chapter, we briefly review the literature dealing with the following problems:

(i) Modelling the impact of a continuous system with a rigid point obstacle;

(ii) Modelling the impact of a continuous system with a rigid distributed obstacle and its application to the bridge-string interaction in a sitar; and

(iii) Modelling the impact between a compliant multibody system and a continuous system in the presence of friction, with an application to the hammer-string interaction in a piano.

2.1 Modelling the impact of a continuous system with a rigid point obstacle

The dynamics of beams, strings, and rods subjected to impacts caused by motion-limiting constraints has been studied extensively. An incomplete but illustrative analysis can be found in [8, 22–24, 26, 48, 50, 54, 61, 68, 69, 72–75, 77, 78]. Three different approaches have been employed to model the problem:

1. Force integration method (also referred to as the penalty approach) [8, 22, 48, 50, 54, 68, 69, 77, 78]: In this method, a contact force proportional to the penetration of the beam

at the contact point is applied at the contact location. This method can be used to model linear or nonlinear stiffness in the obstacles.

2. Mode switching method [23, 26, 63, 68]: In this method, the mode shapes of the continuous system are evaluated when it is in contact with the obstacle, and are used as the basis for representing the motion of the system during contact. Since a prior evaluation of mode shapes is necessary to model the contact, this method is only applicable to linear system models.

3. CoR method: This approach is based on the coefficient of restitution (CoR) method, which treats the obstacle as rigid, and has been proposed by Wagg and Bishop [72–75].

Despite the success of modelling short-duration impacts in flexible multibody systems using the CoR approach, the extension of CoR-based modelling to structural systems has received little attention, especially when combined with modal discretization. The only work in this area was done by Wagg and Bishop [75], who comment in their work that the CoR theory can be applied to a continuous system when the impact is of very short duration, such as with metal impacting components. They proposed a modal form of CoR (MoCoR) that relates the pre-impact and post-impact velocities for beams, making two assumptions:

1. The configuration of the system does not change during the impact, in accordance with the conventional rigid-body CoR approach; and

2. The velocity field of the structure changes only at the impacting point according to the CoR method, setting up a non-smooth velocity field after impact.

Using the above assumptions, Wagg and Bishop defined a modal form of CoR that relates the post-impact modal velocities to the pre-impact modal velocities. For an N-mode approximation, the modal form of CoR requires selecting $N-1$ locations (the collocation points) on the beam at which the velocities are assumed to be the same before and after the impact. The authors have approximated the assumed non-smooth post-impact velocity distribution of the beam using a function (the collocation function), which is a linear combination of the N mode shapes. The coefficients of the collocation function are obtained by equating it to the corresponding non-smooth function at the collocation and impact points. From numerical simulations, we have

observed that the MoCoR approach, in its current form, adds energy into the structure that is being impacted for certain simulation parameters (collocation points). To resolve this issue, we develop a new MoCoR approach that does not involve choosing collocation points. The developed method is also energy-consistent, as explained in Chapter 3.

2.2 Bridge-string interaction in the sitar

Raman [59] gives a detailed description of the bridge geometry used for the sitar, veena, and tambura. He notes that even if a veena string is plucked at a node, the corresponding vibration mode appears in the response. Raman concludes that this phenomenon is a consequence of the interaction of the string with the bridge. Various approaches for modelling the interaction between a vibrating string and an obstacle have been presented in the literature. Amerio and Prouse [3], Schatzman [60], Burridge et al. [12], and Cabannes [13–15] used the method of characteristics and energy conservation for simulating the impact between a string and a rigid obstacle. Cabannes [15] notes that the case of modelling a string not initially at rest is an open problem when using a travelling wave approach. Ahn [2] used a finite element approach and Newton's kinetic coefficient of restitution to simulate the string and its impact with the bridge. Han and Grosenbaugh [39] and Taguti [67] simulated the impact using a penalty approach combined with finite difference discretization for the string motion, while Vyasarayani et al. [71] used the penalty approach with a modal representation of the string motion. A different direction was taken by Krishnaswamy and Smith [49], who model the curved sitar bridge as a point obstacle and apply digital wave-guides (signal processing methods) and finite difference methods to obtain the solution for a rigid impact. Valette [70] analyzes the dynamics of a tambura string interacting with a distributed obstacle that is modelled as a unilateral point constraint, and assumes completely plastic impact.[1]

The objective of this study is to developed a mathematical model that can be used to understand the mechanism behind the tone generation in a sitar. A new modal formulation is developed to simulate distributed wrapping contacts in continuous systems, which is presented in Chapter 4. When the obstacle is located near the termination of the vibrating continuum,

[1] In the literature, a perfectly wrapped string is often described as a completely plastic impact.

it is possible to model the interaction dynamics as a moving boundary problem. Fung and Chen [29] proposed this method and studied perfect wrapping of a flexible cantilever beam on a circular rigid foundation as a moving boundary problem. The sitar bridge-string problem is closely related to this work, but differs from it in several respects: (i) the vibrating continuum is a string rather than a beam; (ii) the string can have a non-point contact length at static equilibrium; (iii) the contacting boundary is of finite length, thus limiting the maximum amount of wrapping around the obstacle; and (iv) the obstacle geometry is closer to a parabola than a circle.

2.3 Hammer-string impact in the piano

As mentioned in Section 1.21, the piano hammer loses contact with the action mechanism (escapement) just before its impact with the string. Many authors [7, 9, 17, 18, 34–38, 66] have exploited this fact and modelled the hammer as a single-degree-of-freedom translating mass with nonlinear compliance, thus assuming perfect normal impact between the string and the hammer. In reality, the hammer shank (the component on which the hammer is mounted) is a rotating slender beam, so the hammer follows a circular trajectory, not a linear one. Moreover, small vibrations are superimposed on its motion due, in part, to the flexibility of the shank and the compressibility of the felt contacts. The influence of these effects on string motion [5], contact force [30], and action mechanism dynamics [47] have been emphasized in the literature. The hammer-string contact modelling literature [7, 9, 17, 18, 34–38, 66] ignores any effects due to hammer shank flexibility and action compressibility; the only simulation model which includes hammer shank flexibility [47] neglects string dynamics, substituting a rigid stop for the hammer to impact. In this research, we investigate the dynamic significance of flexibility by integrating models of an action mechanism with a flexible hammer shank [47] and an elastic stiff piano string.

Hirschkorn et al. [42] developed a multibody dynamic model of the action mechanism considering all the components as rotating rigid bodies. A detailed review of earlier action mechanism models was also reported, with the conclusion that none of the existing models are sufficiently realistic nor mechanistic enough to be useful for prototyping purposes. Parameters

in the earlier models were tuned to obtain the observed hammer motion and could not be associated with physical measurements of action components. Izadbakhsh et al. [47] extended the Hirshkorn et al. [42] model by including hammer shank flexibility. In both these models, string dynamics are neglected and the hammer impacts a rigid obstacle in place of a string. The development of a simulation model for analysis and design of piano actions, one of the goals of this research, demands a complete multibody dynamic model of the mechanism with string contact. This model will be used to support several future objectives of the Piano Design Lab at the University of Waterloo, including the following:

- To design and develop a new mechanacoustic piano at a low cost. In the process of designing a new piano, it is important to analyze the dynamics of existing designs; the new design should have at least the same dynamic capability as traditional pianos. A realistic simulation model is required to study the behaviour of existing piano actions.
- To study the biomechanical aspects of the pianist, and to understand the controllability of the instrument by the pianist.
- To develop a simulation model that can be used by the industrial sponsor, Steinway and Sons, for their analysis and design of piano action mechanisms.

In order to include a realistic hammer-string interaction, the action mechanism and string must be dealt with as a single system. This is necessary so that the effect on system response due to changing physical parameters of the mechanism and/or string may be examined. In general, there will be tonal changes, characterized by different partials generated on the string, as well as changes in the dynamic behaviour of the components of the mechanism (presented in Chapter 5). To understand the influence of the string on the dynamic response of the action mechanism and vice versa, we integrate the stiff string model proposed by Fletcher [27] with the flexible action mechanism model presented in Izadbakhsh et al. [47], thus filling the gap between the single-degree-of-freedom hammer-string interaction models [7, 9, 17, 18, 34–38, 66] and dynamic piano action mechanism models with rigid contacts [42, 47].

Chapter 3

Modelling the dynamics of a continuous system impacting a rigid point obstacle

This chapter begins with the mathematical modelling of an Euler-Bernoulli beam impacting a rigid point obstacle. First, we model the impact using an existing collocation method. The disadvantages of the collocation method are discussed. A new method based on the unit-impulse response is then proposed. Numerical simulations are presented to demonstrate the effectiveness of the proposed method, and a comparison with the penalty approach is presented. Finally, some qualitative comparisons are made between simulations and existing experimental results.

3.1 Mathematical modelling

The schematic of the physical system being modelled and the related nomenclature is shown in Figure 3.1. The system consists of a pinned-pinned beam excited harmonically at location X_f by a force $F^* \sin(\omega^* t)$. The motion of the beam is constrained by a rigid stop at location X_i. The equation governing the dynamics of the beam, excluding the event of impact and assuming Euler-Bernoulli beam theory, is given by the following:

$$EI\frac{\partial^4 Z}{\partial X^4} + \rho A\frac{\partial^2 Z}{\partial t^2} = F^* \sin(\omega^* t)\delta_d(X - X_f), \quad Z(X_i, t) \leq D \tag{3.1}$$

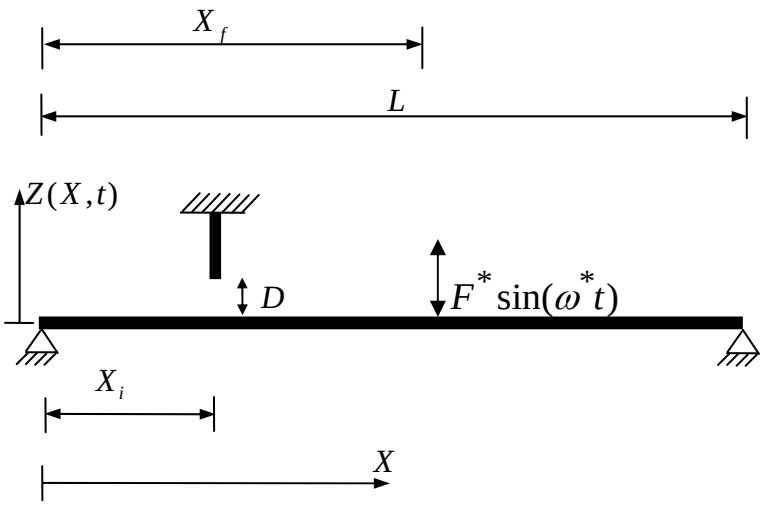

Figure 3.1: Schematic of the physical system.

where E is the Young's modulus, I is the area moment of inertia, ρ is the density, A is the cross-sectional area, δ_d is Dirac's delta function, and t is time. The boundary conditions for pinned-pinned supports are as follows:

$$Z(0,t) = Z(L,t) = 0 \quad \text{and} \quad \frac{\partial^2 Z(0,t)}{\partial X^2} = \frac{\partial^2 Z(L,t)}{\partial X^2} = 0 \tag{3.2}$$

We introduce the following dimensionless parameters into the equation of motion:

$$x = \frac{X}{L},\ \ w = \frac{Z}{D},\ \ \tau = t\sqrt{\frac{EI}{\rho A L^4}},\ \ \omega = \omega^* \sqrt{\frac{\rho A L^4}{EI}},\ \ F = \frac{F^* L^4}{EID} \tag{3.3}$$

The equation of motion now becomes the following:

$$\frac{\partial^4 w}{\partial x^4} + \frac{\partial^2 w}{\partial \tau^2} = F \sin(\omega\tau)\delta_d(x - x_f), \quad w(x_i, \tau) \leq 1 \tag{3.4}$$

with the following boundary conditions:

$$w(0,\tau) = w(1,\tau) = 0 \quad \text{and} \quad \frac{\partial^2 w(0,\tau)}{\partial x^2} = \frac{\partial^2 w(1,\tau)}{\partial x^2} = 0 \tag{3.5}$$

Two further initial conditions are required:

$$w(x,0) = w_0(x) \quad \text{and} \quad \dot{w}(x,0) = \dot{w}_0(x) \tag{3.6}$$

3.1.1 Natural frequencies and mode-shapes

In this section, we derive the expressions for natural frequencies and mode-shapes of the simply-supported beam. The obtained mode-shapes will be used in the expansion theorem to obtain

the solution of equation 3.4. To solve for the natural frequencies and mode-shapes, we consider the following homogenous PDE, which is obtained by dropping the forcing function on the right-hand side of equation 3.4:

$$\frac{\partial^4 w}{\partial x^4} + \frac{\partial^2 w}{\partial \tau^2} = 0 \tag{3.7}$$

with boundary conditions:

$$w(0,\tau) = w(1,\tau) = 0 \quad \text{and} \quad \frac{\partial^2 w(0,\tau)}{\partial x^2} = \frac{\partial^2 w(1,\tau)}{\partial x^2} = 0 \tag{3.8}$$

We assume a solution using the method of separation of variables to be of the following form:

$$w(x,\tau) = W(x)q(\tau) \tag{3.9}$$

Substituting equation 3.9 into equation 3.7, we arrive at the following:

$$\frac{\frac{d^4 W}{dx^4}}{W} = -\frac{\frac{d^2 q}{d\tau^2}}{q} \tag{3.10}$$

The left-hand side of equation 3.10 is a spatial function and the right-hand side is only a function of time. Equation 3.10 will only have a solution if both sides are equal to a constant, which should always be positive (Ω^4) so that the time-dependent differential equation will have a harmonic solution. Equation 3.10 reduces to the following two differential equations:

$$\frac{d^4 W}{dx^4} - \Omega^4 W = 0 \tag{3.11}$$

and

$$\frac{d^2 q}{d\tau^2} + \Omega^4 q = 0 \tag{3.12}$$

Equation 3.12 has a harmonic solution with a frequency of oscillation equal to Ω^2. In essence, we wish to find the mode shapes (spatial functions) that satisfy equation 3.11, and those modes will have a corresponding natural frequency given by Ω^2. Equation 3.11 has the following solution:

$$W(x) = C_1 \sin(\Omega x) + C_2 \cos(\Omega x) + C_3 \sinh(\Omega x) + C_4 \cosh(\Omega x) \tag{3.13}$$

Substituting equation 3.9 into equation 3.8, we obtain the following boundary conditions:

$$W(0) = W(1) = 0 \quad \text{and} \quad \frac{d^2 W(0)}{dx^2} = \frac{d^2 W(1)}{dx^2} = 0 \tag{3.14}$$

Evaluating equation 3.13 at the first boundary conditions, we obtain the following:

$$W(0) = C_2 + C_4 = 0 \tag{3.15}$$

and

$$\frac{d^2W(0)}{dx^2} = -C_2 + C_4 = 0 \tag{3.16}$$

The above equations give $C_2 = C_4 = 0$, and equation 3.13 can be reduced as follows:

$$W(x) = C_1 \sin(\Omega x) + C_3 \sinh(\Omega x) \tag{3.17}$$

Substituting equation 3.17 into other two boundary conditions in equation 3.14, we arrive at the following:

$$\frac{d^2W(1)}{dx^2} = \Omega^2(-C_1 \sin(\Omega) + C_3 \sinh(\Omega)) = 0 \tag{3.18}$$

and

$$W(1) = C_1 \sin(\Omega) + C_3 \sinh(\Omega) = 0 \tag{3.19}$$

Adding equation 3.18 (after dropping the Ω^2) and equation 3.19, we have:

$$C_3 \sinh(\Omega) = 0 \tag{3.20}$$

The above equation holds if $\Omega = 0$, which gives the trivial solution of zero frequency. For a nontrivial solution, we must have $C_3 = 0$. Equation 3.19 now becomes:

$$C_1 \sin(\Omega) = 0 \tag{3.21}$$

The above equation can be true if $C_1 = 0$, which means that $W(x) = 0$ (a trivial solution); therefore, $\sin(\Omega) = 0$, which gives:

$$\Omega = j\pi, \quad j = 1, 2, ..., \infty \tag{3.22}$$

The natural frequencies given by Ω^2 are:

$$\omega_j = (j\pi)^2, \quad j = 1, 2, ..., \infty \tag{3.23}$$

The mode shape corresponding to the natural frequency ω_j can be obtained by substituting equation 3.22 into equation 3.17:

$$W_j(x) = C_1 \sin(j\pi x) \tag{3.24}$$

It should be noted that the above mode shape has arbitrary amplitude.

3.1.2 Assumed solution

Using the expansion theorem, a solution to equation 3.4 is assumed to be of the following form:

$$w(x,\tau) = \sum_{j=1}^{\infty} W_j(x) q_j(\tau) \tag{3.25}$$

where $W_j(x)$ and $q_j(\tau)$ correspond to the j^{th} mode shape and the corresponding modal coordinate for the beam, respectively. Substituting the above form of solution into equation 3.4, we get:

$$\sum_{j=1}^{\infty} \frac{d^4 W_j(x)}{dx^4} q_j(\tau) + \sum_{j=1}^{\infty} W_j(x) \ddot{q}_j(\tau) = F \sin(\omega\tau)\delta(x - x_f) \tag{3.26}$$

The above equation is multiplied by $W_k(x)$ and then integrated over the spatial domain, which yields the following expression:

$$\sum_{j=1}^{\infty} q_j(\tau) \int_0^1 \frac{d^4 W_j(x)}{dx^4} W_k(x) dx + \sum_{j=1}^{\infty} \ddot{q}_j(\tau) \int_0^1 W_j(x) W_k(x) dx =$$

$$F \sin(\omega\tau) \int_0^1 \delta_d(x - x_f) W_k(x) dx, \qquad k = 1, 2, ..., \infty \tag{3.27}$$

We now evaluate the following integral:

$$\int_0^1 W_j(x) W_k(x) dx = C_1^2 \int_0^1 \sin(j\pi x) \sin(k\pi x) dx = \frac{C_1^2}{2} \delta_{jk} \tag{3.28}$$

where δ_{jk} is Kronecker's delta, defined as:

$$\delta_{jk} = \begin{cases} 1, & \text{if } j = k \\ 0, & \text{if } j \neq k \end{cases} \tag{3.29}$$

Since the amplitudes of the mode shapes are arbitrary, we choose the amplitude of mode shapes (C_1) to be $\sqrt{2}$. This procedure of choosing the amplitudes of mode shapes such that the right-hand side of equation 3.28 becomes δ_{jk} is called mass-normalization. By using the mass-normalized mode shapes, it can be shown that:

$$\int_0^1 \frac{d^4 W_j(x)}{dx^4} W_k(x) dx = \omega_j^2 \delta_{jk} = (j\pi)^4 \delta_{jk} \tag{3.30}$$

The coupled ordinary differential equations (ODEs) given by equation 3.27 can be decoupled using the orthogonality relations (equation 3.28 and equation 3.30). The uncoupled ODEs, after truncating the system to N modes, are as follows:

$$\ddot{q}_j(\tau) + \omega_j^2 q_j = W_j(x_f) F \sin(\omega\tau), \;\; j = 1, 2, ..., N \tag{3.31}$$

To obtain the modal initial conditions, we substitute the series solution given by equation 3.25 into equation 3.6, which gives the following relations for displacement and velocity initial conditions:

$$w(x, 0) = \sum_{j=0}^{\infty} W_j(x) q_j(0) \tag{3.32}$$

and

$$\dot{w}(x, 0) = \sum_{j=0}^{\infty} W_j(x) \dot{q}_j(0) \tag{3.33}$$

Multiplying both sides of equations 3.32 and 3.33 by $W_k(x)$, and then integrating over the domain, results in the following modal initial conditions:

$$q_j(0) = \int_0^1 w(x, 0) W_j(x) dx \;\text{ and }\; \dot{q}_j(0) = \int_0^1 \dot{w}(x, 0) W_j(x) dx \tag{3.34}$$

3.1.3 Impact modelling

Once the system parameters have been specified, equation 3.31 can be numerically integrated until the impact occours. At the impact event, we have information about the pre-impact displacement and velocity distribution of the beam, which are respectively $w(x, \tau_-)$ and $\dot{w}(x, \tau_-)$, where τ_- is the time immediately prior to impact. The objective is to relate the pre-impact displacement and velocity distributions to the post-impact distributions. In rigid-body problems involving translation, if the velocity of one point is known, then the velocities of all other points on the rigid body can be easily derived. With continuous systems, however, we must predict the post-impact velocity distribution, $\dot{w}(x, \tau_+)$, given only a post-impact velocity at the impact location, $\dot{w}(x_i, \tau_+)$. At the instant of impact, it is assumed that the configuration of the system does not change, as was assumed in [75]:

$$w(x, \tau_+) = w(x, \tau_-) \tag{3.35}$$

The corresponding modal post-impact displacement initial conditions are:

$$q_j(\tau_+) = q_j(\tau_-) \tag{3.36}$$

The velocity of the beam at the impact location changes according to the following classical coefficient of restitution rule:

$$\dot{w}(x_i, \tau_+) = -R\dot{w}(x_i, \tau_-) \tag{3.37}$$

where R is the coefficient of restitution. In addition to equation 3.37, the pre-impact velocity distribution, $\dot{w}(x, \tau_-)$, is also known. We must now obtain the post-impact velocity distribution, $\dot{w}(x, \tau_+)$, satisfying equation 3.37. The method proposed by Wagg and Bishop [75] for obtaining the post-impact velocity distribution and the corresponding modal velocity initial conditions is presented here. First, equation 3.37 is written as follows:

$$\sum_{j=1}^{N} W_j(x_i)\dot{q}_j(\tau_+) = -R\sum_{j=1}^{N} W_j(x_i)\dot{q}_j(\tau_-) \tag{3.38}$$

In order to solve for the post-impact modal velocity initial conditions, we require $N-1$ additional equations, which can be obtained from the assumption that the velocity of the beam remains the same before and after impact at all points except for the impact location. Selecting $N-1$ collocation points $(x_{c1},\ x_{c2}, ..., x_{c(N-1)})$, we have the following relationships:

$$\dot{w}(x_{ck}, \tau_+) = \dot{w}(x_{ck}, \tau_-),\ \ k = 1, 2, ..., N-1 \tag{3.39}$$

which can be further expressed as follows:

$$\sum_{j=1}^{N} W_j(x_{ck})\dot{q}_j(\tau_+) = \sum_{j=1}^{N} W_j(x_{ck})\dot{q}_j(\tau_-),\ \ k = 1, 2, ..., N-1 \tag{3.40}$$

The chosen collocation points must be distinct from the nodal points of the modes that are included in the simulation. Equations 3.38 and 3.40 can now be expressed in matrix form. As an example, we show the matrix form for a three-mode problem. Figure 3.2 illustrates the collocation method for obtaining the post-impact velocity distribution. In this case, we must choose two collocation points, x_{c1} and x_{c2}, as well as the impact location, x_i. The matrix

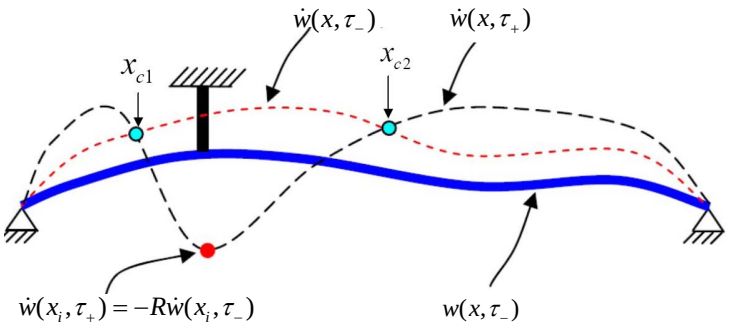

Figure 3.2: Illustration of collocation method.

equation relating the pre- and post-impact modal velocities can be written as follows:

$$\begin{Bmatrix} \dot{q}_1(\tau_+) \\ \dot{q}_2(\tau_+) \\ \dot{q}_3(\tau_+) \end{Bmatrix} = [\mathbf{W}]^{-1} \begin{bmatrix} 1 & 0 & 0 \\ 0 & -R & 0 \\ 0 & 0 & 1 \end{bmatrix} [\mathbf{W}] \begin{Bmatrix} \dot{q}_1(\tau_-) \\ \dot{q}_2(\tau_-) \\ \dot{q}_3(\tau_-) \end{Bmatrix}$$

$$\text{where} \quad [\mathbf{W}] = \begin{bmatrix} W_1(x_{c1}) & W_2(x_{c1}) & W_3(x_{c1}) \\ W_1(x_i) & W_2(x_i) & W_3(x_i) \\ W_1(x_{c2}) & W_2(x_{c2}) & W_3(x_{c2}) \end{bmatrix} \tag{3.41}$$

It is clear from equation 3.41 that the post-impact modal velocities are strongly dependent on the selected collocation points, and can lead to completely different vibro-impacting system dynamics. Certain choices of collocation points may also lead to the artificial input of energy into the mechanical oscillator – that is, where the predicted post-impact velocity distribution contains more energy than the pre-impact velocity distribution. In order to resolve this issue, a new method is proposed in the next section.

3.1.4 The impulse-based CoR method

Before discussing the proposed impulse-based CoR method, we revisit the idea of the unit impulse response of a continuous system. We derive the expression for velocity distribution of a beam, initially at rest, subject to a unit impulse. The equation of motion of a beam with a unit impulse as the forcing function, acting at the impact location x_i at time $\tau = \tau_-$, can be written as follows:

$$\frac{\partial^4 w}{\partial x^4} + \frac{\partial^2 w}{\partial \tau^2} = \delta_d(x - x_i)\delta_d(\tau - \tau_-) \tag{3.42}$$

After substituting the solution given by equation 3.25 into equation 3.42, we get:

$$\sum_{j=1}^{\infty} \frac{d^4 W_j(x)}{dx^4} q_j(\tau) + \sum_{j=1}^{\infty} W_j(x) \ddot{q}_j(\tau) = \delta_d(\tau - \tau_-)\delta_d(x - x_i) \tag{3.43}$$

We multiply the above equation with $W_k(x)$ and then integrate over the spatial domain, which yields the following expression:

$$\sum_{j=1}^{\infty} q_j(\tau) \int_0^1 \frac{d^4 W_j(x)}{dx^4} W_k(x) dx + \sum_{j=1}^{\infty} \ddot{q}_j(\tau) \int_0^1 W_j(x) W_k(x) dx =$$

$$\delta_d(\tau - \tau_-) \int_0^1 \delta_d(x - x_i) W_k(x) dx, \quad k = 1, 2, ..., \infty \tag{3.44}$$

We choose the mass normalized mode-shapes $W_j(x) = \sqrt{2}\sin(j\pi x)$ of the pinned-pinned beam as the spatial functions in equation 3.25. The coupled ODEs given by equation 3.44 can be decoupled using the orthogonality relations given by equations 3.28 and 3.30. The resulting system of modal equations as follows:

$$\ddot{q}_j(\tau) + \omega_j^2 q_j(\tau) = W_j(x_i)\delta_d(\tau - \tau_-), \quad j = 1, 2, ..., \infty \tag{3.45}$$

The above equation represents the dynamics of the j^{th} modal coordinate, and can be solved using the Laplace transform technique. It should be noted that the beam is assumed to be at rest before the application of the unit impulse, so the modal initial conditions are zero before the application of impact. Taking the Laplace transform of both sides of equation 3.45, we get:

$$\mathcal{L}\{q_j(\tau)\} = \frac{W_j(x_i)e^{-s\tau_-}}{s^2 + \omega_j^2}, \quad j = 1, 2..., \infty \tag{3.46}$$

Now taking the inverse Laplace transform of equation 3.46 by using the second shifting theorem, we get:

$$q_j(\tau) = W_j(x_i)\frac{1}{\omega_j}\sin(\omega_j(\tau - \tau_-)), \quad j = 1, 2, .., \infty, \qquad \tau > \tau_- \tag{3.47}$$

Substituting equation 3.47 into 3.25 and truncating the series solution to N terms results in the following displacement response to equation 3.42:

$$w(x, \tau) = \sum_{j=1}^{N} W_j(x)\frac{W_j(x_i)}{\omega_j}\sin\left(\omega_j(\tau - \tau_-)\right), \qquad \tau > \tau_- \tag{3.48}$$

as well as the following velocity response:

$$\dot{w}(x,\tau) = \sum_{j=1}^{N} W_j(x) W_j(x_i) \cos\left(\omega_j(\tau - \tau_-)\right), \qquad \tau > \tau_- \tag{3.49}$$

It can be seen that the displacement of the beam is $w(x,\tau_+) = 0$ at $\tau = \tau_+$, but the velocity of the beam after the application of impact is nonzero i.e., the unit impulse results in a sudden change in the velocity of the beam. Immediately after the application of impact (i.e., when $\tau = \tau_+$), the system has the following velocity distribution:

$$\dot{w}(x,\tau_+) = \dot{U}(x,\tau_+) = \sum_{j=1}^{N} W_j(x) W_j(x_i) \tag{3.50}$$

where $\dot{U}(x,\tau_+)$ is the velocity distribution of the continuous structure due to a unit impulse at location x_i. The magnitude of the velocity at the impact location, x_i, can now be written as follows:

$$\dot{U}(x_i,\tau_+) = \sum_{j=1}^{N} W_j(x_i)^2 \tag{3.51}$$

We now discuss the impulse-based CoR method. As shown in Figure 3.3, we attempt to find the

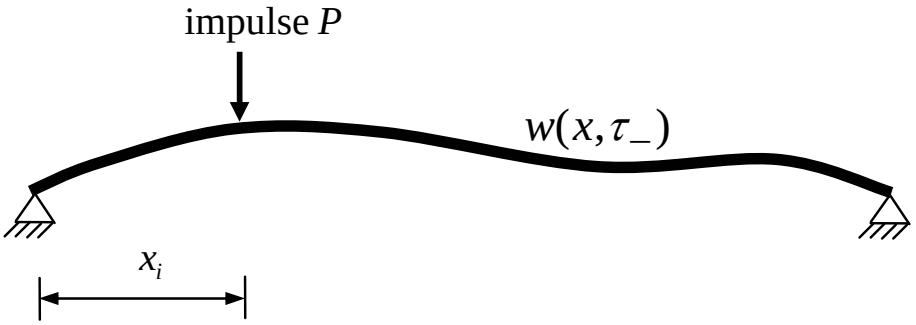

Figure 3.3: Impact modelled using finite impulse.

non-dimensional impulse P that must be applied to the continuous system at the time of impact so that the post-impact velocity at the impact location is as described by equation 3.37. We make use of the velocity distribution of the beam due to a unit impulse at the impact location. The calculated impulse P should generate similar initial conditions as the unit impulse, but of different magnitude with a scaling factor of P. The velocity at the impact location due to an impulse P, when added to the pre-impact velocity at the impact location, should result in the

following post-impact velocity at the impact location:

$$\dot{w}(x_i, \tau_-) + P\dot{U}(x_i, \tau_+) = \dot{w}(x_i, \tau_+) \tag{3.52}$$

In equation 3.52, the post-impact velocity, $\dot{w}(x_i, \tau_+)$, can be expressed in terms of the pre-impact velocity using equation 3.37. Thus, equation 3.52 now becomes:

$$\dot{w}(x_i, \tau_-) + P\dot{U}(x_i, \tau_+) = -R\dot{w}(x_i, \tau_-) \tag{3.53}$$

Rearranging equation 3.53, the magnitude of the impulse can be obtained as follows:

$$P = -(R+1)\frac{\dot{w}(x_i, \tau_-)}{\dot{U}(x_i, \tau_+)} \tag{3.54}$$

The post-impact velocity distribution, $\dot{w}(x, \tau_+)$, can be obtained by superimposing the velocity distribution due to impulse P at time τ_- on the pre-impact velocity distribution, $\dot{w}(x, \tau_-)$:

$$\dot{w}(x, \tau_+) = \dot{w}(x, \tau_-) - (R+1)\frac{\dot{w}(x_i, \tau_-)}{\dot{U}(x_i, \tau_+)}\dot{U}(x, \tau_+) \tag{3.55}$$

Multiplying both sides of equation 3.55 with modal functions and integrating over the domain results in the following relation:

$$\dot{q}_j(\tau_+) = \dot{q}_j(\tau_-) - (R+1)\frac{\dot{w}(x_i, \tau_-)}{\dot{U}(x_i, \tau_+)}W_j(x_i), \quad j = 1, 2, ..., N \tag{3.56}$$

Equation 3.56 relates the pre-impact and post-impact modal initial conditions, without the need to choose collocation points.

3.1.5 Alternative derivation for impulse-based CoR method

Let $w(x, \tau_-)$ and $\dot{w}(x, \tau_-)$ be the displacement and velocity distributions of the beam just before the application of impact. Let us assume that at the instant of impact (τ_-) an impulse of magnitude P acts on the beam at the impact location. The equation of motion of the beam can be written as:

$$\frac{\partial^4 w}{\partial x^4} + \frac{\partial^2 w}{\partial \tau^2} = P\delta_d(x - x_i)\delta_d(\tau - \tau_-) \tag{3.57}$$

We assume the same pinned-pinned boundary conditions for the above PDE. Now substituting the series solution given by equation 3.25 into the above PDE, we have:

$$\sum_{j=1}^{N} \frac{d^4 W_j(x)}{dx^4} q_j(\tau) + \sum_{j=1}^{N} W_j(x)\ddot{q}_j(\tau) = P\delta_d(x - x_i)\delta_d(\tau - \tau_-) \tag{3.58}$$

Integrating the above equation between τ_- and τ_+, we get:

$$\sum_{j=1}^{N} \frac{d^4 W_j(x)}{dx^4} \int_{\tau_-}^{\tau_+} q_j(\tau) d\tau + \sum_{j=1}^{N} W_j(x) \int_{\tau_-}^{\tau_+} \ddot{q_j}(\tau) d\tau = P\delta_d(x - x_i) \int_{\tau_-}^{\tau_+} \delta_d(\tau - \tau_-) d\tau \tag{3.59}$$

The post-impact displacement distribution will remain the same as the pre-impact distribution, as the impact is assumed to occur in an infinitesimal amount of time, i.e., $w(x, \tau_+) = w(x, \tau_-)$. Hence we have $q_j(\tau_+) = q_j(\tau_-)$ and thus the first integral in equation 3.59 becomes zero. Integrating the second term with respect to time, and from the definition of Dirac's delta function ($\int_{\tau_-}^{\tau_+} \delta_d(\tau - \tau_-) d\tau = 1$), equation 3.59 becomes:

$$\sum_{j=1}^{N} W_j(x) \left(\dot{q_j}(\tau_+) - \dot{q_j}(\tau_-) \right) dt = P\delta_d(x - x_i) \tag{3.60}$$

Now substituting for $\dot{w}(x, \tau) = \sum_{j=1}^{N} W_j(x) \dot{q_j}(\tau)$, we get:

$$\dot{w}(x, \tau_+) = \dot{w}(x, \tau_-) + P\delta_d(x - x_i) \tag{3.61}$$

From the above equation we can say that the effect of applying an impulse on the Euler-Bernoulli beam, results in a sudden change in velocity of the beam, immediately after the application of impact. The resulting velocity distribution after impact is nothing but a Dirac's function in space added to the pre-impact velocity distribution. The scaling parameter P (magnitude of impulse) in equation 3.61 is to be found such that the post-impact velocity at the impact location is as described by equation 3.37. Multiplying both sides of equation 3.61 by $W_k(x)$ and integrating over the domain results in:

$$\sum_{j=1}^{N} \dot{q_j}(\tau_+) \int_0^1 W_j(x) W_k(x) dx = \sum_{j=1}^{N} \dot{q_j}(\tau_-) \int_0^1 W_j(x) W_k(x) dx + P \int_0^1 W_k(x) \delta_d(x - x_i) dx \tag{3.62}$$

Making use of equation 3.28, the above equation reduces to:

$$\dot{q_j}(\tau_+) = \dot{q_j}(\tau_-) + P W_j(x_i) \tag{3.63}$$

we now substitute equation 3.63 into equation 3.37:

$$\sum_{j=1}^{N} W_j(x_i) \left[\dot{q_j}(\tau_-) + P W_j(x_i) \right] = -R \sum_{j=1}^{N} W_j(x_i) \dot{q_j}(\tau_-) \tag{3.64}$$

which can be simplified to obtain the following expression for P:

$$P = -\frac{(1+R)\sum_{j=1}^{N} W_j(x_i) q_j(\tau_-)}{\sum_{j=1}^{N} W_j(x_i)^2} = -\frac{(1+R)\dot{w}(x_i,\tau_-)}{\dot{U}(x_i,\tau_+)} \tag{3.65}$$

The post-impact modal velocities can be obtained by substituting equation 3.65 into equation 3.63, which results in the following expression:

$$\dot{q}_j(\tau_+) = \dot{q}_j(\tau_-) - \frac{(1+R)\dot{w}(x_i,\tau_-)}{\dot{U}(x_i,\tau_+)} W_j(x_i), \quad j = 1, 2, ..., N \tag{3.66}$$

The above expression is the same as that of equation 3.56.

3.1.6 Relating the pre-impact and post-impact energies

In this section, we derive the relationship between pre-impact and post-impact energies and show that the energy of the beam after impact is bounded by its energy before impact. The expression for the dimensionless energy [53] ($\triangle$) of the beam is:

$$\triangle(\tau) = \frac{1}{2}\int_0^1 \left(\frac{\partial^2 w}{\partial x^2}\right)^2 dx + \frac{1}{2}\int_0^1 \left(\frac{\partial w}{\partial \tau}\right)^2 dx \tag{3.67}$$

Substituting the series solution (equation 3.25) by retaining N terms in the above expression gives:

$$\triangle(\tau) = \frac{1}{2}\int_0^1 \left(\sum_{j=1}^{N} \frac{dW_j^2(x)}{dx^2} q_j(\tau)\right)\left(\sum_{j=1}^{N} \frac{dW_j^2(x)}{dx^2} q_j(\tau)\right) dx \tag{3.68}$$

$$+\frac{1}{2}\int_0^1 \left(\sum_{j=1}^{N} W_j(x)\dot{q}_j(\tau)\right)\left(\sum_{j=1}^{N} W_j(x)\dot{q}_j(\tau)\right) dx \tag{3.69}$$

Substituting $W_j(x) = \sqrt{2}\sin(j\pi x)$ and using the following relations:

$$\int_0^1 \frac{d^2 W_j(x)}{dx^2}\frac{d^2 W_k(x)}{dx^2} dx = (j\pi)^4 \delta_{jk} = \omega_j^2 \delta_{jk} \tag{3.70}$$

we obtain the following expression for the energy of the beam:

$$\triangle(\tau) = \frac{1}{2}\sum_{j=1}^{N} \dot{q}_j(\tau)^2 + \frac{1}{2}\sum_{j=1}^{N} q_j(\tau)^2 \omega_j^2 \tag{3.71}$$

The energy in the beam just before the impact at $\tau = \tau_-$ is given by:

$$\triangle(\tau_-) = \frac{1}{2}\sum_{j=1}^{N} \dot{q_j}(\tau_-)^2 + \frac{1}{2}\sum_{j=1}^{N} q_j(\tau_-)^2\omega_j^2 \tag{3.72}$$

and the post-impact energy at $\tau = \tau_+$ is given by:

$$\triangle(\tau_+) = \frac{1}{2}\sum_{j=1}^{N} \dot{q_j}(\tau_+)^2 + \frac{1}{2}\sum_{j=1}^{N} q_j(\tau_+)^2\omega_j^2 \tag{3.73}$$

Substituting equation 3.40 into equation 3.73 and making use of the relation $q_j(\tau_+) = q_j(\tau_-)$, we get:

$$\triangle(\tau_+) = \frac{1}{2}\sum_{j=1}^{N} \left(\dot{q_j}(\tau_-) - (R+1)\frac{\dot{w}(x_i,\tau_-)}{\dot{U}(x_i,\tau_-)}W_j(x_i)\right)^2 + \frac{1}{2}\sum_{j=1}^{N} q_j(\tau_-)^2\omega_j^2 \tag{3.74}$$

Further simplifying the above expression gives:

$$\triangle(\tau_+) = \triangle(\tau_-) + \frac{1}{2}(R+1)^2\frac{\dot{w}(x_i,\tau_-)^2}{\dot{U}(x_i,\tau_-)^2}\sum_{j=1}^{N} W_j(x_i)^2 - (R+1)\frac{\dot{w}(x_i,\tau_-)}{\dot{U}(x_i,\tau_-)}\sum_{j=1}^{N} W_j(x_i)\dot{q_j}(\tau_-) \tag{3.75}$$

Substituting $\dot{U}(x_i,\tau_-) = \sum_{j=1}^{N} W_j^2(x_i)$ and $\sum_{j=1}^{N} W_j(x_i)\dot{q_j}(\tau_-) = \dot{w}(x_i,\tau_-)$, we get:

$$\triangle(\tau_+) = \triangle(\tau_-) + \frac{1}{2}(R+1)^2\frac{\dot{w}(x_i,\tau_-)^2}{\dot{U}(x_i,\tau_+)} - (R+1)\frac{\dot{w}(x_i,\tau_-)^2}{\dot{U}(x_i,\tau_+)} \tag{3.76}$$

Simplifying equation 3.76 results in the following equation relating the post-impact and pre-impact energies:

$$\triangle(\tau_+) = \triangle(\tau_-) + \frac{1}{2}\left(R^2-1\right)\frac{\dot{w}(x_i,\tau_-)^2}{\dot{U}(x_i,\tau_+)} \tag{3.77}$$

Substituting $R = 1$ in equation 3.77, we get $\triangle(\tau_+) = \triangle(\tau_-)$, i.e., the energy remains constant before and after impact. For all $R < 1$, the expression $\frac{1}{2}\left(R^2-1\right)\frac{\dot{w}(x_i,\tau_-)^2}{\dot{U}(x_i,\tau_+)} < 0$, which means that, for any coefficient of restitution chosen between 0 and 1, the beam loses energy at the impact. The amount of energy lost is equal to $\frac{1}{2}\left(1-R^2\right)\frac{\dot{w}(x_i,\tau_-)^2}{\dot{U}(x_i,\tau_+)}$.

3.2 Results and discussion

CoR-based modelling is a limiting case of the local compliance approach, in which the stiffness of the obstacle reaches infinity. We, therefore, compare numerical simulations obtained using the proposed impulse-based CoR method with those obtained using a penalty approach [68],

where the obstacle is modelled as a linear spring with very high stiffness. We now briefly describe the penalty approach. The equation of motion of the beam in dimensionless form when modelled with the penalty approach is of the following form:

$$\frac{\partial^4 w}{\partial x^4} + \frac{\partial^2 w}{\partial \tau^2} = -F_{contact} + F\sin(\omega\tau)\delta_d(x - x_f) \tag{3.78}$$

where the contact force $F_{contact}$ is represented as:

$$F_{contact} = \begin{cases} K\left[w(x_i,\tau) - 1\right] & w(x_i,\tau) \geq 1 \\ 0 & w(x_i,\tau) < 1 \end{cases} \tag{3.79}$$

The boundary conditions and initial conditions are given by equations 3.5 and equation 3.6. When the beam penetrates into the obstacle, a contact force is generated as described by equation 3.79. If the penalty parameter (contact stiffness K) is chosen sufficiently high, the penetration of the beam will be very small, approaching zero as K tends to infinity. The generated contact forces will push the beam away from the obstacle, thus simulating its impact behaviour. Equation 3.78 along with the contact force expression (equation 3.79) can be solved numerically using modal analysis technique presented in section 3.1.2.

Initially, we present the numerical solution for a free vibration problem and emphasize the energy-conserving nature of the formulation. The initial conditions for this particular study are as follows:

$$w(x,0) = -1.01\sin(\pi x) \text{ and } \dot{w}(x,0) = 0 \tag{3.80}$$

The physical parameters used in numerical simulation are listed in Table 3.1. We compare

Table 3.1: Parameters used in simulation of free vibration.

Physical parameter	**Quantity**
Penalty stiffness (K)	1×10^{12}
Impact location (x_i)	0.5
Coefficient of restitution (R)	1

the four-mode solutions obtained when different sets of collocation points are chosen, as shown

Table 3.2: Collocation method parameters used in simulation.

Number of modes	**Collocation points**
4	CP1=[0.2, 0.3, 0.7]
4	CP2=[0.15, 0.4, 0.8]
4	CP3=[0.1, 0.35, 0.9]

in Table 3.2. The modal equations given by equation 3.31 are solved in MATLAB using the numerical integrator ode45 and the built-in event detection algorithm for detecting impacts. Relative and absolute tolerances were chosen to be 10^{-9} to obtain a high degree of accuracy. The ode45 is a fourth order Runga-Kutta integrator [62]. The event detection algorithm in Matlab is based on the bisection method and detects a zero crossing in the function (in our case it is the gap function $(w(x_i, t) - 1 = 0)$) on which the event is to be detected. Figure 3.4(a) shows the displacement of the beam at the impact location for different sets of collocation points. Figure 3.4(b) shows a magnified version of the displacement at the first impact, and clearly illustrates the dependence of the response on the selected collocation points. This dependence is also confirmed in Figures 3.5 and 3.6,which show the velocity and phase plot at the impact location.

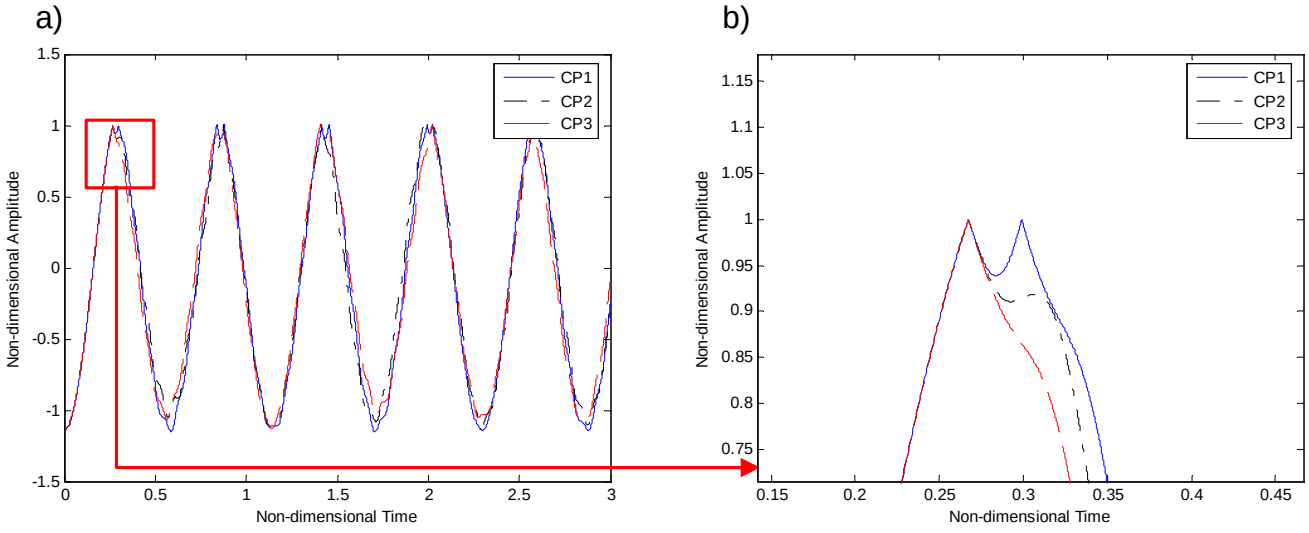

Figure 3.4: Response at impact location: (a) displacement, (b) magnified view at first impact.

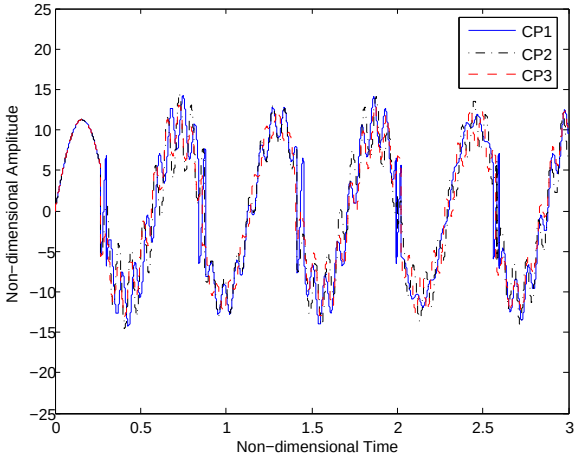

Figure 3.5: Velocity at impact location.

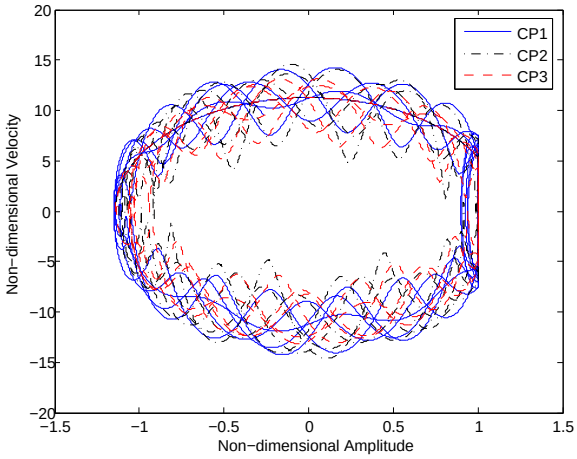

Figure 3.6: Phase plot at impact location.

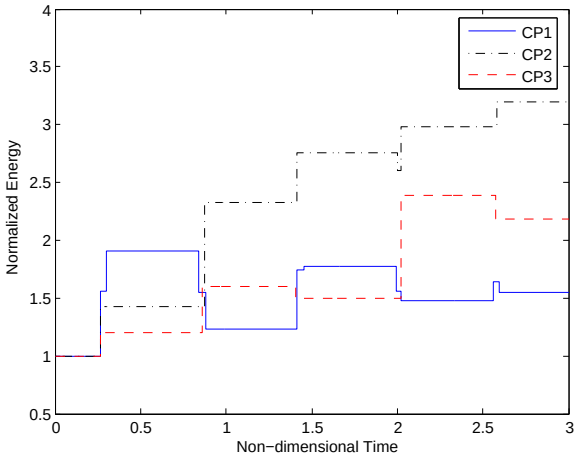

Figure 3.7: Energy of the mechanical system.

Figure 3.7 clearly shows that the energy of the mechanical system is increasing. It should be noted that, since the current problem is a free vibration problem with CoR equal to 1, the energy in the system should be conserved. The lack of energy conservation can be explained by Figure 3.8, which shows the pre- and post-impact velocity distributions at the first impact for

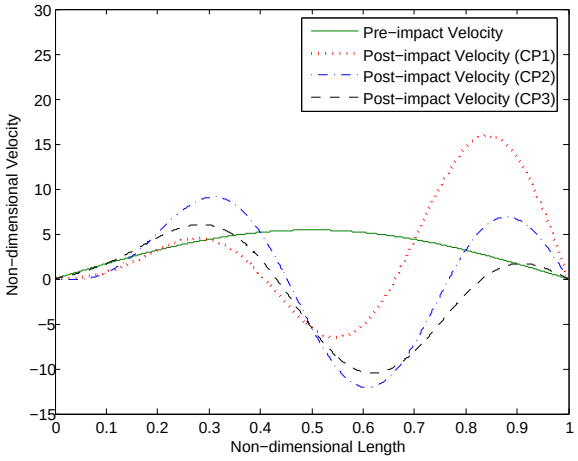

Figure 3.8: Pre- and post-impact velocity distributions.

different sets of collocation points. It can be seen that the post-impact velocity distributions are different for different selections of collocation points. Since it is assumed that the displacement configuration remains the same before and after impact, the strain energy cannot be altered and any incorrect predictions of post-impact initial conditions can lead to spurious energy input. Equation 3.40 strongly enforces that the pre- and post-impact velocities to match at the collocation points, and relates velocities at the impact location as given by equation 3.37, but we have no control over the velocity at other points.

Now, we examine the results obtained for a four-mode problem using the impulse-based CoR method proposed above. Figures 3.9(a) and 3.9(b) show the displacements at the impact location obtained for free and forced vibration problems using the impulse-based CoR and penalty methods. The physical parameters for forcing function amplitude, location, and frequency are shown in Table 3.3. The forcing function frequency is chosen to be the first natural frequency of the beam. It can be clearly seen from Figure Ch1Figure9 that the displacement response agree exactly. This fact is further illustrated in Figures 3.10 and 3.11, which show the velocity and phase portrait at the impact location.

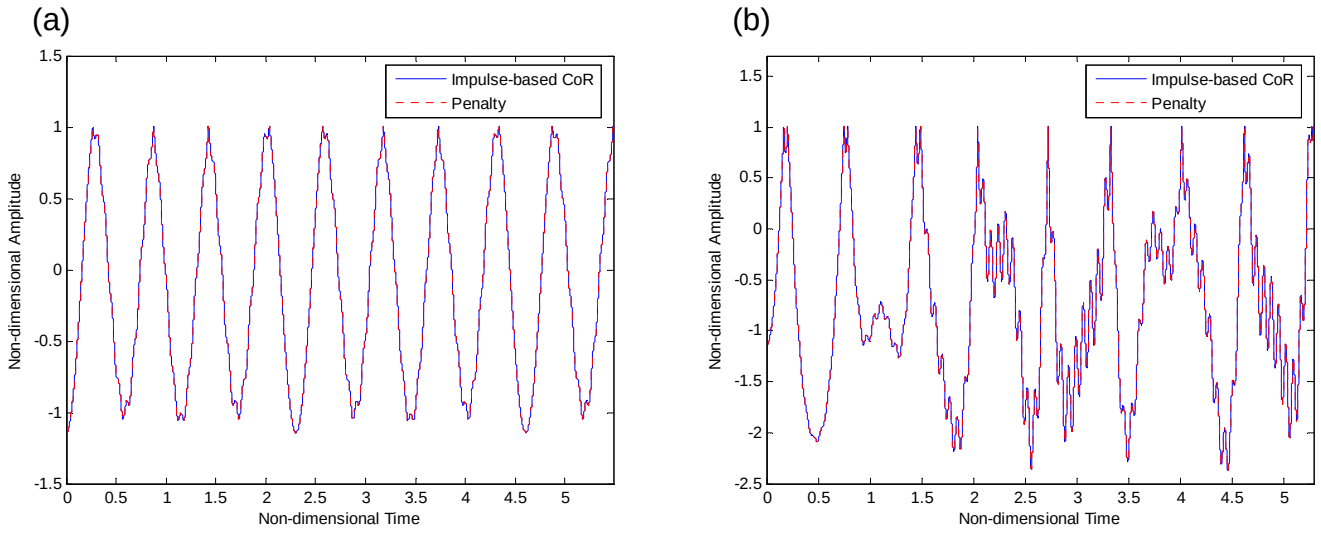

Figure 3.9: Displacement at the impact location: (a) free vibration, (b) forced vibration.

Table 3.3: Forcing function parameters used in simulations.

Physical parameter	**Quantity**
Amplitude of forcing function (F)	72.0000
Location of forcing function (x_f)	0.5
Frequency of forcing function ($\omega = \omega_1$)	π^2

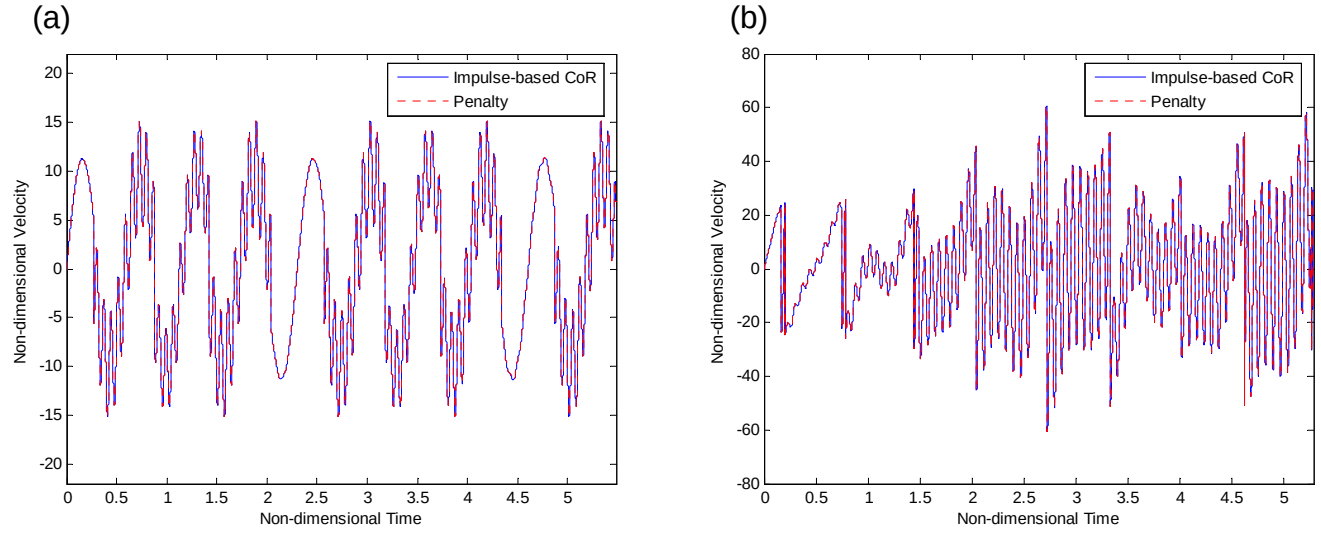

Figure 3.10: Velocity at the impact location: (a) free vibration, (b) forced vibration.

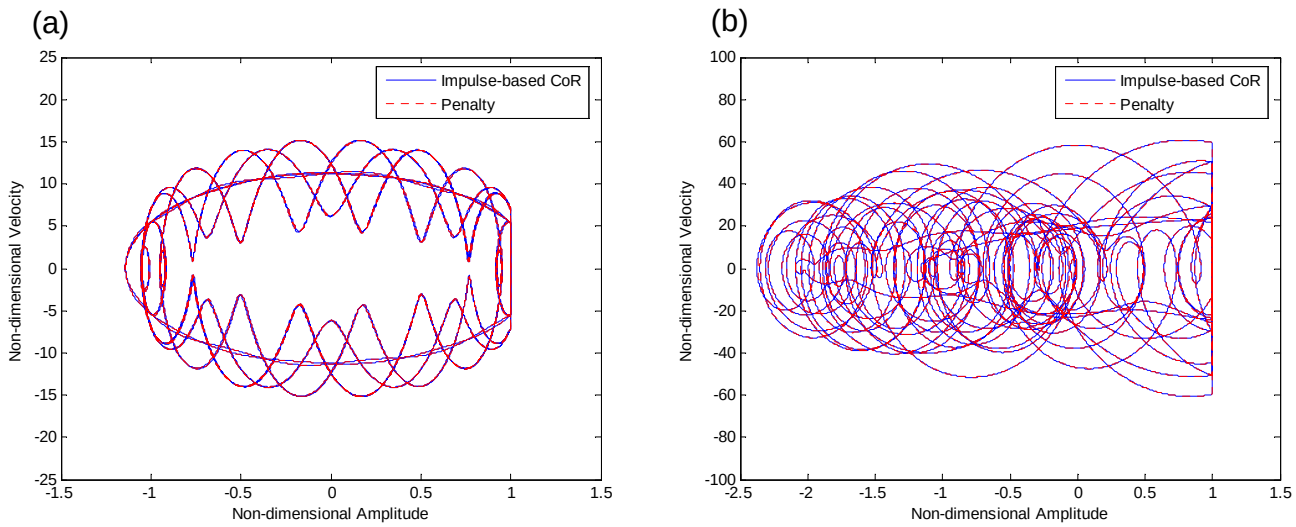

Figure 3.11: Phase plot at the impact location: (a) free vibration, (b) forced vibration.

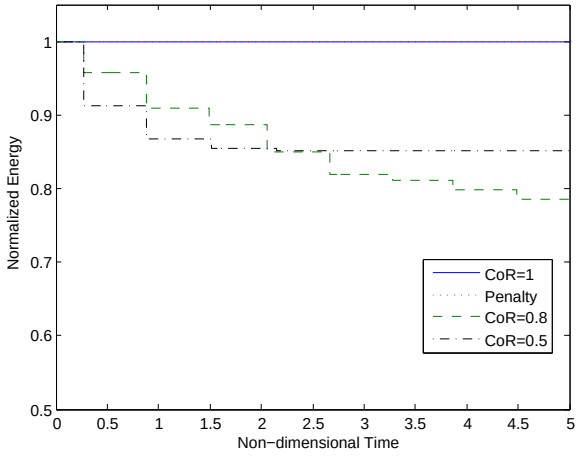

Figure 3.12: Energy in the mechanical system in free vibration.

Figure 3.12 shows the energy in the mechanical system for the free vibration problem, illustrating that the impulse-based CoR approach with R=1 and the penalty approach formulation both preserve the energy of the mechanical system. If the coefficient of restitution is decreased, the beam loses energy at every impact. Interestingly, with R=0.5 the beam settles at an energy level that is higher than that found when R=0.8. The total energy lost is a function of the number of impacts, the pre-impact velocity, and the CoR. More energy is lost at each impact when R=0.5, while more impacts occur in the duration of the simulation when R=0.8.

A comparison of normalized CPU times for the forced response problem is shown in Figure 3.13. It is evident from the graph that the difference in the CPU time grows as the number of

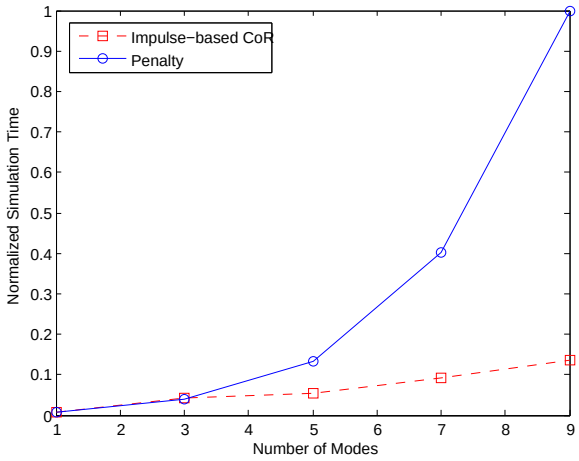

Figure 3.13: Comparison of computational efficiency.

modes considered in the problem is increased. The impulse-based CoR method runs 87% faster than the penalty approach when 9 modes are considered in the analysis. The proposed method can be used to successfully simulate the impact behaviour at a much lower computational cost compared to the penalty approach, which is particularly useful given that a large number of numerical parametric studies must be performed in order to characterize the behaviour of vibro-impacting systems. The developed method can also be incorporated into finite element codes provided that the analysis is carried out in the modal domain and a prior knowledge of the response of the structure due to a unit impulse at the impact location is known.

3.3 Experimental validation

Experimental investigations on continuous systems subjected to vibro-impacting motions are scarce in the literature. The following paragraph provides a brief overview of the work that has been done by previous researchers.

In the experimental work done by Moon and Shaw [55] and Shaw [63], a base-excited cantilever beam impacting against a one-sided elastic stop was studied. Bishop et al. [11] have experimentally studied period-1 motions in a driven beam with a one-sided stop. Experiments on a cantilever beam with a tip mass excited by a harmonically oscillating impactor were studied by Fang and Wickert [25], while Balachandran [6] studied the dynamics of the cantilever beam for both harmonic and aharmonic impactor motion. In the above mentioned literature, single-

degree-of-freedom models combined with the coefficient of restitution approach [6, 11, 25, 63] or the method of mode switching [55] were used to simulate the impact. The single-mode numerical results were qualitatively compared to the experimental results, and were found to be in good agreement. Cusumano et al. [20] conducted experiments on a cantilever beam impacted by a harmonic impactor to estimate the dimensionality of the model. Experimental and numerical studies that dealt with the multi-modal behaviour of beams combined with coefficient of restitution were done by Wagg et al. [76]. The experimental setup involved a cantilever beam, forced by an electromagnetic exciter, impacting a rigid obstacle. The authors performed extensive statistical analysis [76] to determine the excitation frequency range in which the CoR theory is applicable. Fegelman and Grosh [26] developed a numerical model based on the mode-switching method to simulate a vibro-impacting pinned-free beam. de Vorst et al. [21] studied the dynamics of a complex beam structure subjected to unilateral contact. The impact is modelled in their study using Hertzian contact law. A base-excited cantilever beam subjected to impact was also studied in [22], where the impact was again modelled using Herzian contact theory. Ervina and Wickert [23] experimentally studied the impact dynamics of a base-excited rigid body attached to a flexible beam system. The impact in the numerical simulation was modelled as a linear spring and a mode-switching approach was used. In all the above mentioned literature, even though the authors have used different approaches for simulating impact [21–23, 26, 75], an excellent agreement between numerical and experimental results were shown. In this section, we make an attempt to validate the theory developed in this chapter with the experimental results of de Vorst et al. [22].

Figure 3.14 shows the mechanical system that has been studied experimentally by de Vorst et al. [22]. The mechanical system consists of a fixed-free cantilever beam that is base-excited. The beam impacts the rigid base through a spherical contact at a predefined location along its length. An impact occurs when the relative distance between the beam and the base approaches zero. The base is excited harmonically by the displacement excitation $u(t) = 0.501 \sin(2\pi f_e t)$ mm. The beam is comprised of steel with a Young's modulus (E_{Beam}) of 2.1×10^{11} N/m^2 and a density (ρ_{Beam}) of 7800 Kg/m^3; other physical dimensions are shown in Figure 3.14.

The first three experimentally-observed natural frequencies of the beam system when not in contact with the base are 17.2 Hz, 128.9 Hz, and 378.9 Hz. The numerical code that was used in

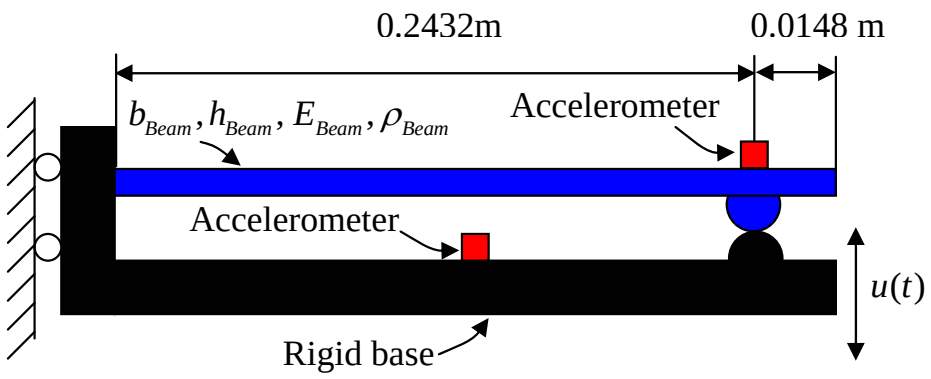

Figure 3.14: Experimental setup of the beam system [22]: $b_{Beam} = 0.0298$m, $h_{Beam} = 0.0020$m.

Section 3.2 was modified to simulate the experimental system. The modal formulation presented in section 3.1 is implemented with mode shapes $W_j(x)$ and natural frequencies ω_j that represents a cantilever beam. The base excitation results in a distributed inertial force on the beam when the coordinates are transformed to a frame attached to the boundary of the beam. Damping (ζ_i) is introduced into the modal oscillators (equation 3.31) to include the experimentally-observed modal damping of $\zeta_i = 0.015$. The impact on the beam is simulated using the CoR method presented in Subsection 3.1.4. Figure 3.15(a) shows the accelerations recorded experimentally near the impact point, Figure 3.15(b) and 3.15(c) show the accelerations and displacements obtained numerically using the Hertzian contact theory. Figure 3.15 is from de Vorst et al. [21] [1]. Figure 3.15(d) shows the numerically obtained displacement from the CoR method. A CoR of 1 has been used in the simulations, as no impact damping was considered in the model by de Vorst et al. It can be seen from the figure that the displacements closely match with the numerical model. Unfortunately, the accelerations from our numerical model cannot be directly compared due to fact that the accelerations are infinite at the instant of impact. The model predicts the same period of motion that was obtained experimentally. Figure 3.15 shows period-1 motion—that is, for every one cycle of base motion, the beam impacts the base once. Figures 3.16 and 3.17 show period-2 motion.

[1]Permission was obtained from elsivier to reproduce the graphs from the paper [21]. The licence agreeement can be viewed at `http://s100.copyright.com/CustomerAdmin/PLF.jsp?lID=2009070_1247590419063`.

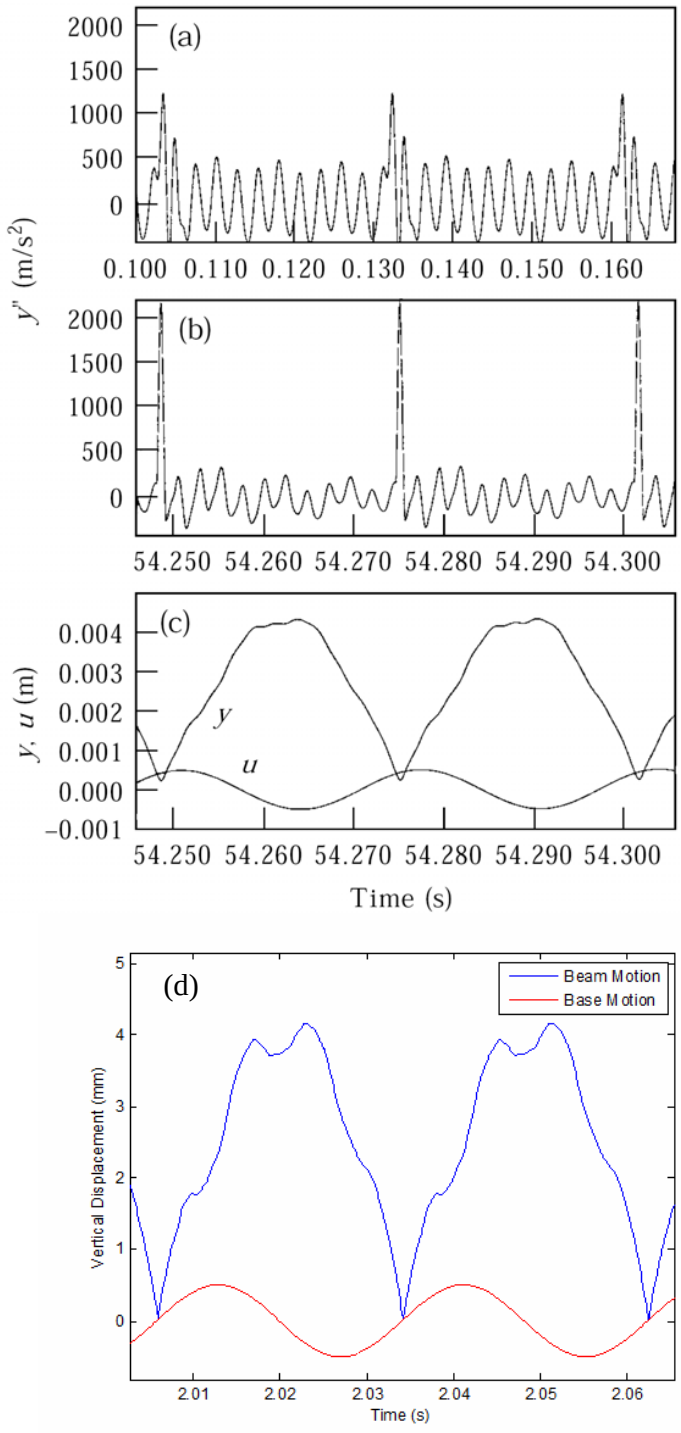

Figure 3.15: Comparison between experimental and numerical response at excitation frequency of 37.64 Hz: (a) experimentally observed acceleration, (b) acceleration obtained from simulation using Hertzian contact model, (c) displacement obtained from simulation using Hertzian contact model, (d) displacement obtained from simulation using coefficient of restitution model.

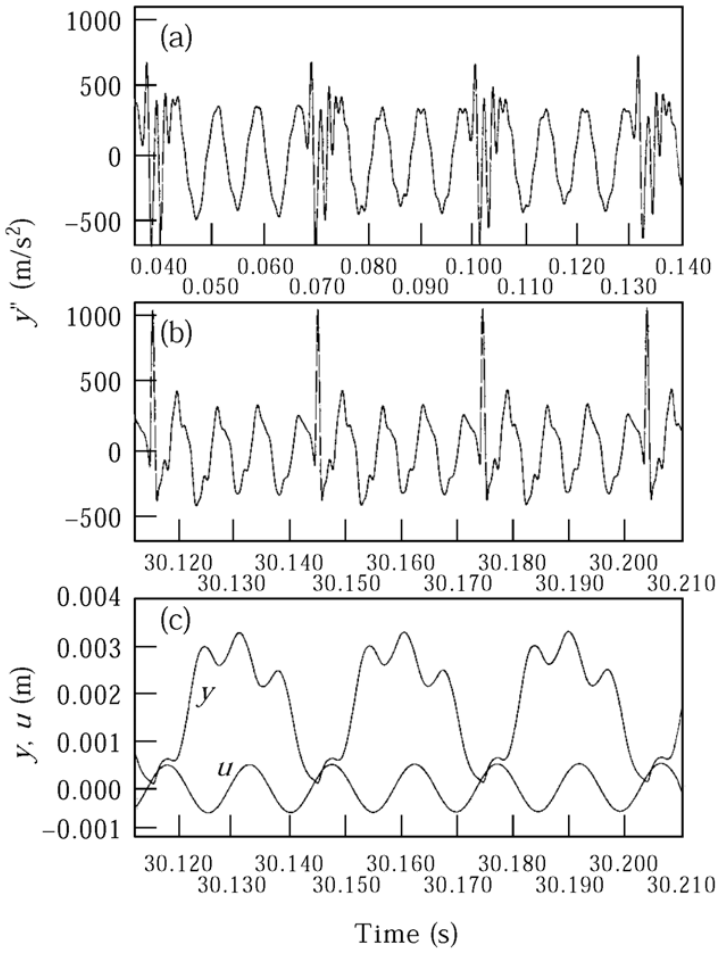

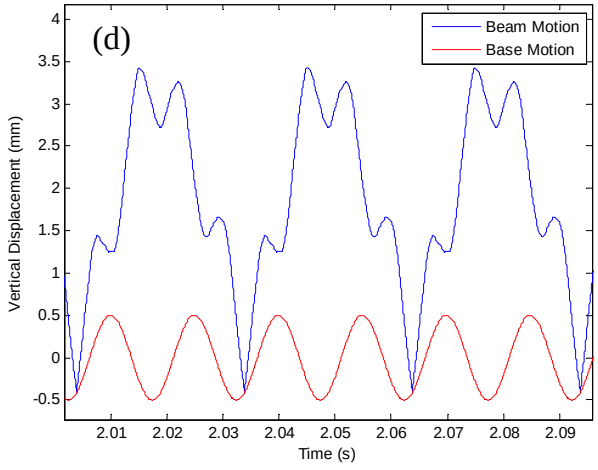

Figure 3.16: Comparison between experimental and numerical response at excitation frequency of 67.8 Hz: (a) experimentally observed acceleration, (b) acceleration obtained from simulation using Hertzian contact model, (c) displacement obtained from simulation using Hertzian contact model, (d) displacement obtained from simulation using coefficient of restitution model.

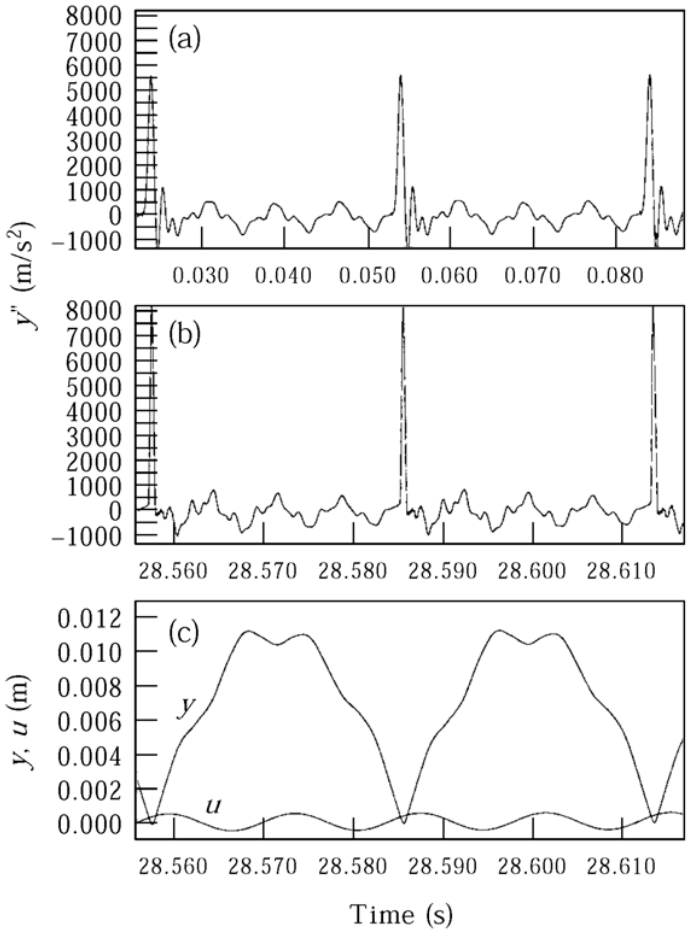

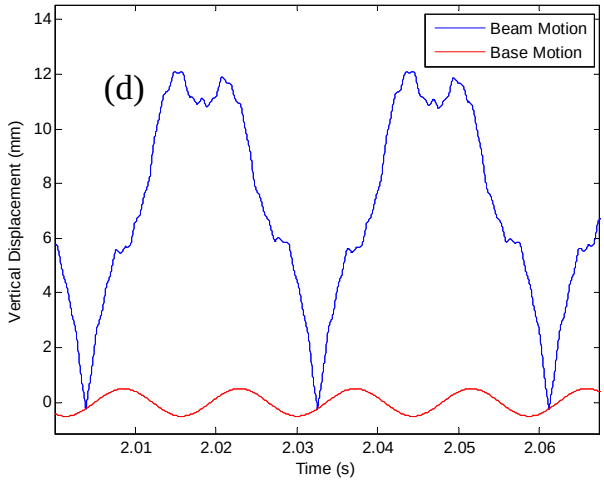

Figure 3.17: Comparison between experimental and numerical response at excitation frequency of 71.5 Hz: (a) experimentally observed acceleration, (b) acceleration obtained from simulation using Hertzian contact model, (c) displacement obtained from simulation using Hertzian contact model, (d)displacement obtained from simulation using coefficient of restitution model.

3.4 Chapter conclusions

It has been shown that the collocation-based CoR approach can introduce energy into a mechanical system for certain selections of collocation points. The new impulse-based CoR approach presented herein is energy-consistent and predicts a response that is very close to that obtained using the penalty approach. Moreover, the impulse-based CoR approach has been seen to provide increased computational efficiency over the penalty approach as the number of modes considered in the analysis is increased. The method has also been validated with experimental results from the existing literature. Although the impulse-based CoR method has only been applied to a vibro-impacting beam, the method can be applied to any continuous mechanical system that can be discretized using modal-based methods.

Chapter 4

Modelling the dynamics of a continuous system impacting a rigid distributed obstacle

In this chapter, we present a new moving boundary formulation for modelling the impact between a string and an obstacle. Hamilton's principle is used to obtain the equations of motion. Three different models are derived to represent the motion of the string during its three different phases of motion, and switching conditions are derived to switch between these models. An alternative formulation using a penalty approach is also proposed. Simulations from the models are studied to predict the behaviour of the string. The developed model is applied to study the dynamics of a sitar.

4.1 Mathematical modelling using a moving boundary approach

A schematic representation of the bridge-string geometry being investigated is shown in Figure 4.1. The bridge is a finite obstacle defined by a parabolic surface for values of X between Γ_1 and Γ_2. The string has fixed termination points on the X-axis at $X = L$ and on the parabola at $X = \Gamma_1$. The shape of the obstacle is assumed to be a parabola, as in the work of Burridge

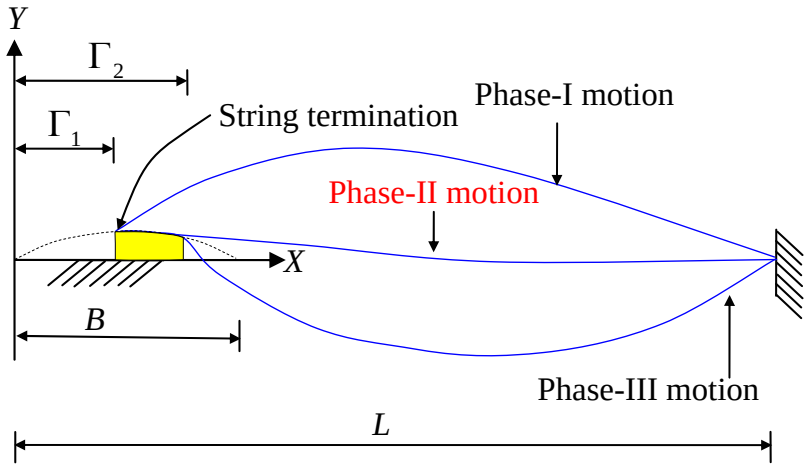

Figure 4.1: Bridge-string geometry and the three phases of string motion (exaggerated for clarity). The right string termination lies on the X-axis; the left termination lies on the parabolic bridge surface, as shown.

et al. [12], and the geometry can be represented analytically as:

$$Y_B(X) = A_P X(B - X) \tag{4.1}$$

The motion of the string can be divided into three distinct phases: phase-I motion occurs when there is no contact with the obstacle, partial wrapping on the obstacle is called phase-II motion, and a completely wrapped string is considered to be in phase-III motion. In this section we assume, for simplicity and without loss of generality, that $\Gamma_1 = 0$ and $\Gamma_2 = B$. The equation of motion governing the dynamics of the string during each of the three phases is derived, as are the corresponding switching conditions as the string passes between the phases. This approach is more general than that of Burridge et al. [12], who only consider phase-II motion because the parabola in their model extends indefinitely below the string.

4.1.1 Phase-I motion

During phase-I motion, the string is governed by the following classical string equation:

$$\rho A \frac{\partial^2 Y_1}{\partial t^2} - T \frac{\partial^2 Y_1}{\partial X^2} = 0 \tag{4.2}$$

with boundary conditions:

$$Y_1(0, t) = Y_1(L, t) = 0 \tag{4.3}$$

where Y_1 is the transverse displacement of the string, L is the length of the string, T is the string tension, ρ is the density, A is the cross-sectional area, X is the coordinate along the length, and t is the time. We substitute the following non-dimensional parameters into the equation of motion to facilitate our analysis:

$$y_1 = \frac{Y_1}{h}, \quad x = \frac{X}{L}, \; \tau = t\sqrt{\frac{T}{\rho A L^2}} \tag{4.4}$$

where $h = A_P B^2/4$ is the height of the obstacle. The equation of motion after substituting the non-dimensional variables is as follows:

$$\frac{\partial^2 y_1}{\partial \tau^2} - \frac{\partial^2 y_1}{\partial x^2} = 0 \tag{4.5}$$

with boundary conditions:

$$y_1(0,\tau) = y_1(1,\tau) = 0 \tag{4.6}$$

A solution to equation 4.5 is assumed to be of the form:

$$y_1(x,\tau) = \sum_{k=1}^{N} \phi_k(x)\eta_k(\tau) \tag{4.7}$$

In equation 4.7, $\phi_k(x) = \sqrt{2}\sin(k\pi x)$ are mass-normalized mode shapes of the string and $\eta_k(\tau)$ are modal coordinates. Substituting equation 4.7 into equation 4.5, multiplying by $\phi_j(x)$, integrating over the domain, and simplifying the resulting equation by using orthogonality relations results in a set of uncoupled ordinary differential equations of the following form:

$$\ddot{\eta}_k(\tau) + \omega_{1k}^2 \eta_k(\tau) = 0 \quad k = 1, 2, ..., N \tag{4.8}$$

where $\omega_{1k} = k\pi$ are the natural frequencies of the string. The modal initial conditions corresponding to physical initial conditions of $y_1(x,0)$ and $\dot{y}_1(x,0)$ are as follows:

$$\eta_k(0) = \int_0^1 y_1(x,0)\phi_k(x)dx \quad \text{and} \quad \dot{\eta}_k(0) = \int_0^1 \dot{y}_1(x,0)\phi_k(x)dx \tag{4.9}$$

The velocity of the string during phase-I motion is given by the following expression:

$$\frac{\partial y_1(x,\tau)}{\partial \tau} = \sum_{k=1}^{N} \phi_k(x)\dot{\eta}_k(\tau) \tag{4.10}$$

After specifying the system parameters and initial conditions, the modal equations of motion given by equation 4.8 can be integrated analytically or numerically. When the string begins contacting the obstacle, the equation of motion given by equation 4.8 is no longer valid. In the next section, we derive the equation of motion that describes the wrapping of the string around the obstacle using Hamilton's principle.

4.1.2 Phase-II motion

The variational principle involving a spatial constraint can be written as follows [29]:

$$\delta I = \delta \int_{t_1}^{t_2} \left[\int_0^{\Gamma_-(t)} (\Pi + \lambda G)\, dX + \int_{\Gamma_+(t)}^{L} \Pi dX \right] dt = 0 \tag{4.11}$$

where Π is the Lagrangian density function defined as:

$$\Pi = \frac{1}{2}\rho A \left(\frac{\partial Y_2(x,t)}{\partial t} \right)^2 - \frac{1}{2} T \left(\frac{\partial Y_2(X,t)}{\partial X} \right)^2 \tag{4.12}$$

G is the gap function, defined as $G(X,t) = Y_2(X,t) - Y_B(X)$, Γ is the wrapped string length, Y_2 is the displacement of the string during the wrapping motion, and λ is the unknown Lagrange multiplier function in the domain $0 \leq X \leq \Gamma_-(t)$. Substituting equation 4.12 into equation 4.11 we get:

$$\begin{aligned} \delta I &= \delta \int_{t_1}^{t_2} \left[\int_0^{\Gamma_-(t)} \frac{1}{2}\rho A \left(\frac{\partial Y_2(X,t)}{\partial t} \right)^2 dX - \int_0^{\Gamma_-(t)} \frac{1}{2} T \left(\frac{\partial Y_2(X,t)}{\partial X} \right)^2 dX \right. \\ &+ \int_0^{\Gamma_-(t)} \lambda G(X,t) dX + \int_{\Gamma_+(t)}^{L} \frac{1}{2}\rho A \left(\frac{\partial Y_2(X,t)}{\partial t} \right)^2 dX \\ &- \left. \int_{\Gamma_+(t)}^{L} \frac{1}{2} T \left(\frac{\partial Y_2(X,t)}{\partial X} \right)^2 dX \right] dt \end{aligned} \tag{4.13}$$

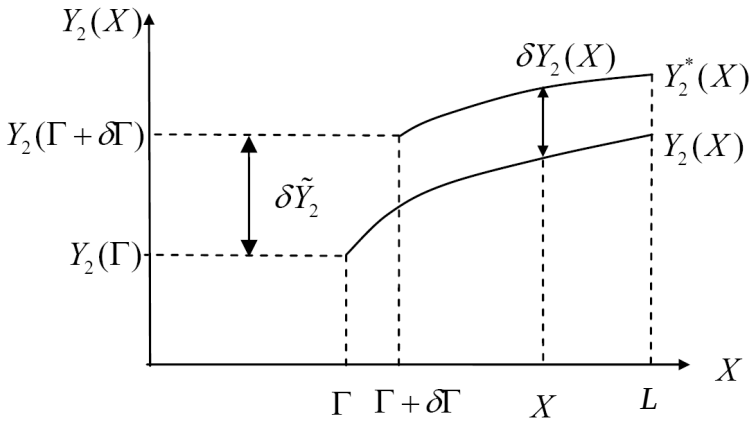

Figure 4.2: Actual and varied path at the moving boundary (separation point)

After evaluating the variations in equation 4.13, we arrive at the following:

$$\begin{aligned}
\delta I &= \int_{t_1}^{t_2}\int_{0}^{\Gamma_-(t)} \left(T\frac{\partial^2 Y_2(X,t)}{\partial X^2} - \rho A\frac{\partial^2 Y_2(X,t)}{\partial t^2} + \lambda\right)\delta Y_2(X,t)dXdt \\
&+ \int_{t_1}^{t_2}\int_{0}^{\Gamma_-(t)} (G(X,t)\delta\lambda)dXdt \\
&+ \int_{t_1}^{t_2}\int_{\Gamma_+(t)}^{L} \left(T\frac{\partial^2 Y_2(X,t)}{\partial X^2} - \rho A\frac{\partial^2 Y_2(X,t)}{\partial t^2}\right)\delta Y_2(X,t)dXdt \\
&+ \int_{t_1}^{t_2} \left(T\frac{\partial Y_2(\Gamma_+(t),t)}{\partial X}\delta Y_2(\Gamma_+(t),t)\right)dt \\
&- \int_{t_1}^{t_2} \left(T\frac{\partial Y_2(\Gamma_-(t),t)}{\partial X}\delta Y_2(\Gamma_-(t),t)\right)dt \\
&+ \int_{t_1}^{t_2} \left(T\frac{\partial Y_2(0,t)}{\partial X}\delta Y_2(0,t)\right)dt \\
&- \int_{t_1}^{t_2} \left(T\frac{\partial Y_2(L,t)}{\partial X}\delta Y_2(L,t)\right)dt = 0
\end{aligned} \tag{4.14}$$

4.1.2.1 Relation between variations in $\delta Y_2(\Gamma(t),t)$ and $\delta\Gamma(t)$

It should be noted that the variations $\delta Y_2(\Gamma(t),t)$ and $\delta\Gamma(t)$ are unspecified, but they are related due to the presence of the geometrical constraint. We derive the relationship between them following Fung and Chen [29]. Figure 4.2 shows the actual ($Y_2(X,t)$) and varied ($Y_2^*(X,t)$) paths in Y_2 over the X plane It can be seen from the figure that $\delta Y_2(X,t) = Y_2^*(X,t) - Y_2(X,t)$ has meaning only in the interval $[\Gamma(t)+\delta\Gamma(t), L]$, as $Y_2^*(X,t)$ is not defined in the interval $[\Gamma(t), \Gamma(t)+\delta\Gamma(t)]$. The following relationship for $\delta\tilde{Y}_2$ can be derived by exploiting the geometry

in Figure 4.2:

$$\begin{aligned}\delta\tilde{Y_2} &= Y_2^*(\Gamma(t)+\delta\Gamma(t),t) - Y_2(\Gamma(t),t) \doteq Y_2^*(\Gamma(t),t) + \frac{\partial Y_2(\Gamma(t),t)}{\partial X}\delta\Gamma(t) - Y_2(\Gamma(t),t) \\ &= \frac{\partial Y_2(\Gamma(t),t)}{\partial X}\delta\Gamma(t) + \delta Y_2(\Gamma(t),t) \end{aligned} \tag{4.15}$$

The point $\Gamma(t)+\delta\Gamma(t)$ of the varied path should also satisfy the geometrical constraint, which gives the following relation:

$$G(Y_2^*(\Gamma(t)+\delta\Gamma(t),t),\Gamma(t)+\delta\Gamma(t)) = 0 \tag{4.16}$$

Substituting for $Y_2^*(\Gamma(t)+\delta\Gamma(t),t) = Y_2(\Gamma(t),t) + \delta\tilde{Y_2}$ (equation 4.15), we get:

$$G(Y_2(\Gamma(t),t) + \delta\tilde{Y_2},\Gamma(t)+\delta\Gamma(t)) = 0 \tag{4.17}$$

which can be written as:

$$G(Y_2(\Gamma(t),t) + \delta\tilde{Y_2},\Gamma(t)+\delta\Gamma(t)) = G(Y_2(\Gamma(t),t),\Gamma(t)) + \frac{\partial G}{\partial Y_2(\Gamma(t),t)}\delta\tilde{Y_2} + \frac{\partial G}{\partial\Gamma(t)}\delta\Gamma(t) = 0 \tag{4.18}$$

The following relations can be used to simplify equation 4.18

$$G(Y_2(\Gamma(t),t),\Gamma(t)) = Y_2(\Gamma(t),t) - A_p\Gamma(t)(B-\Gamma(t)) = 0 \tag{4.19}$$

$$\frac{\partial G(Y_2(\Gamma(t),t),\Gamma(t))}{\partial Y_2(\Gamma(t),t)} = 1 \tag{4.20}$$

$$\frac{\partial G(Y_2(\Gamma(t),t),\Gamma(t))}{\partial\Gamma(t)} = -A_p(B-2\Gamma) \tag{4.21}$$

Substituting equations 4.19, 4.20, and 4.21 into equation 4.18, we get:

$$\delta\tilde{Y_2} - A_p(2\Gamma(t)-B)\delta\Gamma(t) = 0 \tag{4.22}$$

Substituting equation 4.15 into equation 4.22, we get:

$$\frac{\partial Y_2(\Gamma,t)}{\partial X}\delta\Gamma + \delta Y_2(\Gamma,t) - A_p(B-2\Gamma)\delta\Gamma = 0 \tag{4.23}$$

which, when rearranged, gives:

$$\left[A_p(B-2\Gamma) - \frac{\partial Y_2(\Gamma,t)}{\partial X}\right]\delta\Gamma = \delta Y_2(\Gamma,t) \tag{4.24}$$

Now substituting equation 4.24 into the fourth and fifth terms of equation 4.14, we have:

$$\begin{aligned}
\delta I &= \int_{t_1}^{t_2}\int_{0}^{\Gamma_-}\left(T\frac{\partial^2 Y_2(X,t)}{\partial X^2}-\rho A\frac{\partial^2 Y_2(X,t)}{\partial t^2}+\lambda\right)\delta Y_2(X,t)dXdt \\
&+ \int_{t_1}^{t_2}\int_{0}^{\Gamma_-}\left((G(X,t)\delta\lambda\right)dXdt \\
&+ \int_{t_1}^{t_2}\int_{\Gamma_+}^{L}\left(T\frac{\partial^2 Y_2(X,t)}{\partial X^2}-\rho A\frac{\partial^2 Y_2(X,t)}{\partial t^2}\right)\delta Y_2(X,t)dXdt \\
&+ \int_{t_1}^{t_2}\left(T\frac{\partial Y_2(\Gamma_+(t),t)}{\partial X}\left(A_p(B-2\Gamma_+(t))-\frac{\partial Y_2(\Gamma_+(t),t)}{\partial X}\right)\right)\delta\Gamma_+(t)dt \\
&- \int_{t_1}^{t_2}\left(T\frac{\partial Y_2(\Gamma_-(t),t)}{\partial X}\left(A_p(B-2\Gamma_-(t))-\frac{\partial Y_2(\Gamma_-(t),t)}{\partial X}\right)\right)\delta\Gamma_-(t)dt \\
&+ \int_{t_1}^{t_2}\left(T\frac{\partial Y_2(0,t)}{\partial X}\delta Y_2(0,t)\right)dt \\
&- \int_{t_1}^{t_2}\left(T\frac{\partial Y_2(L,t)}{\partial X}\delta Y_2(L,t)\right)dt = 0
\end{aligned} \tag{4.25}$$

In equation 4.25, the variations in $\delta Y_2(X,t)$ and $\delta\lambda$ are arbitrary and the values of $Y_2(0,t)=0$, $Y_2(L,t)=0$ are specified, so we have the following equations of motion that must be satisfied for all time:

$$\rho A\frac{\partial^2 Y_2(X,t)}{\partial t^2}-T\frac{\partial^2 Y_2(X,t)}{\partial X^2}-\lambda=0 \qquad 0<X<\Gamma_-(t) \tag{4.26}$$

$$\rho A\frac{\partial^2 Y_2(X,t)}{\partial t^2}-T\frac{\partial^2 Y_2(X,t)}{\partial X^2}=0 \qquad \Gamma_+(t)<X<L \tag{4.27}$$

with boundary conditions:

$$Y_2(0,t)=0,\ Y_2(\Gamma_-(t),t)=A_P\Gamma_-(t)(B-\Gamma_-(t)) \tag{4.28}$$

$$Y_2(L,t)=0,\ \ Y_2(\Gamma_+(t),t)=A_P\Gamma_+(t)(B-\Gamma_+(t)) \tag{4.29}$$

and from the fact that the variations in $\delta\Gamma_\pm(t)$ are arbitrary, we must have the following condition (transversality) that must be satisfied at the free boundary:

$$\frac{\partial Y_2(\Gamma_\pm(t),t)}{\partial X}=A_P\left(B-2\Gamma_\pm(t)\right) \tag{4.30}$$

The transversality condition is the necessary condition that must be satisfied for the variations to vanish at the free boundary, Γ. The physical interpretation of the transversality condition is that the slope of the string must be equal to the slope of the parabola at the point of separation $(\Gamma(t))$.

4.1.2.2 Dimensionless equation of motion during phase-II motion

We substitute the same non-dimensional parameters given in equation 4.4, along with $\gamma = \Gamma/L$, $b = B/L$, and $\alpha = 4L^2/B^2$, into equations (4.26-4.30). It should be noted that the solution of equation 4.26 is the geometry of the parabola, as the string in the domain $0 < x < \gamma_-(\tau)$ perfectly wraps around the obstacle. As such, we need only solve for the motion of the string in the domain $\gamma_+(\tau) < x < 1$ and solve for $\gamma_+(\tau)$. Thus, the equation of motion after replacing $\gamma_+(\tau)$ with $\gamma(\tau)$ reduces to the following moving boundary problem:

$$\frac{\partial^2 y_2(x,\tau)}{\partial \tau^2} - \frac{\partial^2 y_2(x,\tau)}{\partial x^2} = 0, \quad \gamma(\tau) < x < 1 \tag{4.31}$$

$$y_2(\gamma(\tau),\tau) = \alpha\gamma(\tau)(b-\gamma(\tau)), \quad y_2(1,\tau) = 0 \tag{4.32}$$

One further equation is required in order to obtain the separation point (moving boundary), which comes from the tranversality condition:

$$\frac{\partial y_2(\gamma(\tau),\tau)}{\partial x} = \alpha\left(b - 2\gamma(\tau)\right) \tag{4.33}$$

4.1.2.3 Approximate solution during phase-II motion

The boundary conditions in equation 4.32 are non-homogeneous, so it is difficult to apply the Galarkin method directly to solve equation 4.31. To transform the non-homogeneous boundary conditions given by equation 4.32 into homogeneous boundary conditions, the following variable transformation defining $y_3(x,\tau)$ is substituted into equations 4.31-4.33:

$$y_2(x,\tau) = y_3(x,\tau) + s(x,\tau) \tag{4.34}$$

where:

$$s(x,\tau) = \frac{\alpha\gamma(\tau)(b-\gamma(\tau))}{(\gamma(\tau)-1)}(x-1) \tag{4.35}$$

To obtain the function $s(x,\tau)$, we freeze time and solve for the static contact problem of equation 4.31. For a given $\gamma(\tau)$, the problem now reduces to:

$$\frac{\partial^2 y_2(x,\tau)}{\partial x^2} = 0, \quad \gamma(\tau) < x < 1 \tag{4.36}$$

with the following boundary conditions:

$$y_2(\gamma(t),\tau) = \alpha\gamma(\tau)(b-\gamma(\tau)), \quad y_2(1,\tau) = 0 \tag{4.37}$$

Equation 4.36 has the following solution:

$$y_2(x,\tau) = s(x,\tau) = C_1 x + C_2 \tag{4.38}$$

Substituting equation 4.38 into the boundary conditions given in equation 4.37 and solving for C_1 and C_2 gives the following static solution:

$$s(x,\tau) = \frac{\alpha\gamma(\tau)(b-\gamma(\tau))}{(\gamma(\tau)-1)}(x-1) \tag{4.39}$$

Although we have frozen time to obtain the above expression, this static solution is valid for any value of $\gamma(\tau)$. Substituting the variable transformation (equation 4.34) into equation 4.31 we get:

$$\frac{\partial^2}{\partial x^2}\left(y_3(x,\tau)+s(x,\tau)\right) - \frac{\partial^2}{\partial \tau^2}\left(y_3(x,\tau)+s(x,\tau)\right) = 0, \quad \gamma(\tau) < x < 1 \tag{4.40}$$

Simplifying the above equation using the relation $\frac{\partial^2 s(x,\tau)}{\partial x^2} = 0$, we get:

$$\frac{\partial^2 y_3(x,\tau)}{\partial \tau^2} - \frac{\partial^2 y_3(x,\tau)}{\partial x^2} = -\frac{\partial^2 s(x,\tau)}{\partial t^2}, \quad \gamma(\tau) < x < 1 \tag{4.41}$$

we now substitute the variable transformation (equation 4.34) into the boundary conditions given in equation 4.32:

$$y_3(\gamma(\tau),\tau) + s(\gamma(\tau),\tau) = \alpha\gamma(\tau)(b-\gamma(\tau)) \tag{4.42}$$

Evaluating $s(\gamma(\tau),\tau)$ from equation 4.39, we have:

$$y_3(\gamma(\tau),\tau) = 0 \tag{4.43}$$

Similarly, substituting equation 4.34 into the other boundary condition, we get:

$$y_2(1,\tau) = y_3(1,\tau) + s(1,\tau) = 0 \tag{4.44}$$

Evaluating $s(1,\tau)$ from equation 4.39, we have:

$$y_3(1,\tau) = 0 \tag{4.45}$$

After substituting the variable transformation into the transversality condition, we arrive at the following:

$$\frac{\partial y_3(\gamma(\tau),\tau)}{\partial x} = \alpha\left(b - 2\gamma(\tau)\right) - \frac{\alpha\gamma(\tau)(b-\gamma(\tau))}{(\gamma(\tau)-1)} \tag{4.46}$$

It can be seen that the boundary conditions (equation 4.43 and equation 4.44) are homogeneous.

4.1.2.4 Galerkin approximation

Since the domain of the problem is changing due to the time-dependent moving boundary, the basis functions we must choose in the Galerkin approximation should also be time-dependent. This particular solution procedure was used by Fung and Chen [29] for solving the contact problem of a beam wraping around a cylindrical obstacle. This method was also used by Wang and Wei [79] to study the vibrations in a moving flexible arm, and Yuksel and Gurgoze [33] to study the vibrations in an elastic manipulator with a prismatic joint. We assume a solution of the following form:

$$y_3(x,\tau) = \sum_{k=1}^{N} \psi_k(x,\tau)\beta_k(\tau) \tag{4.47}$$

The time-dependent basis function that must be chosen should satisfy the time-dependent boundary conditions (equations 4.43 and 4.44) at all times. Again, we freeze time and for a given $\gamma(\tau)$, we consider the following boundary value problem with the unknown frequency parameter $\Omega_2^2(\tau)$:

$$\frac{d^2\psi(x,\tau)}{dx^2} + \Omega_2^2(\tau)\psi(x,\tau) = 0 \tag{4.48}$$

with boundary conditions:

$$\psi(\gamma((\tau),\tau) = 0 \text{ and } \psi(1,t) = 0 \tag{4.49}$$

A solution satisfying equation 4.45 can be written as:

$$\psi(x,\tau) = A_1 \sin\left(\Omega_2(\tau)(x-\gamma(\tau))\right) + A_2 \cos\left(\Omega_2(\tau)(x-\gamma(\tau))\right) \tag{4.50}$$

Evaluating the above solution at the boundary conditions, we get:

$$\psi(\gamma(\tau),\tau) = A_2 = 0 \tag{4.51}$$

and:

$$\psi(1,\tau) = A_1 \sin\left(\Omega_2(\tau)(1-\gamma(\tau))\right) = 0 \tag{4.52}$$

For a non-trivial solution, we must have:

$$\Omega_2(\tau) = \omega_{2k} = \frac{k\pi}{(1-\gamma(\tau))} \quad k = 1, 2, ..., N \tag{4.53}$$

Substituting equations 4.51 and 4.53 into equation 4.50, we get:

$$\psi_k(x,\tau) = A_1 \sin\left(k\pi\left(\frac{x-\gamma(\tau)}{1-\gamma(\tau)}\right)\right) \tag{4.54}$$

Even though we have frozen time in deriving the above expression, the above functions satisfy the boundary conditions given by equations 4.43 and 4.45 at all times. Substituting the solution (equation 4.50) into equation 4.41, we have:

$$\frac{\partial^2}{\partial\tau^2}\left(\sum_{k=1}^{N}\psi_k(x,\tau)\beta_k(\tau)\right)-\frac{\partial^2}{\partial x^2}\left(\sum_{k=1}^{N}\psi_k(x,\tau)\beta_k(\tau)\right)=-\frac{\partial^2 s(x,\tau)}{\partial t^2} \tag{4.55}$$

$$\sum_{k=1}^{N}\psi_k(x,\tau)\ddot{\beta}_k(\tau)+\sum_{k=1}^{N}2\frac{\partial\psi_k(x,\tau)}{\partial t}\dot{\beta}_k(\tau)+\sum_{k=1}^{N}\frac{\partial^2\psi_k(x,\tau)}{\partial t^2}\beta_k(\tau)-\sum_{k=1}^{N}\frac{\partial^2\psi_k(x,\tau)}{\partial x^2}\beta_k(\tau)=-\frac{\partial^2 s(x,\tau)}{\partial\tau^2} \tag{4.56}$$

Now, multiplying both sides of the above equation with $\psi_j(x,\tau)$ and integrating over the domain $\gamma(\tau)<x<1$, we have:

$$\begin{aligned}
&\sum_{k=1}^{N}\ddot{\beta}_k\int_{\gamma(\tau)}^{1}(\tau)\psi_k(x,\tau)\psi_j(x,\tau)dx+\sum_{k=1}^{N}2\dot{\beta}_k(\tau)\int_{\gamma(\tau)}^{1}\frac{\partial\psi_k(x,\tau)}{\partial t}\psi_j(x,t)dx\\
+\quad&\sum_{k=1}^{N}\beta_k(\tau)\int_{\gamma(\tau)}^{1}\frac{\partial^2\psi_k(x,\tau)}{\partial t^2}\psi_j(x,\tau)dx-\sum_{k=1}^{N}\beta_k(\tau)\int_{\gamma(\tau)}^{1}\frac{\partial^2\psi_k(x,\tau)}{\partial x^2}\psi_j(x,\tau)dx=\\
-\quad&\int_{\gamma(\tau)}^{1}\frac{\partial^2 s(x,\tau)}{\partial t^2}\psi_j(x,\tau),\quad j=1,2,..,N
\end{aligned} \tag{4.57}$$

Now calculating the first integral in equation 4.57, we get:

$$\begin{aligned}
\int_{\gamma(\tau)}^{1}\psi_j(x,\tau)\psi_k(x,\tau)dx &= A_1^2\int_{\gamma(\tau)}^{1}\sin\left(j\pi\left(\frac{x-\gamma(\tau)}{1-\gamma(\tau)}\right)\right)\sin\left(k\pi\left(\frac{x-\gamma(\tau)}{1-\gamma(\tau)}\right)\right)dx\\
&= A_1^2\left(\frac{1-\gamma(\tau)}{2}\right)\delta_{jk}
\end{aligned} \tag{4.58}$$

We choose the amplitude of function $\psi_j(x,\tau)$ to be $\sqrt{\frac{2}{1-\gamma(\tau)}}$, so the right-hand side of the above equation becomes δ_{jk}. Now we evaluate the following integral shown below:

$$\begin{aligned}
&\int_{\gamma(\tau)}^{1}\frac{\partial^2\psi_j(x,\tau)}{\partial x^2}\psi_k(x,\tau)dx\\
=-\quad&\frac{2}{1-\gamma(\tau)}\left(\frac{j\pi}{(1-\gamma(\tau))}\right)^2\int_{\gamma(\tau)}^{1}\sin\left(j\pi\left(\frac{x-\gamma(\tau)}{1-\gamma(\tau)}\right)\right)\sin\left(k\pi\left(\frac{x-\gamma(\tau)}{1-\gamma(\tau)}\right)\right)dx\\
=-\quad&\left(\frac{j\pi}{(1-\gamma(\tau))}\right)^2\delta_{jk}
\end{aligned} \tag{4.59}$$

Substituting the integral evaluations given by equations 4.58 and 4.59 into equation 4.57, and noting that the indices j and k are interchangeable, we have:

$$\begin{aligned} & \ddot{\beta}_k(\tau) + 2\left[\sum_{j=1}^{N}\int_{\gamma(\tau)}^{1}\frac{\partial\psi_j(x,\tau)}{\partial\tau}\psi_k(x,\tau)dx\right]\dot{\beta}_k(\tau) \\ + & \left[\left(\frac{k\pi}{(1-\gamma(\tau))}\right)^2 + \sum_{j=1}^{N}\int_{\gamma(\tau)}^{1}\frac{\partial^2\psi_j(x,\tau)}{\partial\tau^2}\psi_k(x,\tau)dx\right]\beta_k(\tau) \\ = & \int_{\gamma(\tau)}^{1}\frac{\partial^2 s(x,\tau)}{\partial t^2}\psi_k(x,\tau)dx, \quad k=1,2,...,N \end{aligned} \tag{4.60}$$

The above equation can now be written as:

$$\begin{aligned} & \ddot{\beta}_k(\tau) + \left[\sum_{j=1}^{N} 2C_{jk}(\gamma(\tau),\dot{\gamma}(\tau))\right]\dot{\beta}_k(\tau) \\ + & \left[\left(\frac{k\pi}{(1-\gamma(\tau))}\right)^2 + \sum_{k=1}^{N} D_{jk}(\gamma(\tau),\dot{\gamma}(\tau),\ddot{\gamma}(\tau))\right]\beta_k(\tau) \\ = & -E_k(\gamma(\tau),\dot{\gamma}(\tau),\ddot{\gamma}(\tau)), \quad k=1,2,...,N \end{aligned} \tag{4.61}$$

where C_{jk}, D_{jk}, and E_k are defined as follows:

$$C_{jk}(\gamma(\tau),\dot{\gamma}(\tau)) = \int_{\gamma(\tau)}^{1}\frac{\partial\psi_j(x,\tau)}{\partial\tau}\psi_k(x,\tau)dx = J_{1kj}(\gamma(\tau))\dot{\gamma}(\tau) \tag{4.62}$$

$$\begin{aligned} D_{jk}(\gamma(\tau),\dot{\gamma}(\tau),\ddot{\gamma}(\tau)) &= \int_{\gamma(\tau)}^{1}\frac{\partial^2\psi_j(x,\tau)}{\partial\tau^2}\psi_k(x,\tau)dx \\ &= J_{1jk}(\gamma(\tau))\ddot{\gamma}(\tau) + J_{2jk}(\gamma(\tau))\dot{\gamma}(\tau)^2 \end{aligned} \tag{4.63}$$

$$\begin{aligned} E_k(\gamma(\tau),\dot{\gamma}(\tau),\ddot{\gamma}(\tau)) &= \int_{\gamma(\tau)}^{1}\frac{\partial^2 s(x,\tau)}{\partial\tau^2}\psi_k(x,\tau)dx \\ &= J_{3k}(\gamma(\tau))\dot{\gamma}(\tau)^2 + J_{4k}(\gamma(\tau))\ddot{\gamma}(\tau) \end{aligned} \tag{4.64}$$

In the above equations, J_{1jk}, J_{2jk}, J_{3jk}, and J_{4jk} are functions of $\gamma(\tau)$ only. Equation 4.61 is decoupled with respect to $\beta_k(\tau)$, but the coefficients are time-dependent and are functions of $\gamma(\tau)$, $\dot{\gamma}(\tau)$, and $\ddot{\gamma}(\tau)$. The time-dependent nature of the coefficients in equation 4.61 can be explained from the fact that the length of the string changes as the string starts to wrap around the obstacle, thus making the stiffness a function of time. It should be noted that $\gamma(\tau)$ is unknown and should be found as a part of the solution. The equation governing the dynamics

of $\gamma(\tau)$ will be obtained from the transversality condition (equation 4.46). After substituting the solution given by equation 4.47 into equation 4.46, we get:

$$\sum_{k=1}^{N} k\pi\sqrt{2}\beta_k(\tau) = (1-\gamma(\tau))^{3/2}\left(\alpha\left(b-2\gamma(\tau)\right) - \frac{\alpha\gamma(\tau)(b-\gamma(\tau))}{(\gamma(\tau)-1)}\right) \tag{4.65}$$

Differentiating the above equation with respect to time, we get:

$$\sum_{k=1}^{N} k\pi\sqrt{2}\dot{\beta}_k(\tau) = H_1(\gamma(\tau))\dot{\gamma}(\tau) \tag{4.66}$$

Differentiating again with respect to time gives:

$$\sum_{k=1}^{N} j\pi\sqrt{2}\ddot{\beta}_k(\tau) = H_1(\gamma(\tau))\ddot{\gamma}(\tau) + H_2(\gamma(\tau))\dot{\gamma}(\tau)^2 \tag{4.67}$$

In equation 4.67, H_1 and H_2 are functions of $\gamma(\tau)$. Equations 4.61 and 4.67 can be solved simultaneously for $\beta_k(\tau)$ and $\gamma(\tau)$ to predict the motion of the string in the transformed coordinates $y_3(x,t)$ during the contact phase. The above method of satisfying the second derivative of the displacement constraint rather than the displacement constraint directly, thus converting the constraint equation into a differential equation, is a well-known approach in the field of multi-body dynamics [58]. To get the actual motion of the string, $y_2(x,t)$, we use the transformation given in equation 4.34:

$$y_2(x,\tau) = \sum_{k=1}^{N} \psi_k(x,\tau)\beta_k(\tau) + \frac{\alpha\gamma(\tau)(b-\gamma(\tau))}{(\gamma(\tau)-1)}(x-1) \tag{4.68}$$

The velocity of the string, which is the partial derivative of the above expression with respect to time, is as follows:

$$\begin{aligned}\frac{\partial y_2(x,\tau)}{\partial\tau} &= \sum_{k=1}^{N}\frac{\partial\psi_k(x,\tau)}{\partial\tau}\beta_k(\tau) + \sum_{k=1}^{N}\psi_k(x,\tau)\dot{\beta}_k(\tau) \\ &+ \alpha(x-1)\left(\frac{(\gamma(\tau)-1)b\dot{\gamma}(\tau) - 2\gamma(\tau)\dot{\gamma}(t) - (b\gamma(\tau)-\gamma(\tau)^2)\dot{\gamma}(\tau)}{(\gamma(\tau)-1)^2}\right)\end{aligned} \tag{4.69}$$

4.1.3 Switching conditions between phase-I and phase-II motions

Let τ_{c1} be the time at which the string in phase-I motion comes in contact with the obstacle. The subscript c represents contact. The string in phase-I motion contacts the obstacle when

the slope of the string at $x = \gamma(\tau_{c1}) = 0$ matches the slope of the obstacle. At the event of contact, we have:

$$y_1(x, \tau_{c1}) = y_2(x, \tau_{c1}) \tag{4.70}$$

Substituting equation 4.7 and equation 4.68 into the above expression gives:

$$\sum_{k=1}^{N} \phi_k(x)\eta_k(\tau_{c1}) = \sum_{k=1}^{N} \psi_k(x, \tau_{c1})\beta_k(\tau_{c1}) + \frac{\alpha\gamma(\tau_{c1})(b - \gamma(\tau_{c1}))}{(\gamma(\tau_{c1}) - 1)}(x - 1) \tag{4.71}$$

Since $\gamma(\tau_{c1}) = 0$ at $\tau = \tau_{c1}$, we have:

$$\sum_{k=1}^{N} \phi_k(x)\eta_k(\tau_{c1}) = \sum_{k=1}^{N} \psi_k(x, \tau_{c1})\beta_k(\tau_{c1}) \tag{4.72}$$

Recalling the expression for $\psi_k(x, \tau)$:

$$\psi_k(x, \tau) = \sqrt{\frac{2}{1 - \gamma(\tau)}} \sin\left(k\pi\left(\frac{x - \gamma(\tau)}{1 - \gamma(\tau)}\right)\right) \tag{4.73}$$

and now substituting $\gamma(\tau_{c1}) = 0$ at time τ_{c1} into this expression, we have:

$$\psi_k(x, \tau_{c1}) = \sqrt{2}\sin(k\pi x) \tag{4.74}$$

It can be seen from the above expression that $\psi_k(x, \tau_{c1}) = \phi_k(x, \tau_{c1})$ at $\gamma(\tau_{c_1}) = 0$. Multiplying both sides of equation 4.72 with $\psi_j(x, \tau_{c1})$ and integrating over the domain, we have:

$$\sum_{k=1}^{N} \eta_k(\tau_{c1}) \int_0^1 \phi_k(x)\psi_j(x, \tau_{c1})dx = \sum_{k=1}^{N} \beta_k(\tau_{c1}) \int_0^1 \psi_k(x, \tau_{c1})\psi_j(x, \tau_{c1}) \tag{4.75}$$

Now evaluating the following integrals, we have:

$$\int_0^1 \phi_k(x)\psi_j(x, \tau_{c1})dx = \int_0^1 \psi_k(x, \tau_{c1}))\psi_j(x, \tau_{c1})dx = 2\int_0^1 \sin(j\pi x)\sin(k\pi x) = \delta_{jk} \tag{4.76}$$

Substituting the above relations into equation 4.75, we have:

$$\eta_k(\tau_{c1}) = \beta_k(\tau_{c1}), \quad k = 1, 2, ..., N \tag{4.77}$$

Since the velocity distributions in phase-I motion and phase-II motion should also be equal at transferring time τ_{c1}, we have:

$$\frac{\partial y_1(x, \tau_{c1})}{\partial \tau} = \frac{\partial y_2(x, \tau_{c1})}{\partial \tau} \tag{4.78}$$

Substituting 4.10 and equation 4.69 into the above expression for $\tau = \tau_{c1}$ and $x = \gamma(\tau_{c1}) = 0$, we have:

$$\sum_{k=1}^{N}(\tau_{c1})\phi_k(x)\dot{\eta}_k = \sum_{k=1}^{N}\left(\frac{\partial\psi_k(x,\tau_{c1})}{\partial\tau}\beta(\tau_{c1}) + \psi_k(x,\tau_{c1})\dot{\beta}_k(\tau_{c1})\right) - b\alpha\,(x-1)\,\dot{\gamma}(\tau_{c1}) \tag{4.79}$$

Multiplying both sides of equation 4.79 by $\psi_j(x,\tau_{c1})$ and integrating over the domain results in the following:

$$\sum_{k=1}^{N}\dot{\eta}_k(\tau_{c1})\int_0^1 \phi_k(x)\psi_j(x,\tau_{c1})dx \tag{4.80}$$

$$= \sum_{k=1}^{N}\beta_k(\tau_{c1})\int_0^1 \frac{\partial\psi_k(x,\tau_{c1})}{\partial\tau}\psi_j(x,\tau_{c1})dx \; + \sum_{k=1}^{N}\dot{\beta}_k(\tau_{c1})\int_0^1 \psi_k(x,\tau_{c1})\psi_j(x,\tau_{c1})dx$$

$$- \quad b\alpha\dot{\gamma}(\tau_{c1})\int_0^1 (x-1)\,\psi_j(x,\tau_{c1})dx \tag{4.81}$$

Evaluating the following integral, we get:

$$\int_0^1 (x-1)\psi_j(x,\tau_{c1})dx = \int_0^1 (x-1)\sqrt{2}\sin(j\pi x))dx = -\frac{\sqrt{2}}{j\pi} \tag{4.82}$$

Substituting the above equation and using the relations in equation 4.76, the above equation reduces to the following:

$$\dot{\eta}_k(\tau_{c1}) = \dot{\beta}_k(\tau_{c1}) + \left[\beta_k(\tau_{c1})\sum_{j=1}^{N}J_{1jk}(0) + \sqrt{2}\left(\frac{b\alpha}{k\pi}\right)\right]\dot{\gamma}(\tau_{c1}), \quad k = 1, 2, ..., N \tag{4.83}$$

where $J_{1jk}(0) = \int_0^1 \frac{\partial\psi_j(x,\tau_{c1})}{\partial\tau}\psi_k(x,\tau_{c1})dx$ (see equation 4.63). The above set of N equations contains $N+1$ unknowns, so we need one further equation to solve for $\dot{\gamma}(\tau_{c1})$, which can be obtained by differentiating the transversality condition given by equation 4.65 with respect to time:

$$\sum_{k=1}^{N}k\pi\sqrt{2}\dot{\beta}_k(\tau) = H_1(\gamma(\tau))\dot{\gamma}(\tau) \tag{4.84}$$

At the transferring time $\tau = \tau_{c1}$, the above equation becomes:

$$\dot{\gamma}(\tau_{c1}) = \frac{1}{H_1(0)}\sum_{k=1}^{N}k\pi\sqrt{2}\dot{\beta}_k(\tau_{c1}) \tag{4.85}$$

The above algebraic equations (4.83 and 4.85) can be solved to obtain $\dot{\beta}_k(\tau_{c1})$ and $\dot{\gamma}(\tau_{c1})$. The time of switching can be obtained through the transversality condition (equation 4.65):

$$\sum_{k=1}^{N} k\pi\sqrt{2}\eta_k(\tau_{c1}) = \sum_{k=1}^{N} k\pi\sqrt{2}\beta_k(\tau_{c1}) = \alpha b \tag{4.86}$$

Event-detection based on root-finding algorithms (Newton-Raphson, Secant method, or bisection method) can be used in the simulation to detect the time at which equation 4.86 holds. Once contact is detected, the initial conditions needed for phase-II motion can be obtained from equations 4.83 and 4.85, and the equations of motion (equation 4.61 and 4.67) can be integrated forward in time.

4.1.4 Phase-III motion

The Phase-III motion is the same as phase-I motion, except that the string is completely wrapped around the obstacle and vibrates between $x = \gamma(\tau) = b$ and $x = 1$. The dimensionless equation of motion of the string during phase-III can be written as:

$$\frac{\partial^2 y_4(x,\tau)}{\partial \tau^2} - \frac{\partial^2 y_4(x,\tau)}{\partial x^2} = 0, \qquad b < x < 1 \tag{4.87}$$

$$y_4(b,\tau) = 0, \quad y_4(1,\tau) = 0 \tag{4.88}$$

Substituting a solution of the following form:

$$y_4(x,\tau) = \sum_{k=1}^{N} \varphi_k(x) r_j(\tau) \tag{4.89}$$

into equation 4.87 and performing a standard modal analysis, we arrive at the following uncoupled ordinary differential equations:

$$\ddot{r}_k(\tau) + \omega_{3k}^2 r_k(\tau) = 0, \quad k = 1, 2, ..., N \tag{4.90}$$

where $\varphi_k(x) = \sqrt{2/(1-b)}\sin(k\pi(x-b)/(1-b))$ are the mass-normalized mode shapes of the string, $r_k(\tau)$ are the generalized coordinates, and $\omega_{3k} = k\pi/(1-b)$ are the natural frequencies of the string.

4.1.5 Switching conditions between phase-II and phase-III motions

Once the slope of the string at $x = \gamma = b$ matches the slope of the obstacle, the string enters into phase-III motion. Let τ_{c2} be the instant of switching. The displacement and velocity distributions of the string during the last instant of phase-II will be transferred to phase-III, which can be represented mathematically as:

$$\beta_k(\tau_{c2}) = r_k(\tau_{c2}), \quad k = 1, 2, ..., N \tag{4.91}$$

$$\dot{\beta}_k(\tau_{c2}) = \dot{r}_k(\tau_{c2}), \quad k = 1, 2, ..., N \tag{4.92}$$

The transfer time τ_{c2} between phase-II and phase-III can again be obtained from the transversality condition, as shown below: substituting $\tau = \tau_{c2}$ and $\gamma(\tau_{c2}) = b$ in equation 4.65, we have:

$$\sum_{k=1}^{N} k\pi\sqrt{2}\beta_k(\tau_{c2}) = -\alpha b(1-b)^{3/2} \tag{4.93}$$

4.1.6 Switching conditions between phase-III and phase-II motions

The switching conditions between phase-III and phase-II motions are similar to those used between phase-I and phase-II. Let τ_{c3} be the transfer time. Once the phase-III motion is initiated after time τ_{c2}, the string vibrates downwards between the boundaries b and 1. As the string starts to move upwards, its slope at $x = \gamma(\tau_{c3}) = b$ matches the slope of the obstacle and the string remains in phase-III motion. When the string begins unwrapping itself, it once again engages in phase-II motion. We now try to relate the initial conditions between phase-III and phase-II motions. Following a similar procedure as was employed in section 4.1.3, we obtain the following relations:

$$r_k(\tau_{c3}) = \beta_k(\tau_{c3}), \quad k = 1, 2, ..., N \tag{4.94}$$

$$\dot{r}_k(\tau_{c3}) = \dot{\beta}_k(\tau_{c3}) + \left[\beta_k(\tau_{c3})\sum_{j=1}^{N} J_{1kj}(b) + \sqrt{2}\left(\frac{b\alpha}{k\pi}\right)\right]\dot{\gamma}(\tau_{c3}), \quad k = 1, 2, ..., N \tag{4.95}$$

$$\dot{\gamma}(\tau_{c3}) = \frac{1}{H_1(b)}\sum_{k=1}^{N} k\pi\sqrt{2}\dot{\beta}_k(\tau_{c3}) \tag{4.96}$$

Equation 4.96 can be substituted into equation 4.95 to eliminate $\dot{\gamma}(\tau_{c3})$, which can then be

solved for $\dot{\beta}_k(t)$. Once the $\dot{\beta}_k(t)$ are known, they can be re-substituted into equation 4.96 to get $\dot{\gamma}(\tau_{c3})$. The transferring time $\tau = \tau_{c3}$ can again obtained from the transversality condition, as shown below:

$$\sum_{k=1}^{N} k\pi\sqrt{2}\beta_k(\tau_{c3}) = -\alpha b(1-b)^{3/2} \tag{4.97}$$

Equations 4.94-4.96 relate the initial conditions between phase-III and phase-II motions.

4.1.7 Switching conditions between phase-II and phase-I motions

The switching conditions between phase-II and phase-I motions are similar to those used between phase-II and phase-III. Let τ_{c4} be the switching time between phase-II and phase-I motion. When the string completely unwraps from the obstacle during phase-II motion, the slope of the string at $x = \gamma = 0$ matches the slope of the obstacle and phase-I motion is again initiated. Following a similar procedure as that used in section 4.1.5, we get the following relations:

$$\beta_k(\tau_{c4}) = \eta_k(\tau_{c4}), \quad k = 1, 2, ..., N \tag{4.98}$$

$$\dot{\beta}_k(\tau_{c4}) = \dot{\eta}_k(\tau_{c4}), \quad k = 1, 2, ..., N \tag{4.99}$$

The transfer time τ_{c4} between phase-II and phase-III can again be obtained from the transversality condition, as shown below:

$$\sum_{k=1}^{N} k\pi\sqrt{2}\beta_k(\tau_{c4}) = \alpha b \tag{4.100}$$

4.1.8 Summary of formulation

We now have the equations governing the dynamics of the string during the three phases of motion, given by equations 4.8, 4.61, and 4.90. The switching conditions between phase-I and phase-II motions are given by equations 4.77 and 4.85, and the event of switching can be obtained from equation 4.86. The switching conditions between phase-II and phase-III motions are given by equations 4.91 and 4.92, and the event of switching can be obtained from equation 4.93. During upward motion of the string, the switching conditions between phase-III and phase-II motions and the event of switching can be obtained from equations 4.94-4.96 and equation 4.97, respectively. Finally, the switching condition between phase-II and phase-I and the event of switching are given by equations 4.98-4.99 and 4.100.

4.2 Mathematical modelling using a penalty approach

In the penalty approach, the obstacle is not modelled as a constraint nor treated as a boundary condition. The constraint is penalized and is modelled as a distributed force in the PDE. The entire motion of the string can be modelled using only the phase-I motion, with an appropriate forcing term to simulate the impact. The equation of motion of the string-obstacle system can be written as:

$$\rho A \frac{\partial^2 Y_1}{\partial t^2} - T \frac{\partial^2 Y_1}{\partial X^2} = F(X,t) \tag{4.101}$$

with boundary conditions:

$$Y_1(0,t) = 0 \quad \text{and} \quad Y_1(L,t) = 0 \tag{4.102}$$

where ρ is the density, A is the area of cross-section, T is the tension, Y_1 is the transverse deformation, and t is the time. $F(X,t)$ is the distributed contact force generated due to the compression of the obstacle, and can be represented as:

$$F(X,t) = \begin{cases} K(X)G(X,t)^n \left[1 + \Lambda \frac{\partial G}{\partial t}\right] & \text{if} \quad G(X,t) \geq 0 \\ 0 & \text{if} \quad G(X,t) < 0 \end{cases} \tag{4.103}$$

where $G(X,t) = Y_B(X) - Y_1(X,t)$ is the gap function. The contact force is zero when the string does not contact the obstacle, and is finite when the string contacts the obstacle. The contact force is a nonlinear function of $G(X,t)$ and $\frac{\partial G}{\partial t}$. It should be noted that the contact stiffness and damping are generally nonlinear due to the variation of contacting geometries during impact as well as the local plastic deformations; the contact law given by equation 4.103 has parameters to account for both nonlinear stiffness (n) and dissipation (Λ).

The above contact law (equation 4.103) does not predict a nonzero force at the moment of impact as do linear visco-elastic contact models [43]. The contact model is an extension of the point contact model proposed by Hunt and Crossley [43] for distributed contacts, and has been developed by Gonthier et al. [31]. Although the main aim of the chapter is to simulate the sitar string with a parabolic obstacle, we also consider straight and sinusoidal obstacles to compare and validate our numerical model with the analytical results found in existing literature [13, 15].

The equation of the obstacle for various geometries can be represented as:

$$Y_B(X) = \begin{cases} -h, & 0 \le x \le L \quad \text{straight obstacle} \\ h\sin(2\pi X), & 0 \le x \le L \quad \text{sinusoidal obstacle} \\ hX(B-X), & 0 \le x \le B \quad \text{parabolic obstacle} \end{cases} \tag{4.104}$$

where h and B are the parameters defining the geometry. We introduce the following dimensionless parameters:

$$\begin{aligned} y_1 &= \frac{Y_1}{max(Y_B(X))},\ x = \frac{X}{L},\ \tau = t\sqrt{\frac{T}{\rho AL^2}},\ \widehat{\Lambda} = \Lambda h\sqrt{\frac{T}{\rho AL^2}}, \\ k(x) &= \frac{L^2 max(Y_B(X))^{n-1}K(X)}{T},\ \text{and } b = \frac{B}{L} \end{aligned} \tag{4.105}$$

where $Y_B(X)$ is the maximum height of the obstacle, which is h for straight and sinusoidal obstacles and $\frac{hB^2}{4}$ for parabolic obstacles. After substituting the non-dimensional parameters, the equation of motion becomes:

$$\frac{\partial^2 y_1}{\partial \tau^2} - \frac{\partial^2 y_1}{\partial \tau^2} = f(x,\tau) \tag{4.106}$$

with boundary conditions:

$$y_1(0,\tau) = 0 \ \text{ and } \ y_1(1,\tau) = 0 \tag{4.107}$$

The contact force now becomes:

$$f(x,\tau) = K \begin{cases} k(x)g(x,\tau)^n \left[1 + \widehat{\Lambda}\frac{\partial g}{\partial \tau}\right] & \text{if} \quad g(x,\tau) \ge 0 \\ 0 & \text{if} \quad g(x,\tau) < 0 \end{cases} \tag{4.108}$$

where $g(x,\tau) = y_B(x) - y_1(x,\tau)$ is the dimensionless gap function. The geometry of the obstacle can now be written as:

$$y_B(x) = \begin{cases} -1, & 0 \le x \le 1 \\ \sin(2\pi Lx), & 0 \le x \le 1 \\ \frac{4L^2}{B^2}x(b-x), & 0 \le x \le b \end{cases} \tag{4.109}$$

A solution to equation 4.106 is assumed to be of the form:

$$y_1(x,\tau) = \sum_{k=1}^{\infty} \phi_k(x)\eta_j(\tau) \tag{4.110}$$

In equation 4.110, $\phi_k(x) = \sqrt{2}\sin(k\pi x)$ are mass-normalized mode shapes of the string and $\eta_k(\tau)$ are modal coordinates. Substituting equation 4.110 into equation 4.106, multiplying by $\phi_k(x)$, integrating over the domain, and simplifying the resulting equation by using orthogonality relations results in a set of coupled integro-differential equations of the following form:

$$\ddot{\eta}_k(\tau) + \omega_{1k}^2 \eta_j(\tau) = \int_0^1 f(x,\tau)\phi_k(x)dx, \quad k = 1, 2, ..., N \tag{4.111}$$

where $f(x,\tau)$ is given by equation 4.108 and $\omega_{1k} = k\pi$ are the natural frequencies of the string. The modal initial conditions corresponding to the physical initial conditions of $y(x,0)$ and $\dot{y}(x,0)$ are as follows:

$$\eta_k(0) = \int_0^1 y_1(x,0)\phi_k(x)dx \quad \text{and} \quad \dot{\eta}_k(0) = \int_0^1 \dot{y_1}(x,0)\phi_k(x)dx \tag{4.112}$$

4.3 Results and discussion

In this section, we discuss the behaviour of the string motion observed in numerical simulations. For computational simplicity, we consider only a single-mode representation of the string. It will be evident shortly that even a one-mode approximation of the moving boundary formulation can capture the physics of the problem. This approximation requires the string to be plucked at the centre of its unwrapped length.

4.3.1 General behaviour of string motion

Since we have introduced dimensionless quantities in the equation of motion, the natural frequencies of the completely unwrapped string are integer multiples of π. For a simulation, we need two dimensionless quantities: the relationship between the bridge and string given by $b = B/L$, and the modal amplitude of the initial string configuration given by $\beta_1(0)$. The contact length $\gamma = 1 - \sqrt{(1-b)}$ for the string in static equilibrium on the parabolic obstacle can be obtained from the transversality condition (equation 4.65) by setting $\beta_1(0) = 0$; the string shape at static equilibrium, a straight line from the contact point to the right termination, is given by equations 4.34 and 4.35 with $y_3 = 0$.

Transitions between phases are controlled by two factors: (i) the location of the bridge terminations, as determined by γ_1 and γ_2; and (ii) the pluck amplitude, as given by the initial condition $\beta_1(0)$. The value of γ_1 constrains the left boundary of the vibrating string and shortens the effective speaking length at the phase-I transition; γ_2 constrains the potential extent of the string wrapping before it enters into phase-III motion. For each defined pair of bridge terminations, limiting values of the initial conditions such that the string only vibrates in phase-II motion can be obtained from the transversality condition (equation 4.65):

$$\frac{(1-\gamma_2)^{3/2}}{\sqrt{2}\pi}\left(\alpha\,(b-2\gamma_2)-\frac{\alpha\gamma_2(b-\gamma_2)}{(\gamma_2-1)}\right)<\beta_1(0)<\frac{(1-\gamma_1)^{3/2}}{\sqrt{2}\pi}\left(\alpha\,(b-2\gamma_1)-\frac{\alpha\gamma_1(b-\gamma_1)}{(\gamma_1-1)}\right) \tag{4.113}$$

The significance of these inequalities for sitar bridge design will be subsequently demonstrated. A parabolic bridge that extends to the x-axis on both sides, as used in the derivation of the equations of motion and switching conditions in the previous section, corresponds to $\gamma_1 = 0$ and $\gamma_2 = b$, in which case the inequalities constraining the string to phase-II motion simplify to $-4(1-b)^{3/2}/\sqrt{2}\pi b < \beta_1(0) < 1/\sqrt{2}\pi b$. The bridge configuration in Burridge et al. [12] corresponds to $\gamma_1 = 0$ and $\gamma_2 \to \infty$.

Figure 4.3 shows the variation of initial condition $\beta_1(0)$ against initial contact length $\gamma(0)$ for a string in phase-II configuration with $b = 0.05$, which is the value used by Burridge et al. [12]. The corresponding midpoint deflection $y_2(0.5, 0)$ is also shown. Interestingly, the initial

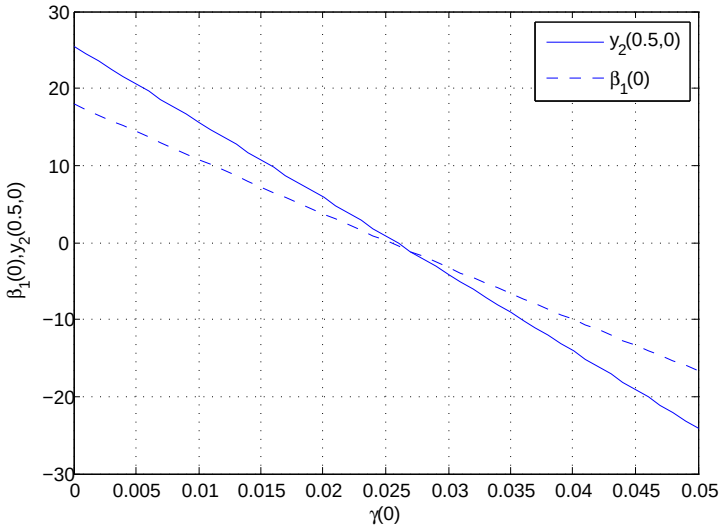

Figure 4.3: Variation of initial condition with initial contact length.

conditions seem to vary almost linearly with contact length. For this bridge configuration, the phase transitions occur when $\gamma(0)$ is 0 or 0.05, giving $\beta_1(0)$ values of 18.0 and -16.7, and corresponding midpoint deflections of 25.5 and -24.1. These values require initial conditions with very large amplitudes if the string is to vibrate in phase-I or phase-III motion. Increasing γ_1 will constrain the $\gamma(0)$ value on the left for the phase-I transition; decreasing γ_2 will constrain the $\gamma(0)$ value on the right giving the phase-III transition. In this way, bridge termination can be used to control the string amplitude required for the phase transitions.

Now we study the free vibrations of the string about the equilibrium state. The equations of motions were solved numerically using Matlab with ode23s solver The built-in event detection algorithm in Matlab was used for detecting events for switching between the three phases of motion. Absolute and relative tolerances of 10^{-6} were used in the numerical simulations. The string is assumed to have a displacement initial condition of $y_1(x,0) = 35.35\sin(\pi x)$, which corresponds to the first mode of vibration of the unwrapped string.

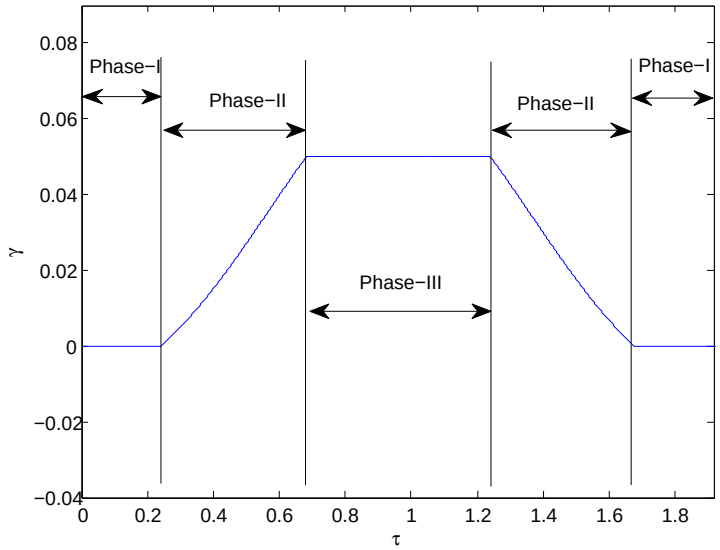

Figure 4.4: Variation of contact length with time.

Figure 4.4 shows the variation of contact length with time. The contact length γ is zero during the Phase-I motion of the string. The string starts to wrap around the obstacle in Phase-II, during which time the contact length continuously increases. Once the string completely wraps around the obstacle (i.e., when $\gamma = b$), the string enters into phase-III motion and the contact length remains constant. The string again unwraps itself and eventually returns to

phase-I motion, thus performing one complete oscillation. The string performs one complete oscillation in $\tau = 1.9231$, while the time required for one oscillation for a string without an obstacle is $\tau = 2$. The decrease in length of the string during phase-II motion explains the reason for the decreased oscillation time. Figure 4.5 shows snapshots of the string motion at the beginning and end of the Phase-I motion. A magnified view of Figure 4.5 near the obstacle is shown in Figure 4.6.

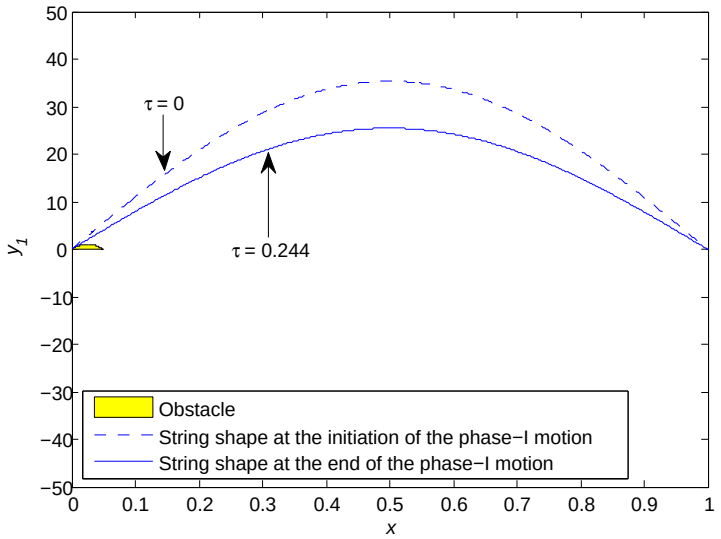

Figure 4.5: Phase-I motion of string.

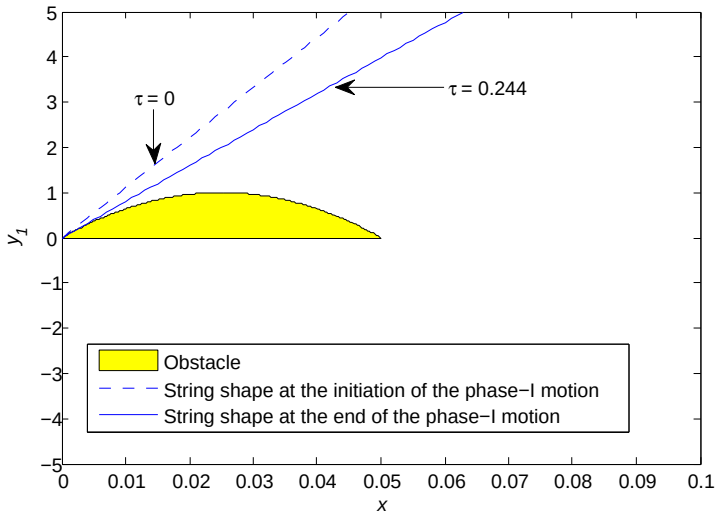

Figure 4.6: Magnified view of Phase-I motion of string near obstacle.

The string is tangential to the obstacle at $x = 0$ during the last configuration of Phase-I motion, after which the string begins wrapping around the obstacle and enters enter into Phase-II motion. The initial, in-between, and final configurations of the string during phase-II motion are shown in Figure 4.7. Magnified view of the same near the obstacle is shown in Figure 4.8.

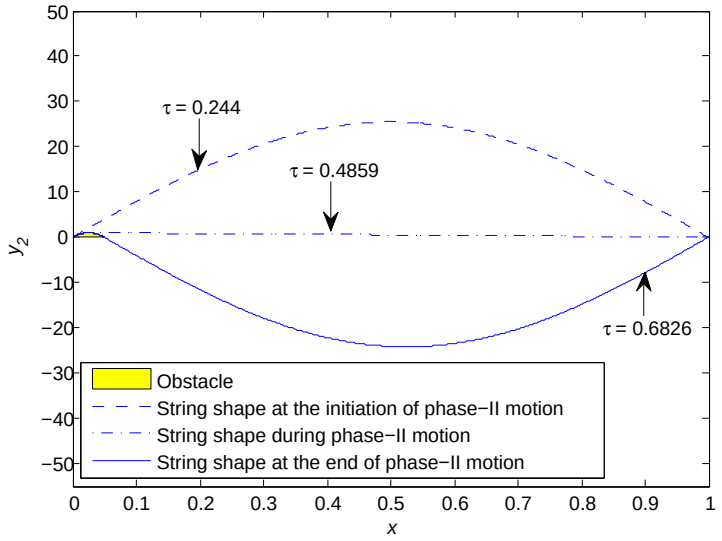

Figure 4.7: Phase-II motion of string.

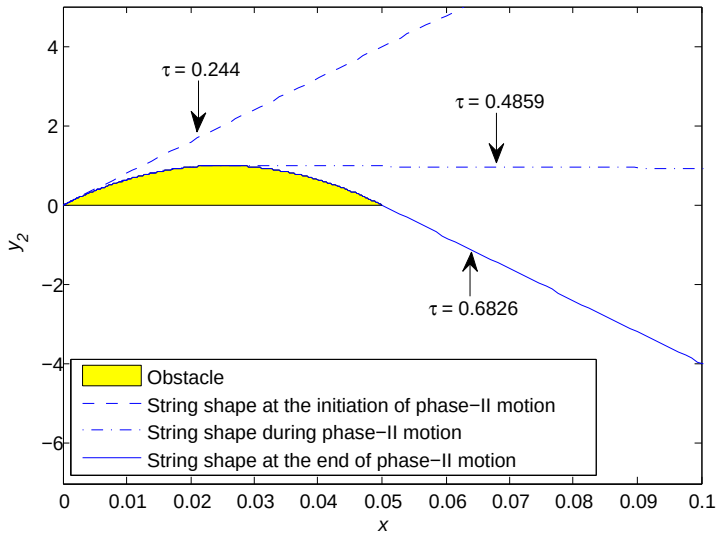

Figure 4.8: Magnified view of Phase-II motion of string near obstacle.

Once the string is again tangent to the right end of the obstacle (i.e., at $\gamma = b$), the third phase of the string motion begins. Snapshots of the string in the initial, in-between, and final configurations of phase-III motion are shown in Figure 4.9, and a magnified version of the figure near the obstacle is shown in Figure 4.10. As expected, the initial and final configurations of the string during phase-III match exactly.

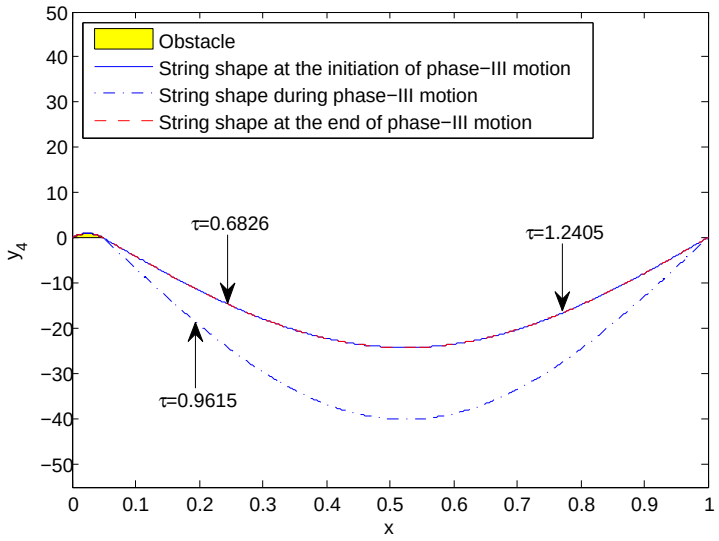

Figure 4.9: Phase-III motion of string.

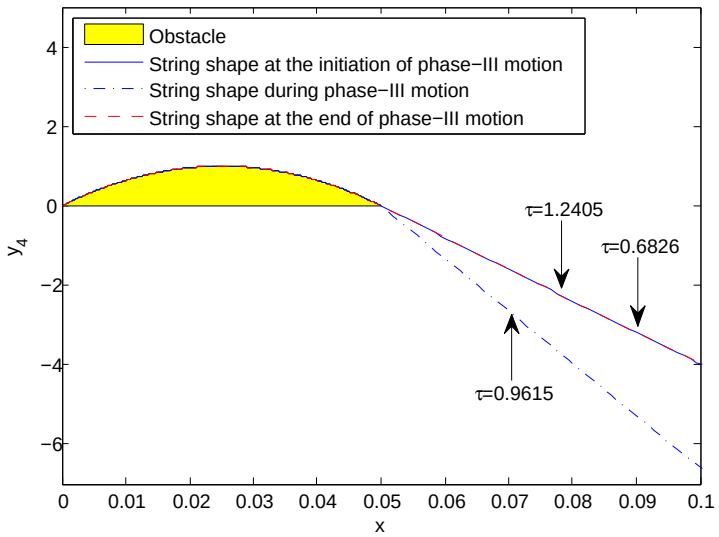

Figure 4.10: Magnified view of Phase-III motion of string near obstacle.

Figure 4.11 shows the variation of modal coordinate $\beta_1(t)$ with time for four different initial conditions. The corresponding phase space plots are given in Figure 4.12. The first initial

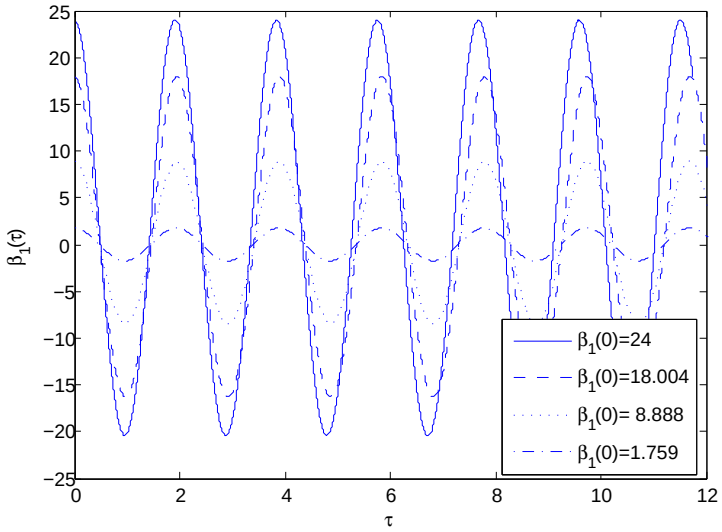

Figure 4.11: Variation of modal amplitude β_1 with time for four different initial conditions. Bridge terminations given by $\gamma_1 = 0$ and $\gamma_2 = b = 0.05$.

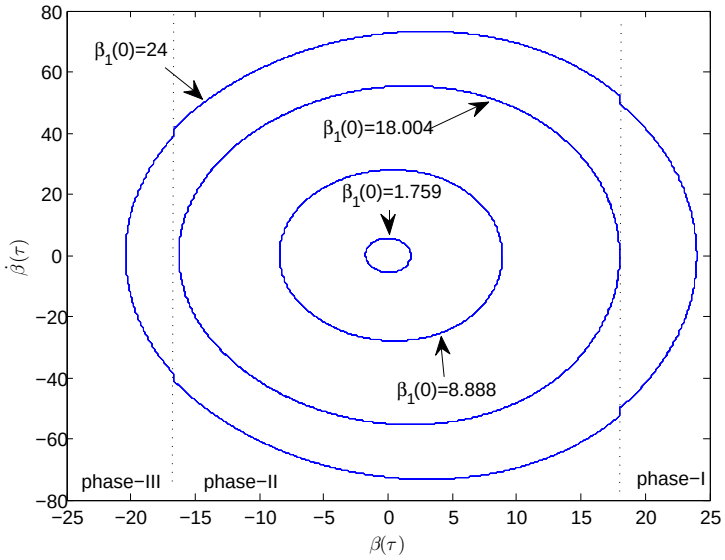

Figure 4.12: Phase space for β_1 and $\dot{\beta}_1$ for four different initial conditions. Bridge terminations are given by $\gamma_1 = 0$ and $\gamma_2 = b = 0.05$.

condition is $\beta_1(0) = 24 > 1/\sqrt{2}\pi b$ and, thus, the string starts its motion in phase-I; the

string eventually vibrates in all the three phases of motion, but the asymmetry seen in the phase plot should be noted. All the other initial conditions shown satisfy the inequalities $-4(1-b)^{3/2}/\sqrt{2}\pi b < \beta_1(0) < 1/\sqrt{2}\pi b$ and the initial string condition is in phase-II. In this case, the string remains in phase-II motion; however, this cannot be concluded in general due to asymmetry. Figure 4.11 shows that the string starting in phase-I motion has a higher oscillation frequency than that starting in phase-II, since some high frequency phase-III motion occurs during the vibration period. The frequencies of oscillation for all cases that remain in phase-II motion are essentially the same, possibly due to the near-linear relationship of $\beta_1(0)$ and $\gamma(0)$, as shown in Figure 4.3. To understand how the natural frequency of the system changes while the string wraps around the obstacle, an instantaneous natural frequency can be defined by taking a square root of the coefficient of $\beta_1(\tau)$ in equation 4.61 and dropping the rate-dependent terms. Figure 4.13 shows the variation of the instantaneous natural frequency for the same four initial conditions. It is clear that the natural frequencies are time-dependent.

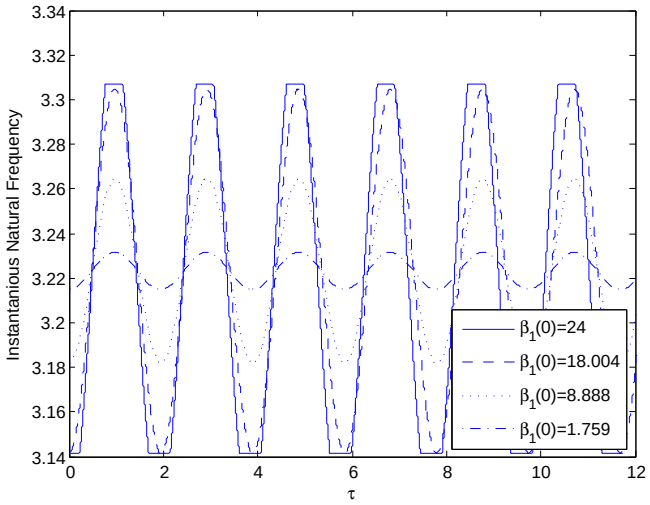

Figure 4.13: Variation of instantaneous natural frequency with time.

To validate our results with the moving boundary formulation, we compared them to those obtained using the penalty approach [71], and found good agreement only when at least 60 modes were retained in the penalty method. Moreover, the moving boundary formulation simulated the string motion 50 times faster than the penalty approach. During phase-III motion,

the slope of the string at $\gamma = b$ is discontinuous, except in the initial and final configurations. This non-smooth behaviour of the string shape at $\gamma = b$ is exactly captured by the formulation, and its discontinuous slope can be seen in Figure 4.14. This particular non-smooth behaviour

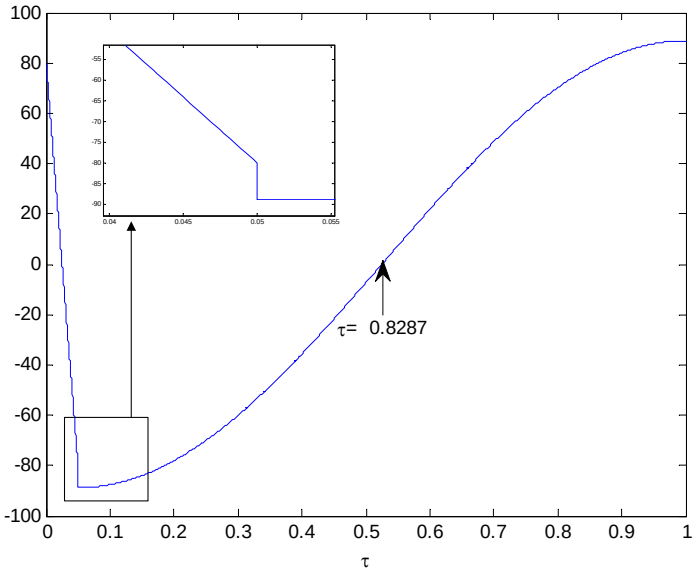

Figure 4.14: Slope of the string during phase-II and III motion.

of the string slope cannot be captured if the impact is modelled using a penalty approach [71], where the obstacle is assumed to be a linear continuum of distributed springs. Usually, a series solution is sought in terms of the normal modes of the classical string, and it is well known that the series solution converges very slowly in the presence of non-smooth displacements and is prone to Gibbs phenomenon [57]. Capturing such discontinuities exactly in the derivatives of the spatial displacement is still a challenging problem with a sparse modelling literature.[10, 57, 81]

In order to investigate the frequency components present in the string shape during phase-II motion, the shape of the string during its entire motion (obtained by solving the moving boundary problem) is projected onto the normal modes of the classical string. Mathematically:

$$y(x,\tau) = \sum_{j=1}^{N} \eta_j(\tau) \sin(j\pi x) \tag{4.114}$$

represents the shape of the string including both the wrapped and unwrapped portions. The series in equation 4.114 can also be interpreted as the series solution of the penalty approach,

for which the $\eta_j(t)$ are obtained by solving the following differential equations [71].

$$\ddot{\eta}_j(\tau) + \omega_j^2 \eta_j(\tau) = k \int_0^1 f(x,\tau)\phi_j(x)dx, \quad j = 1, 2, ..., N \tag{4.115}$$

with penalty parameter k and penetration function $f(x,\tau)$. The moving boundary approach of the present work is the limiting case of the penalty method for $k \to \infty$ and penetration function tending to zero, which corresponds to a rigid obstacle. Both methods should give the same results in the limiting case.

Figure 4.15, is a waterfall plot obtained from equation 4.114, showing the variation of normalized participation factors $a_j(\tau)$ with time for the initial condition $\beta_1(0) = 1.8$ with string motion constrained to phase-II only. The presence of a particular $a_j(\tau)$ in the waterfall

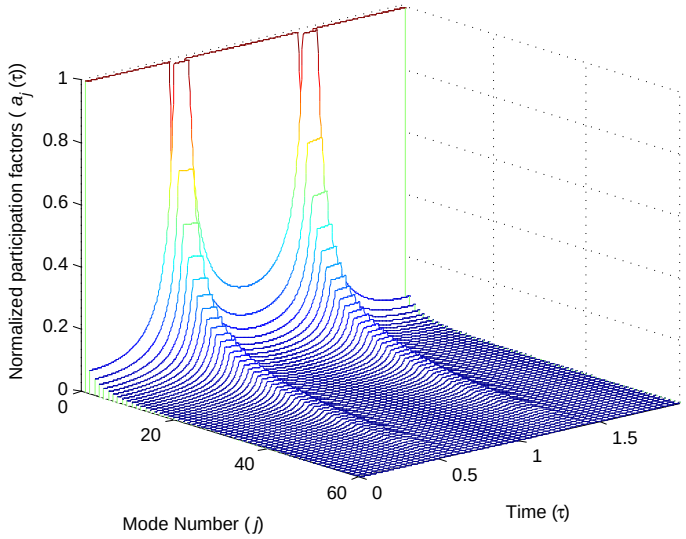

Figure 4.15: Waterfall plot showing the variation of string shape frequency components with time for motion in phase-II only.

plot means that the corresponding modal oscillator in equation 4.115 must participate in the response if the problem is solved using a penalty approach, and its frequency component will automatically be present in the time response. Figure 4.15 clearly shows the participation of higher modes during phase-II motion. Considerably more terms in the series (equation 4.114) are needed around $\tau = 0.5$ and $\tau = 1.5$, when the shape of the string demands higher-mode participation. It can be seen that equation 4.61 is highly coupled and, during phase-II motion, the modes can exchange energy. As time progresses, higher modes will start participating and

will eventually lead to multiple distributed impacts between the bridge and the string, which will violate the perfect wrapping assumption required in the moving boundary method. It is believed that these multiple impacts are responsible for the distinct tone of the sitar.

4.3.2 Simulation approximating the configuration of a sitar

An initial string deflection 24 times the height of the bridge is required for phase-I string motion with the bridge-string configuration used in the above simulations, which is the same as that of Burridge et al. [12]. This scenario is clearly impractical for a real sitar, if only because the resulting large amplitude string vibrations would have to pass through the back of the instrument. In reality, the geometry of a sitar bridge, shown in Figure 1.9, is quite different in several respects: (i) the bridge is terminated on the left at its apex, with a downbearing from the string back length keeping it fixed there; (ii) the bridge is terminated on the right at a level considerably higher than that of the far string termination; and (iii) the slope of the bridge is very shallow, so the bridge surface remains very close to the string.

Measurements obtained from the sitar shown in Figure 1.8 give the following dimensions: $B = 300\,\text{mm}$, $\Gamma_1 = 150\,\text{mm}$, $\Gamma_2 = 173\,\text{mm}$, and $L = 1060\,\text{mm}$ (the length of the string between contact point and right termination is 910 mm). We chose the straight neck of the instrument to define the horizontal direction; the x-axis for simulations (Figure 1.8) is parallel to this and passes through the far string termination, which is 14 mm above the neck reference line. The apex of the bridge at 27 mm above the neck reference line gives $h = 13\,\text{mm}$. Figures 1.8 and 1.9 show how the simulation configuration relates to the real sitar-bridge. The tops of the frets at 11 mm above the neck reference line constrain the maximum vertical displacement of the string if it is to avoid hitting them. The normal plucking point is about 200 mm from the bridge apex, giving a plucking ratio of about 2:9. A typical pluck moves the string about 15 mm horizontally and 2-3 mm vertically.

This sitar string-bridge configuration is approximated for simulations using the following non-dimensional parameters: $b = 0.283$, $\gamma_1 = b/2 = 0.142$, and $\gamma_2 = 0.163$. The initial condition for a one-mode solution requires a mid-string plucking point for which the $\beta_1(0)$ value of 0.25 is used. This initial condition corresponds to a string raised slightly above the horizontal between

the bridge termination and the pluck point, a state that is easily achieved in normal playing.[1] Substituting the non-dimensional parameters into equation 4.113 gives phase transitions for β_1 values of 0.209 (phase-I to phase-II) and -0.172 (phase-II to phase-III), corresponding to midpoint defections of 0.890 and 0.329, respectively. It can be seen that string motion in all three phases can easily be achieved for the configuration of a real sitar in normal playing, as a result of the geometry of the bridge and its terminations. The results of simulations with the above conditions, shown in the phase plot of Figure 4.16, should be contrasted with those shown in Figure 4.12.

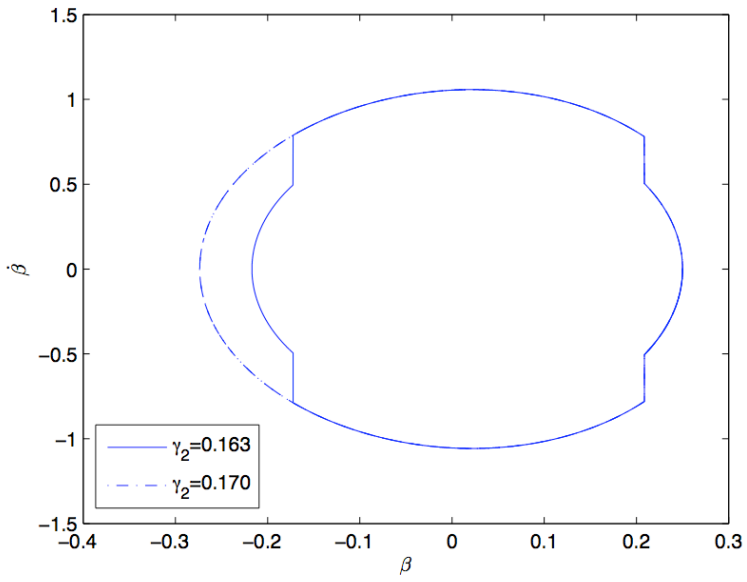

Figure 4.16: Phase space for β_1 and $\dot{\beta}_1$ with two initial conditions and simulation parameters approximating those for a sitar: $b = 0.283$, and bridge terminations $\gamma_1 = 0.142$ and $\gamma_2 = 0.163$. Also shown are results for an extra wide 30 mm bridge surface with $\gamma_2 = 0.170$.

4.3.3 Simulation results using penalty approach

The hypothesis presented in section 4.3.1, that multiple impacts between the string and the obstacle causes a buzzing tone, will be investigated using the penalty approach. The modal

[1] These comments refer to an open string. Fretting the string shortens its length and lowers the far termination about 2 mm, making only a minor difference to the vertical displacement at the normal plucking point.

equations of motion (equation 4.111) along with the contact force expression given by equation 4.109 are numerically solved in Matlab. We use the solver ode23 with absolute and relative tolerances of 10^{-7}. To validate our numerical model, we compare our modal model to the analytical results of Cabannes [13] for a string impacting a straight obstacle. Han and Grosenbaugh [39] also validated their finite difference model of a nonlinear cable with the results of Cabannes [13]. We use the initial condition of $y_0 \sin(\pi x)$, and the location of the obstacle is chosen such that $\frac{y_0}{h} = 2$. These parameters are same as those used in [39]. We consider the first 60 modes of the string in the numerical simulation. The foundation stiffness is chosen sufficiently high ($k(x) = 1.23 \times 10^6$) to simulate rigid contacts. The damping in the string and the contact model are neglected in order to compare our results for the perfectly elastic case of Cabannes [13]. The nonlinear exponent in the contact model was assumed to be unity ($n = 1$).

Figure 4.17 shows the mid-point deflection of the string when impacting a straight obstacle. It is clear from the figure that the response predicted by the modal model is a very close match to that of the analytical solution. Cabannes [13] also gave an analytical expression that relates the frequency of the string with an obstacle to that without an obstacle. The relation between frequencies is expressed as $\tau_0 = \frac{y_0+h}{2}\tau_s$, where τ_s is the frequency of the string without the obstacle and τ_0 is the frequency with an obstacle. It can be seen from Figure 4.17 that the frequency predicted by the modal result is 1.5 times the frequency of the string without an obstacle, which is consistent with the expression of Cabannes [13]. The energy in the string, the obstacle, and the total energy of the string-obstacle system is shown in Figure 4.18. The energy has been normalized with respect to the initial energy in the string (E_0). The total energy is calculated from the following expression:

$$E_{Total} = E_{String} + E_{Obstacle} \tag{4.116}$$

where $E_{Obstacle}$ and E_{String} are given by the following:

$$E_{String} = \frac{1}{2}\int_0^1 \left(\frac{\partial y}{\partial x}\right)^2 + \left(\frac{\partial y}{\partial \tau}\right)^2 dx \tag{4.117}$$

$$E_{Obstacle} = \frac{1}{2}\int_0^1 \frac{k(x)g(x,\tau)^{n+1}}{n+1} dx \tag{4.118}$$

The energy in the string is almost constant over the simulation time. Han and Grosenbaugh [39] reported an energy error of -0.079% of the initial value, while the error associated with the modal approach was found to be -0.002% for the same non-dimensional time. As shown in Figure 4.18, when the string impacts the obstacle, some of the energy of the string is transferred to the obstacle. Since the obstacle is considered to be perfectly elastic, the energy is again transferred to the string during the restitution phase of the impact.

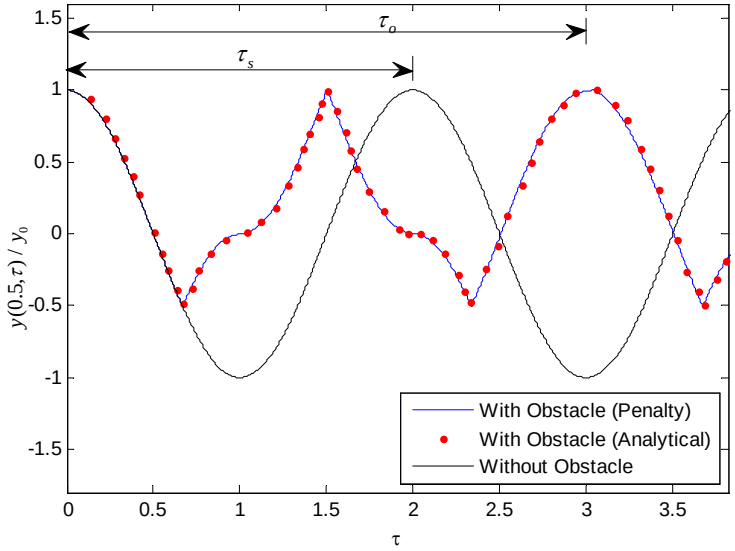

Figure 4.17: Normalized vertical displacement at midpoint of the string.

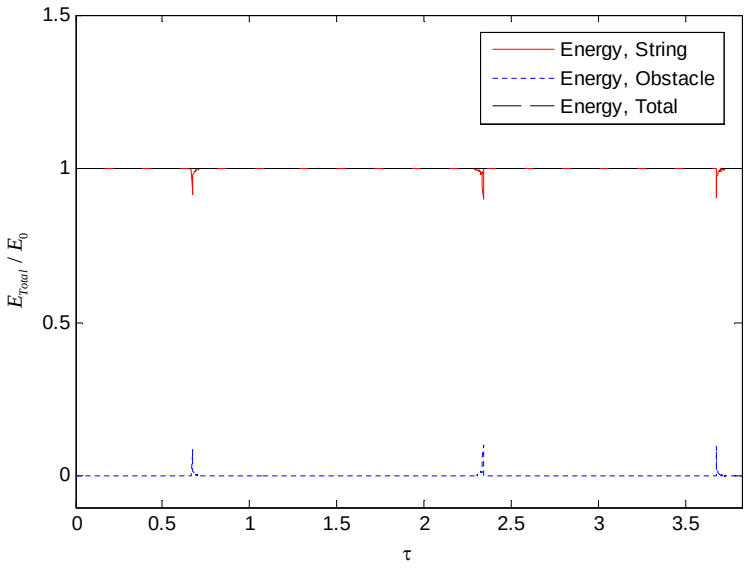

Figure 4.18: Energy of string-obstacle system.

Since the sitar string impacts a curvilinear obstacle, we also compare our results with the analytical results for the case of a sinusoidal obstacle [15]. Cabannes [15] gave a closed-form expression for string shape after the first impact, and we compare it with the numerical simulation at $\tau = 1$. Figure 4.19(a) shows the snapshots of the string motion for the initial condition $y(x, 0) = y_0 \sin(\pi x)$. It can be seen that at $\tau = 1$, the analytical expression and numerical simulation elicit the same string shape.

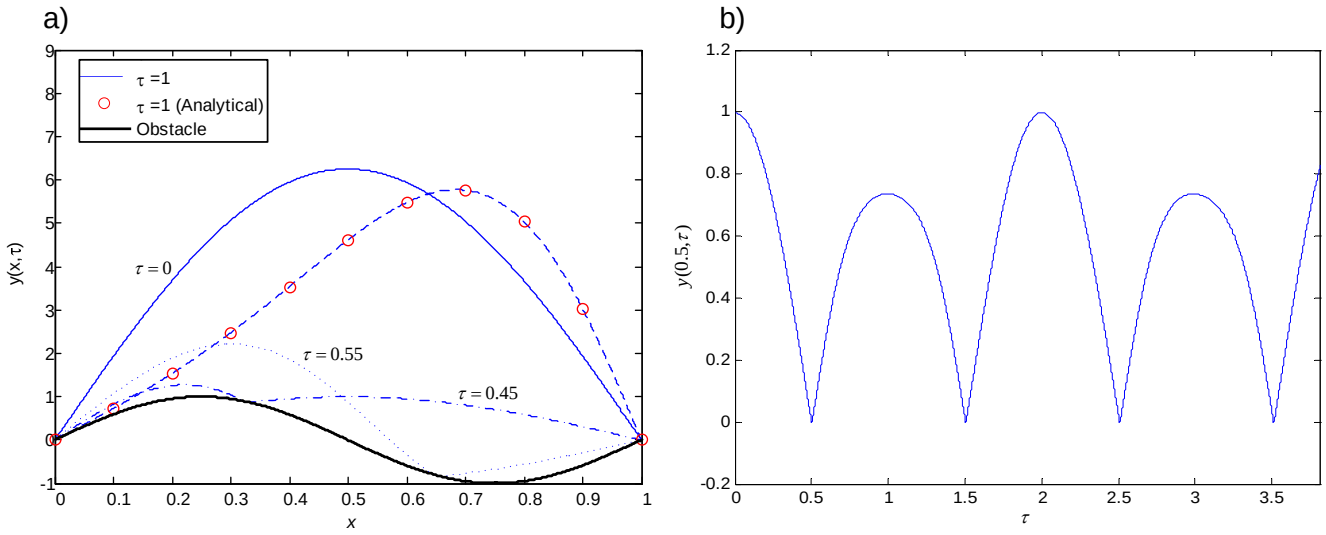

Figure 4.19: (a) Snapshots of the string motion with sinusoidal obstacle, (b) Normalized vertical displacement at mid point with sinusoidal obstacle.

4.3.4 Presence of multiple impacts during bridge-string interaction

In this section, we describe the general behaviour of the sitar string. We consider a linear elastic bridge with no loss ($n = 1$ and $\lambda = 0$). Snapshots of the string motion during one cycle for a sinusoidal initial condition are shown in Figure 4.20. The string exhibits a wrapping motion without multiple impacts for the sinusoidal initial condition, which confirms the applicability of the moving boundary formulation when the string is vibrating in its lower modes. If the simulation is carried out for long time, the coupling between the modes during the impact will lead to energy transfer between the modes, and eventually high frequency components will dominate the response. With the plucked initial condition shown in Figure 4.21, the string

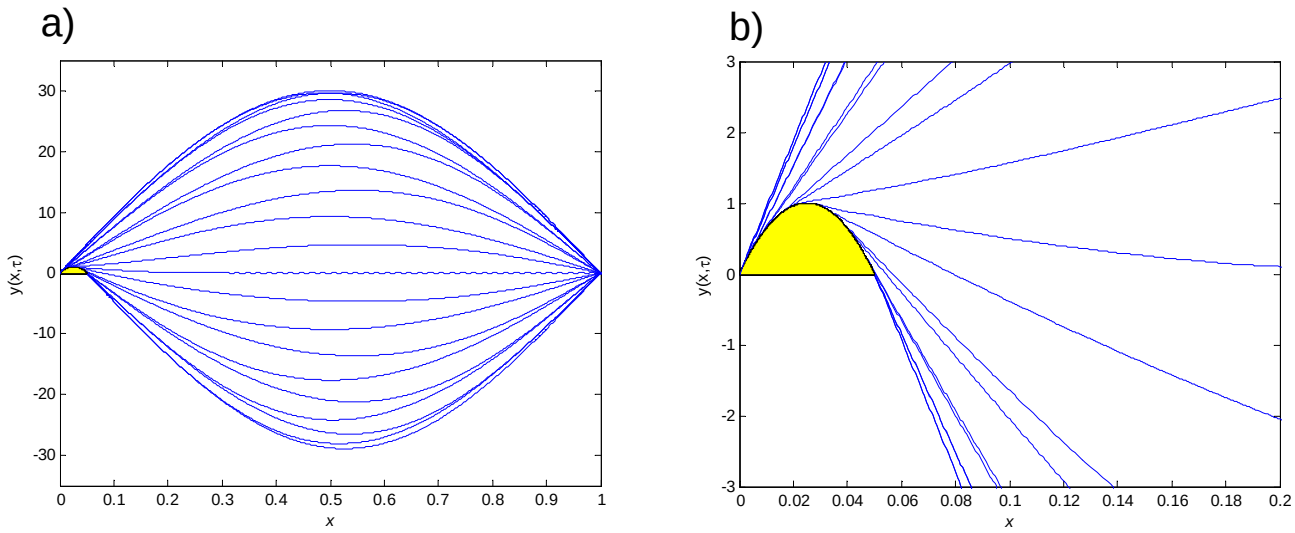

Figure 4.20: Snapshots of the string motion for sinusoidal initial condition and parabolic obstacle: (a) entire string, (b) close-up of bridge

impacts the bridge at several locations. The string is plucked at 0.1, and to represent the

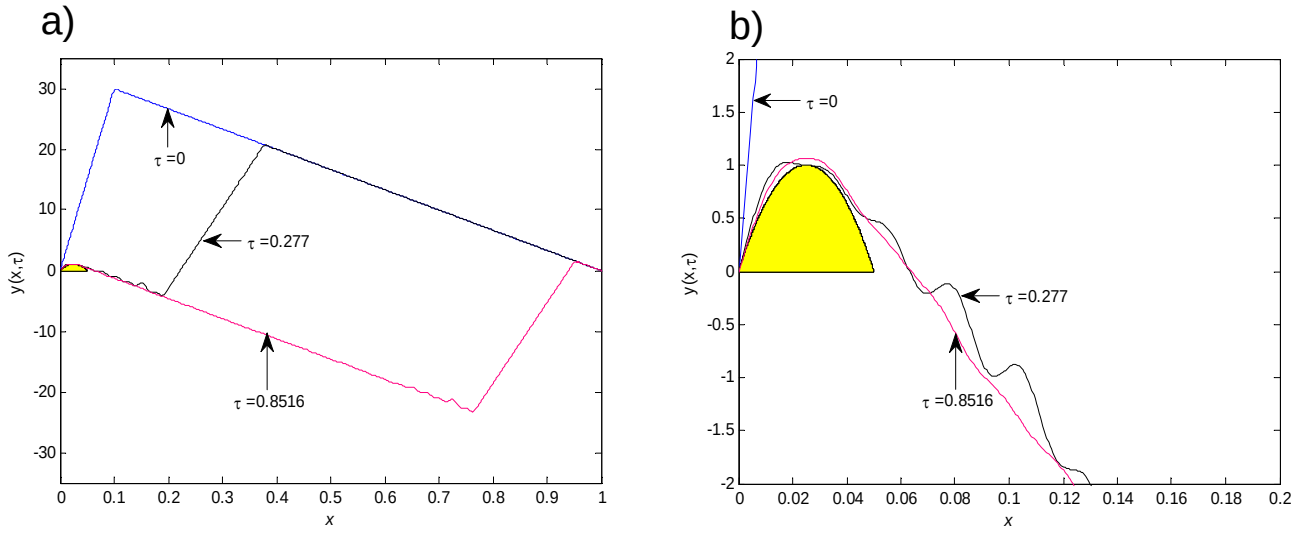

Figure 4.21: Snapshots of the string motion for plucked initial condition and parabolic obstacle: (a) entire string, (b) close-up of bridge

non-smooth shape accurately, we considered 100 modes in the simulation. Since the plucked initial condition inherently has several high-frequency components due to the non-smooth shape of the string, these high-frequency components generate multiple impacts at the obstacle. At

$\tau = 0.8516$, the string is completely airborne, indicating repetitive impacts with the bridge. The string motion is no longer considered pure wrapping in this case. This repetitive impact response is responsible for generating the buzzing tone of the instrument.

4.4 Chapter conclusions

A mathematical model of a string wrapping against an obstacle at its boundary has been formulated using a moving boundary approach. The formulation includes the distributed behaviour of a rigid bridge obstacle that may be terminated at arbitrary locations on either side. Equations of motion have been derived for the three phases of motion corresponding to the string completely (phase-III), partially (phase-II), or not at all (phase-I) wrapped on the bridge. It is shown that a single-mode moving boundary approach can reveal much of the underlying physics, including capturing the non-smooth string shape during phase-II motion. As many as 60 natural frequency components of the string are present in the wrapped string, in particular during phase-II motion. Thus, the model captures the characteristic buzzing behaviour of the sitar tone. In the simulations given, the string motion has been reasonably well represented using only a single mode, requiring the solution of only a single ODE in phase-I and phase-III motion and two coupled ODEs in phase-II. This compact formulation suggests the applicability of the method to physics-based sound synthesis algorithms. The following conclusions can be drawn on phase-II motion:

- The modal amplitude $\beta_1(\tau)$ decreases as the contact length $\gamma(\tau)$ increases.
- The frequency of oscillation of a string initially in phase-I motion is higher than that of a string initially in phase-II motion.
- The frequency of oscillation in phase-II remains constant irrespective of the initial amplitude given by modal amplitude $\beta_1(0)$.

Finally, the hypothesis of multiple impacts as the origin of the buzzing tone is confirmed by simulations from the penalty approach.

Chapter 5

Modelling the dynamics of two continuous systems impacting at a point with friction

In this chapter, we study the interaction between a rotating beam and a string. The beam model is an integral part of the piano action mechanism model, as it is used to represent the motion of the piano hammer. We briefly discuss the action mechanism models found in the existing literature. A string model is developed and integrated into the action mechanism dynamics in order to model the hammer-string interaction. The finite-time impact between the hammer head and the string is modelled using a penalty approach. Hysteresis is also included in the hammer-string interaction model. Parametric studies are conducted to understand how the hammer flexibility, the friction between the hammer and the string, and the horizontal motion (scuffing) of the hammer during hammer-string contact influence the generated tone.

5.1 Mathematical modelling

5.1.1 Action mechanism dynamic model

A procedure for constructing a multibody dynamic model of a piano action mechanism with rigid components was presented in Hirschkorn et al. [42]. This model was extended to include

a flexible hammer shank in Izadbakhsh et al. [47]. Further details, including the results of detailed experimental validation, have also been previously published [41, 45, 46]. The basic structure of the model is shown in Figure 5.1. Bodies representing the action components rotate

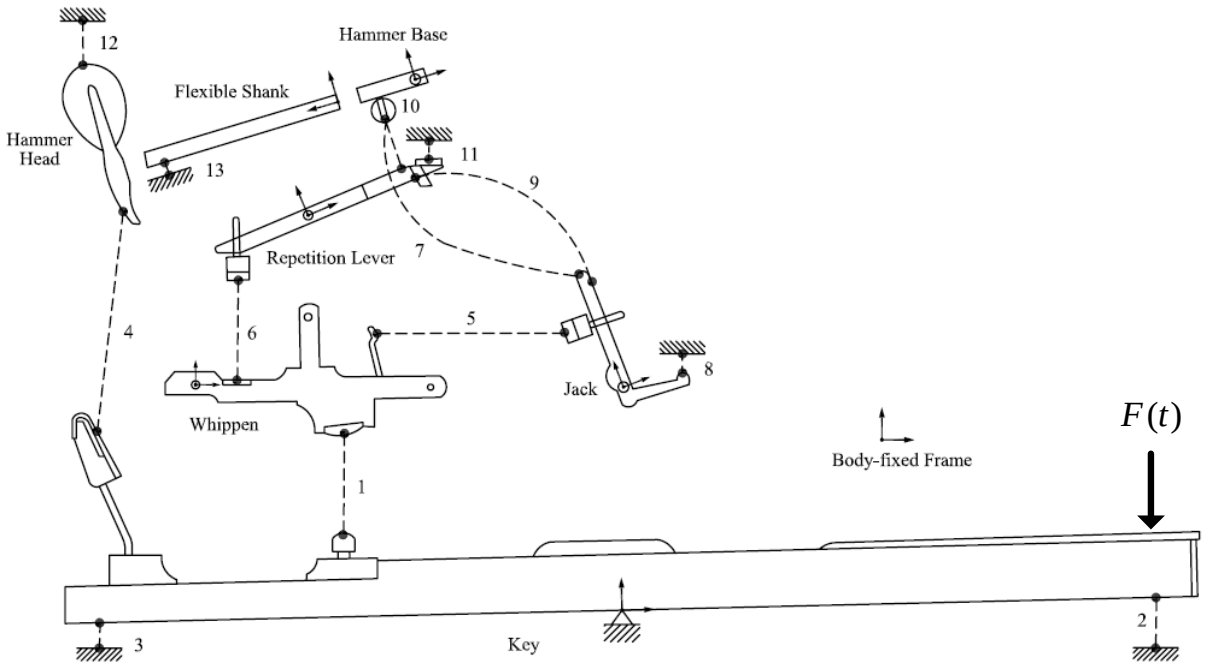

Figure 5.1: The components and the 13 contact locations between them (dashed lines) represented in the dynamic piano action mechanism model.

on pin joints (with friction), which represent the bushed pivots connecting the bodies either to the ground or to a reference frame attached to another body (such as the jack pinned to the whippen). The key, driven by a time-dependent force $F(t)$ (force profile) applied vertically downward at a location on the front surface, is assumed to rotate on a pin joint at the balance rail (key pivot). A contact detection methodology is followed to determine the dynamic interaction between the components coupled through compliant contact interfaces.

Graph-theoretic methods [52] are used to formulate the equations of motion for the rotation of the five component bodies. Due to the complexity of the equations and in order to avoid manual errors, the entire equation formulation procedure was systematically implemented using computational symbolic algebra, with the aid of the multibody dynamic modelling package

DynaFlexPro [1] in Maple.[1] One advantage of this graph-theoretic approach is that user-defined coordinates may be freely chosen for each body, allowing the convenience of a purely joint-coordinate formulation. For the rigid-component action mechanism, the system is governed by five ordinary differential equations (ODEs).

Hammer shank flexibility is included in the model by splitting the rigid hammer into three components; a rigid head and base are linked by weld joints to the ends of a flexible shank, as shown in Figure 5.1. We define two useful measures related to flexibility for the hammer: (i) hammer head tip position with respect to the ground reference frame, which is an indication of the absolute motion of the string contact point on the hammer head, and incorporates both the large-scale rotation of the base pivot as well as the effects on the head motion caused by shank vibrations and string contact; and (ii) hammer shank tip deflection which is a measure of shank bending, defined as the displacement of the tip away from the equilibrium axis of the shank. Wherever hammer head tip displacement is reported in this chapter, the undeformed position of the felt will be assumed. In reality, the actual physical tip of the hammer head may be compressed due to its interaction with the strings during contact. The flexible beam model used for the shank is based on the theory developed by Shi et al. [64, 65], which considers shear deformation (Rayleigh beam) and uses Taylor, Legendre, or Chebyshev polynomials to discretize the governing partial differential equation. A convergence study [47] concluded that three elastic coordinates are sufficient to accurately capture the flexible behaviour of the hammer shank. Therefore, the equations of motion for the rigid-component action are supplemented by three additional coupled ODEs, two of which represent the dynamics of shank bending, and the third represents the axial dynamics of the hammer.

Graph-theoretic modelling of multibody systems is a well-established methodology [51] and the exact procedure followed in generating the equations of motion for the dynamic action model has been explicitly and fully described previously. Equations generated in symbolic form have the following general structure:

$$\mathbf{M}\ddot{\mathbf{e}} = \mathbf{F} \tag{5.1}$$

where $\mathbf{M}$ is the mass matrix and $\mathbf{e} = [A_k, A_w, A_j, A_r, A_h, u_{f1}, v_{f1}, v_{f2}]^T$ is the vector of

[1] Maple is a trademark of Maplesoft, Waterloo, Ontario, Canada.

generalized coordinates, consisting of the angular positions of the key, whippen, jack, repetition lever, and hammer base, as well as the elastic coordinates that describe the state of the flexible hammer shank. The first five coordinates in **e** are angles measured counter-clockwise from the ground reference frame (or from the reference frame attached to the whippen, in the case of A_j and A_r) to the body-fixed reference frame attached to the corresponding component. The last three coordinates in **e** are the axial deformation and the two transverse elastic coordinates of the flexible shank, respectively. The right-hand force vector **F** in equation 5.1 includes quadratic velocity terms and contact forces.

5.1.2 Contact modelling

The contact model used in [41] for representing the compliant felt interfaces between components will be described in some detail, as the same approach is used in this chapter to provide a simple model of the hammer-string interaction (contact 12 in Figure 5.1). Contact detection is based on geometric proximity, with each of the two contacting surfaces defined as a line, circle, or hybrid shape that reflects the actual geometry of the component. A phenomenological model defining force versus compression characteristics was obtained empirically for each individual contacting pair of components in the action mechanism [42, 47]. The approach can be interpreted as an extension of the contact model proposed by Hunt and Crossley [43]. The experimentally-obtained loading and unloading curves determine an average fit curve:

$$f_{\text{fit}}(x) = a_f\Delta^3 + b_f\Delta^2 + c_f\Delta \tag{5.2}$$

which gives the normal force at a contact based on the inter-penetration Δ of the contact surfaces of the two bodies. Hysteresis is introduced to the contact model by including damping that is dependent on penetration velocity in the normal force f_{n} as follows:

$$f_{\text{n}} = f_{\text{fit}}(\Delta)(1 + d_f\dot{\Delta}) \tag{5.3}$$

The damping coefficient d_f is defined by:

$$d_f = \left(\frac{f_{\text{n}}(\tilde{\Delta})}{f_{\text{fit}}(\tilde{\Delta})} - 1\right) \Big/ \dot{x}_{\text{av}} \tag{5.4}$$

where $\tilde{\Delta}$ is chosen as the penetration giving the maximum difference between loading and unloading curves, and $\dot{\Delta}_{\text{av}}$ is the average velocity of the penetration observed in experiments with a real action mechanism.

Friction at the contacting interfaces has been represented using a Coulomb friction model proposed by Cull and Tucker [19], accounting for both static and dynamic friction effects. The expression for frictional force is shown below:

$$f_{\text{t}} = \mu f_{\text{n}} \tag{5.5}$$

where the coefficient of friction μ is given by the following expression:

$$\mu = A\left(\tanh(s_{\text{t}}/v_{\text{t}}) + \frac{B_1 s_{\text{t}}/v_{\text{t}}}{1 + B_2(s_{\text{t}}/v_{\text{t}})^4}\right) \tag{5.6}$$

In this smoothed version of the standard piecewise linear friction model, parameters A, B_1, and B_2 are determined through the static and kinetic friction coefficients, while s_{t} and v_{t} are relative and threshold velocities at which the slipping starts. Details on how these parameters were obtained can be found in the published model [42, 47].

It should be emphasized that an empirical force-compression fit curve, as described above, implicitly incorporates the contact surface geometry of both bodies involved and, consequently, cannot be interpreted as characterizing a unique force-compression curve for the felt interface material itself. In general, if the contact geometry of either body is changed, the force-compression curve will be different even though the compliant properties of the felt interface are maintained. This observation is of particular importance in understanding the rationale for selecting hammer-string contact parameters in the next section.

5.1.3 Hammer-string interaction

In this subsection we discuss the process of integrating a string model into the action mechanism, in place of the rigid stop used previously [42, 47]. The rigid stop was a steel plate fixed to ground and mounted above the hammer, which impacted its narrow edge (3 mm) as if it were a completely rigid string. The equation governing the transverse dynamics of an elastic stiff string, as proposed by Fletcher [27], is given by the following:

$$\rho\frac{\partial^2 Y_1}{\partial t^2} + EI\frac{\partial^4 Y_1}{\partial X^4} - T\frac{\partial^2 Y}{\partial X^2} = f_n(t)\delta_d(X - X_{hc}) \tag{5.7}$$

where Y_1 is the deformation of the string, X is the coordinate along the length of the string, L is the speaking length of the string, T is the tension in the string, ρ is the linear density, I is the area moment of inertia of the string cross-section, E is the Young's modulus, and δ_d is the Dirac delta function.

The hammer impact is modelled as an external force on the above string model. In equation 5.7, X_{hc} is the X component of the displacement $\underline{r}_{hc}$ of a point P on the hammer resolved in a frame attached at the boundary of the string, as shown in Figure 5.2. The point P is chosen

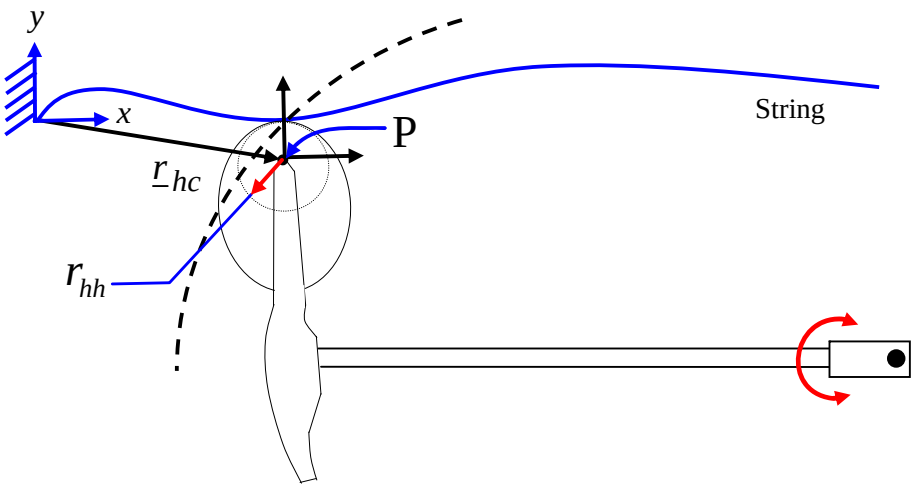

Figure 5.2: Schematic representation of the hammer and string during contact.

such that the contact surface geometry of the hammer head can be represented with a circle, which then is used for contact detection with the string represented as a line. The position X_{hc} is governed by the dynamics of the action mechanism, thereby providing a more sophisticated hammer-string interaction model than the transverse-impact hammer models [7, 9, 17, 18, 34–38, 66] in which the impact location does not change during the contact. Boundary conditions for pinned-pinned supports are as follows:

$$Y_1(0,t) = Y_1(L,t) = 0 \text{ and } \frac{\partial^2 Y_1(0,t)}{\partial X^2} = \frac{\partial^2 Y_1(L,t)}{\partial X^2} = 0 \tag{5.8}$$

The normal contact force during hammer-string impact can be represented by the general contact model described above:

$$f_{\mathrm{n}}(t) = \Upsilon(a_f\Delta^3 + b_f\Delta^2 + c_f\Delta)(1 + d_f\dot{\Delta}) \tag{5.9}$$

where $\Delta = Y_{hc} + r_{hh} - Y_1(x_{hc}, t)$ is the dynamic compression of felt during contact, parameters a_f, b_f, c_f define the empirical fit curve, d_f is the damping coefficient for (compromise) average penetration velocity, and the contact condition Υ is defined by:

$$\Upsilon = \begin{cases} 1 \text{ if } & Y_{hc} + r_{hh} \geq Y_1(X_{hc}, t) \\ 0 \text{ if } & Y_{hc} + r_{hh} < Y_1(X_{hc}, t) \end{cases} \tag{5.10}$$

As noted above, neither the hammer nor the felt are characterized by a unique empirical fit curve, since an identical hammer contacting different target bodies will, in general, produce different force-compression curves according to the different contact areas pertaining during the stages of compression.[2] The frictional force at the interface can be obtained as follows:

$$f_{\mathrm{t}}(t) = \mu f_{\mathrm{n}}(t) \tag{5.11}$$

with μ obtained from equation 5.6 as described above for the general contact model. Previously, friction between the hammer and the rigid stop was ignored [42, 47]; in this work, we consider some implications of including friction in the hammer-string contact.

A solution to the string equation 5.7 is assumed to be of the following form:

$$Y_1(X, t) = \sum_{j=1}^{\infty} \phi_j(X)\eta_j(t) \tag{5.12}$$

where $\phi_j(x)$ is the j^{th} undamped mass-normalized mode shape of the string and $\eta_j(t)$ is the j^{th} modal coordinate to be solved. Substituting the above solution and assuming the damping to be of Rayleigh form where Ξ_j is the modal damping, equation 5.7 can be reduced using orthogonality relations to an infinite number of second-order ODEs of the form:

$$\ddot{\eta}_j + 2\xi_j\omega_j\dot{\eta}_j + \omega_j^2\eta_j = \phi_j(x_{hc})f_{\mathrm{n}}(t) \tag{5.13}$$

The closed-form expressions for natural frequencies and mass-normalized mode shapes given by Fletcher [27] are as follows:

$$\omega_j = \frac{\pi}{L}\sqrt{\frac{T}{\rho}}(1 + \varepsilon\pi^2 j^2) \tag{5.14}$$

[2]The compression properties of piano hammer felt may be characterized, however, by a stress-strain curve which is independent of the properties of the target. It is difficult to use this approach to analytically derive a force-compression curve for a hammer impacting a particular non-planar target, such as a string trichord, because of the complex local loading involved as the target embeds in the hammer felt.

$$\phi_j(X) = \sqrt{\frac{2}{\rho L}} \sin\left(j\pi \frac{X}{L}\right) \tag{5.15}$$

where $\varepsilon = \pi r^4 E / 4L^2 T$ is the inharmonicity index and can be interpreted as the perturbation in the natural frequencies due to the introduction of the small bending stiffness term in the equation of motion (equation 5.7).

5.2 Results and discussion

The equations of motion (equation 5.1) were solved numerically in Matlab along with equation 5.13, discretized considering the first 40 string modes and using the customized hammer-string contact model given by equations 5.9, 5.10, and 5.11. The contact force asymptotically converged near 35 modes, with a maximum difference of 0.05 N when 35 modes were retained in the solution rather than 40 modes. We have considered 40 modes since this covers the audible frequency range. The stiff solver ode15s was used with absolute and relative tolerances of 10^{-6}. Action parameters relate to note 52 (C5) of a Boston GP-178 grand piano. All geometric and material properties, dynamic and contact parameters, initial conditions, and key input were the same as those used previously [40, 44]. The force profile from a forte blow recorded at the key surface [3] was used to provide the input function shown in Figure 5.3; values were linearly interpolated as required because the variable time steps of the solver did not correspond to the fixed sampling rate of the force measurement device.

The soundboard bridge termination of the string (on the left side in all illustrations herein) is the origin of the (horizontal) string axis; the agraffe termination is at position L on this axis. A fixed geometric relation between the string and the action is determined by the positions of the string terminations with respect to the action ground points. This is accomplished by placing the nominal (pseudo-static) hammer-string contact location at $0.88L$ on the string axis. (As will be seen, the dynamic hammer-string contact location can vary according to the flexing of the hammer shank.) Hammer blow distance (the vertical distance between the hammer at rest and the underside of the string) is the standard 47 mm. The action mechanism is arranged

[3] In this case, a pressed touch with the finger initially resting on the key was used. The character of the finger motion is actually not relevant to the model simulations, which only rely on the force profile recorded at the key surface.

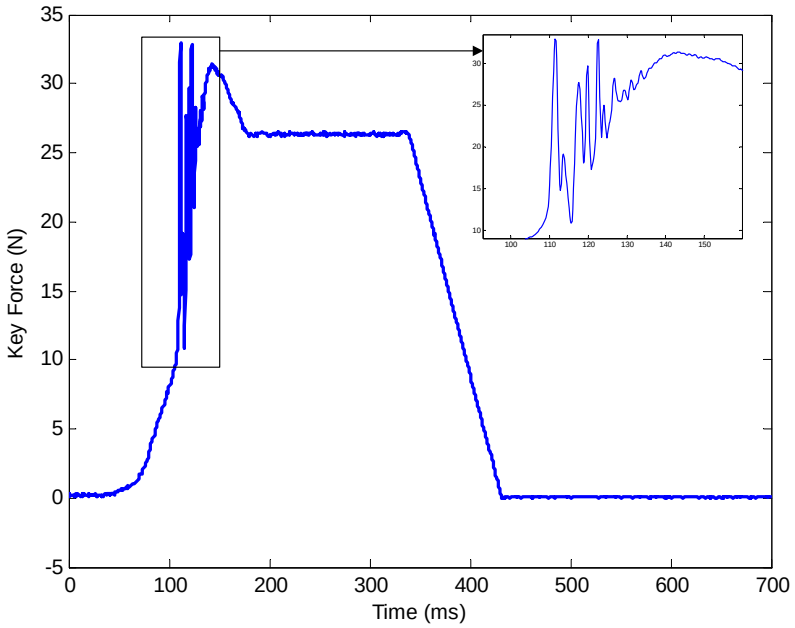

Figure 5.3: Force profile from a forte blow recorded at the key surface and used for model input.

as shown in Figure 1.7, with the key front and hammer pivot to the right side of the string contact location.

String parameters used in the present simulations, given in Table 5.1, were obtained for note 52 (C5) of a Boston GP-178 grand piano; the hammer strikes three such identical parallel strings (a trichord unison) simultaneously. We wish to examine the effect of changing only the target

Table 5.1: Physical parameters of the string.

Physical parameter	Value
Length of the string (L)	0.341 m
String tension (T)	703 N
Linear density (ρ)	0.0058 kg/m

(rigid stop vs. trichord strings) while keeping all other factors, including the hammer, identical in the simulations. However, as noted previously, hammer-string contact parameters will be different, in general, for the same hammer striking different targets. This problem has been circumvented by: (i) representing the trichord target as a single equivalent string model with

linear density and tension both increased by a factor of three, instead of three individual strings; and (ii) assuming that the stop and the triple-string present the same geometric profile to the hammer. These assumptions ensure that the same hammer force-compression characteristics can be used in each case. The hammer contact fit curve parameters in the present simulations, as well as the damping coefficient, are the same as those used previously [42, 47].

5.2.1 Validation of action and string models

The action mechanism model being used in these simulations has been experimentally validated previously [47]. The modal string model was validated by comparing simulation results to those of Bensa et al. [9], in which a space and time finite difference method (FDM) was used to solve the governing PDE. The comparison in this case was for a simple transverse impact between a single-degree-of-freedom hammer model and the string. A modal damping value of $\xi_j = 0.04$ was used in the simulation, with string parameters the same as those used by Bensa et al. [9] to validate their FDM (derived originally from Chaigne and Askenfelt[17]). Using 30 modes for the string model, the simulated hammer-string contact force (Figure 5.4) was seen to be in very close agreement with the FDM results.

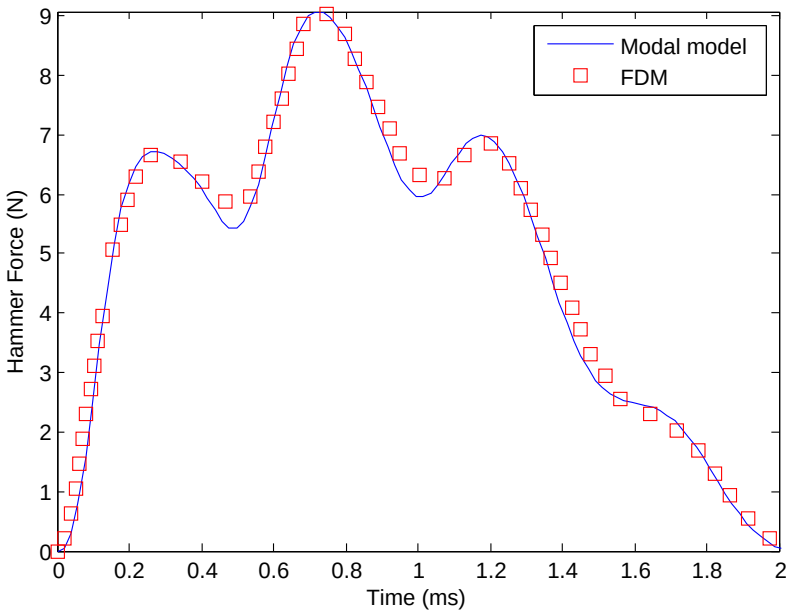

Figure 5.4: Force profile from a forte blow recorded at the key surface and used for model input.

5.2.2 Effect of string flexibility on mechanism dynamics

In this section, the behaviour of the piano action model with a flexible hammer shank is compared for string and rigid stop impacts. Friction is not included here since it was not considered previously with the rigid stop [47]. In the simulations, the hammer impact occurs about 109 ms after the force profile input begins. The post-impact response of the string is governed by the displacement and velocity immediately after the hammer-string contact.

The time-varying contact force between the hammer and the string is shown in Figure 5.5(a). Hammer contact duration (t_c) with the string is 2 ms, about 1.5 times longer than with the

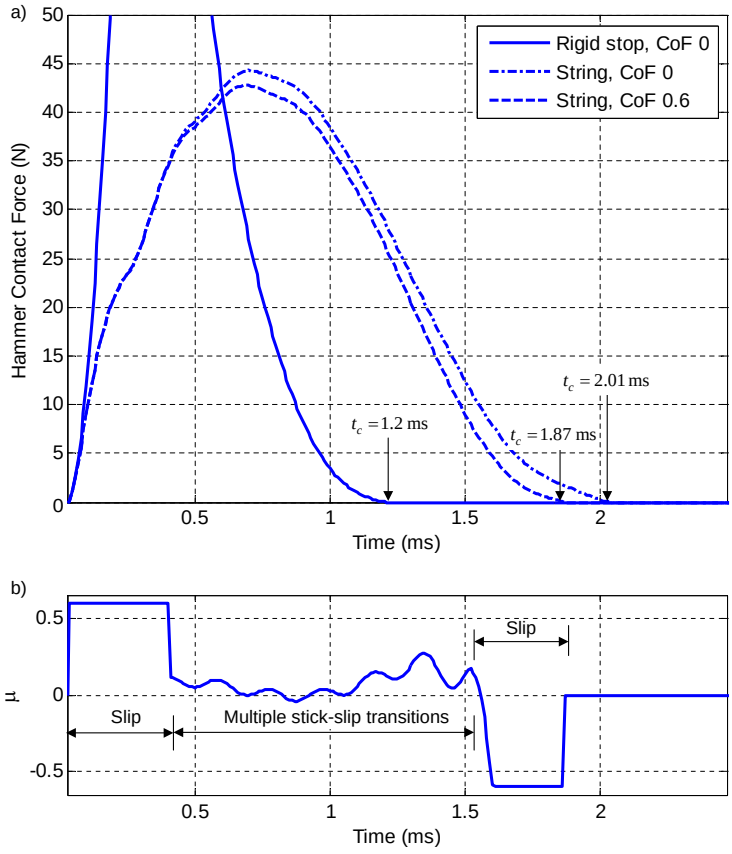

Figure 5.5: (a) Hammer contact force for rigid stop and string for varying coefficient of friction (CoF). Peak force with rigid stop impact is 95 N. Time zero corresponds to initiation of impact. (b) Variation of CoF during hammer-string impact for $A = 0.6$.

rigid stop (1.2 ms), and the peak contact force with the string (44 N) is about 50 percent of that experienced using the rigid stop (95 N). Fluctuations seen in the hammer-string force profile are

caused by pulses initiated on the string by the hammer contact, which reflect off the boundaries and return to interact with the hammer.

The rotation of the hammer base is considerably different for the two impact targets. Deflection of the string in the transverse direction results in an increase in both the hammer-string contact duration and the post-impact angular velocity, and also results in a significant reduction in the vibration of the hammer base about its pivot. The position of the hammer head is determined by the angular rotation of the hammer base as well as the flexural configuration of the hammer shank. Figure 5.6 shows that the shank vibration amplitude at the tip is reduced to about 75 percent of that experienced with the rigid stop (comparing the frictionless cases). Inspection of Figure 5.6 provides the lowest mode frequency of about 280 Hz for shank vibrations; combining this with the contact times from Figure 5.5 shows that the hammer shank executes one half-cycle of oscillation while the hammer is in contact with the string. The lack of high-frequency ripples for the string contact in Figure 5.6 can be explained as follows. The hammer experiences the same normal force as the string and it can be seen from Figure 5.5, that with a rigid stop, the hammer force more closely approximates an ideal impulse, thus exciting more of the higher modes in the response. With the flexible string, the impulse (contact force) is quite smooth and only the first vibration mode of the hammer is excited during hammer-string interaction. However, the modes are coupled due to geometrical nonlinearity in the beam model, and higher-frequency oscillations eventually appear after two cycles of hammer shank oscillation.

The scuffing motion of the hammer head along the string during hammer-string contact can be seen in the trajectory of the hammer head tip in Figure 5.7, as viewed from a reference frame attached to the string boundary. The origin in this trajectory plot is selected as the initial contact point between the hammer head tip and the string or rigid stop. As mentioned previously, it is always the undeformed position of the hammer head tip that is reported and, thus, the vertical displacement of the string will be somewhat less than that implied by the vertical hammer head tip displacement shown in the trajectory plots. In reality, the hammer head felt will have been compressed by the string during contact. In the case of the rigid stop, the implied vertical hammer head tip motion is, in fact, entirely associated with felt compression, as the stop is rigid and does not move.

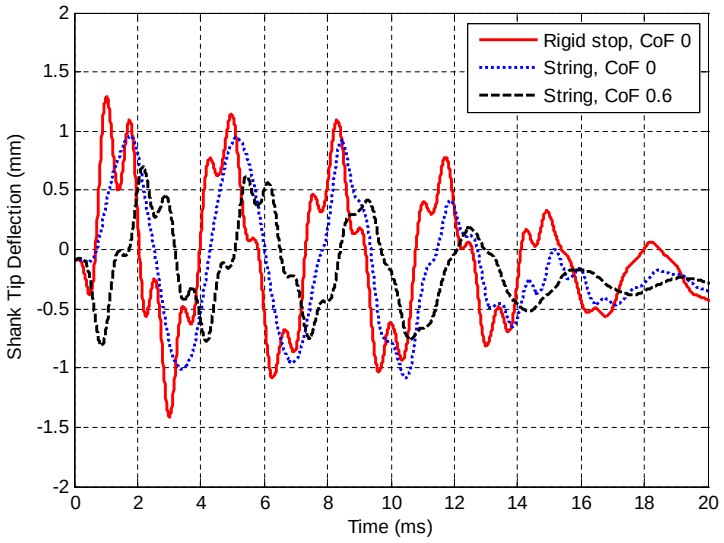

Figure 5.6: Vibration of flexible hammer shank after hammer head impact with string or rigid stop, expressed by shank tip deflection from equilibrium, for varying contact coefficient of friction (CoF). Time zero corresponds to initiation of impact.

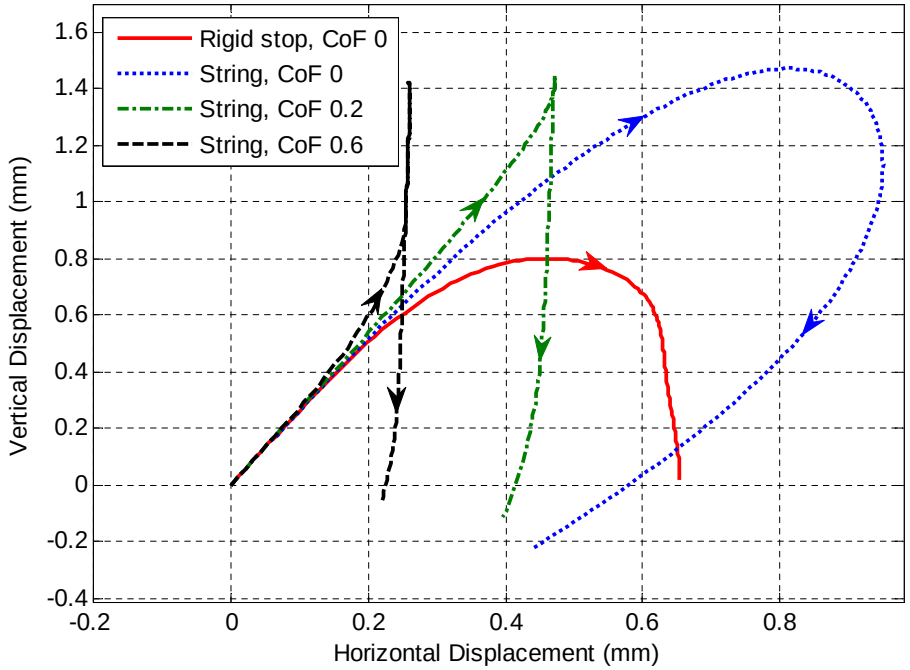

Figure 5.7: Hammer head tip trajectory during contact for string and rigid stop, for varying contact coefficient of friction (CoF). The origin is chosen to represent the initial contact point. Arrows indicate evolution of time. It should be noted that the horizontal and vertical scales are not the same.

5.2.3 Effect of hammer-string friction on mechanism dynamics

As previously mentioned, the above results do not include friction between the hammer head and the string or stop. Friction creates a force along the axis of the string, exciting the longitudinal modes of vibration; however, the present study neglects the longitudinal motion of the string, so this phenomenon cannot be modelled. Nevertheless, it is interesting to study the effect of friction on the dynamics of the mechanism and, in particular, the amplitude of hammer shank vibration and scuffing of the hammer on the string. In this subsection these effects are studied using the friction model presented in subsection 5.1.2. The model parameters were taken to be $A = \mu$, where μ is the static coefficient of friction, slipping velocity $v_t = 0.001\,\mathrm{m/s}$, $B_1 = 0$, and $B_2 = 0$ – that is, we consider only a smoothed static friction model in these simulations. A parametric study varying the CoF from 0 to 0.8 was carried out, which covers the full range of realistic values. For clarity of presentation, only the extreme cases are included in the following plots. There was also little difference between results for CoF of 0.6 and 0.8.

The variation of friction during the hammer-string contact is shown in Figure 5.5 for $A = 0.6$. During the first 0.4 ms of contact, the hammer slides on the string. The hammer then sticks to the string until 1.55 ms, after which time slipping again occurs until the end of the contact period at 1.8 ms. Due to the vibratory nature of the hammer-string contact, multiple slip-stick transitions occur between 0.4 and 1.55 ms. During this time, the relative velocity between the hammer and the string is below the stick-slip transition velocity of 0.001 m/s and can, therefore, be regarded as sticking motion (equation 5.6).

Figure 5.7 shows the hammer head tip trajectory during its contact with the string for different hammer-string coefficients of friction (CoF). It is clear that the amount of hammer head scuffing is reduced with increased CoF, as the frictional force generated at the interface prevents the hammer tip from sliding freely along the string. The scuffing footprint on the string is 0.9, 0.4, and 0.25 mm for CoFs of 0, 0.2, and 0.6, respectively. The predicted normal contact force on the hammer is slightly reduced with increasing CoF, as shown in Figure 5.5. The hammer-string contact time is also slightly reduced, possibly due to frictional energy losses in the hammer. Different CoFs determine different boundary conditions at the interface of the hammer and string, thus affecting the amount of energy transferred to the hammer to excite

its modes of vibration, as shown by the shank tip deflection for CoF of 0.6 in Figure 5.6.

5.2.4 Effect of hammer shank flexibility on string spectra

The influence of hammer shank flexibility on piano tone is well known to piano professionals who routinely select hammer shanks for different locations from treble to bass according to tap frequencies. It is also common practice to adjust the stiffness of hammer shanks, particularly thinning the treble shanks, as a means to achieve a voicing objective. Wolfenden [80] noted that, ''in respect to the recoil of hammers from string, the elasticity of the shank is of prime importance." He also pointed out that ''the bending of the shank induces a stroking action of the head upon the strings." These effects on hammer-string contact due to hammer shank flexibility have been investigated experimentally [4], and have also been proposed as a potential mechanism whereby variation in tone (string spectrum) may be achieved with different types of touch at the same dynamic level [5].

In order to study the effect of hammer-shank flexibility on string spectra, the results of the above simulations with the flexible hammer shank have been compared to those in which the stiffness of the shank is reduced by a factor of 4. For simplicity, the increase in shank flexibility was achieved by using a Young's modulus of 2.8 GPa instead of the original realistic value of 11 GPa for a hard maple shank.[4] This highly flexible shank would have the same stiffness as one where the diameter of the original shank has been reduced from 6.4 to 4.5 mm with no change to the Young's modulus. This is a significant, though by no means unrealistic, reduction in shank diameter. No other changes were made in the action and string model parameters or in the key force profile input. String damping was neglected in this comparison, since the objective was to study the spectral content of the string, and a hammer-string CoF of 0.6 was used.

For the highly flexible shank, an increased hammer head scuffing motion (0.43 mm versus 0.25 mm footprint) during string contact can be seen in the hammer head tip trajectories shown in Figure 5.8. It can also be seen that the initial contact locations are different, the

[4]In practice, a change in shank stiffness is achieved by altering geometry, in particular shank cross section (for instance, by removing material from the sides of the shank). This will, in general, also affect the inertial properties of the shank.

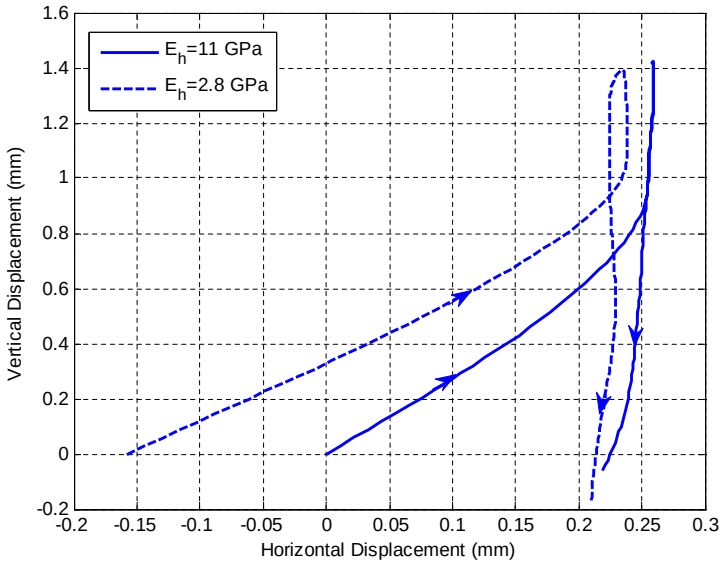

Figure 5.8: Hammer head tip trajectories during string contact for normal ($E_h = 11\,\text{GPa}$) and highly flexible ($E_h = 2.8\,\text{GPa}$) hammer shanks. The origin is chosen as the initial hammer-string contact point for the normally flexible shank. Arrows indicate time evolution. The coefficient of friction is 0.6. It should be noted that the horizontal and vertical scales are not the same.

highly flexible shank first touching the string about 0.2 mm closer to the bridge termination (to the left in the diagrams) compared to the normally flexible shank. In previous simulations (for instance Figure 4.7 of reference [44]), when compared to a rigid shank, the contact point for the normally flexible shank was already observed to shift about 0.1 mm toward the bridge termination. This shift in the contact location can be explained by the shank tip deflection shown in Figure 5.9. The highly flexible hammer shank is bent downward and away from the string before impact, thus changing the initial contact location of the hammer head. As anticipated, the vibration amplitude of the highly flexible shank is greater than that of the normally flexible shank. Finally, the contact time for the highly flexible shank is delayed by 0.2 ms, and the hammer remains in contact with the string about 0.1 ms longer, the contact period being 1.97 ms compared to 1.87 ms for the normally flexible shank. The magnitude of these predicted responses for the highly flexible hammer is consistent with reported observations in experiments with a highly flexible hammer shank [4].

Hammer shank flexibility has been seen to affect many aspects of the hammer-string contact event: contact force, initial contact time, contact location, scuffing motion, and the duration of

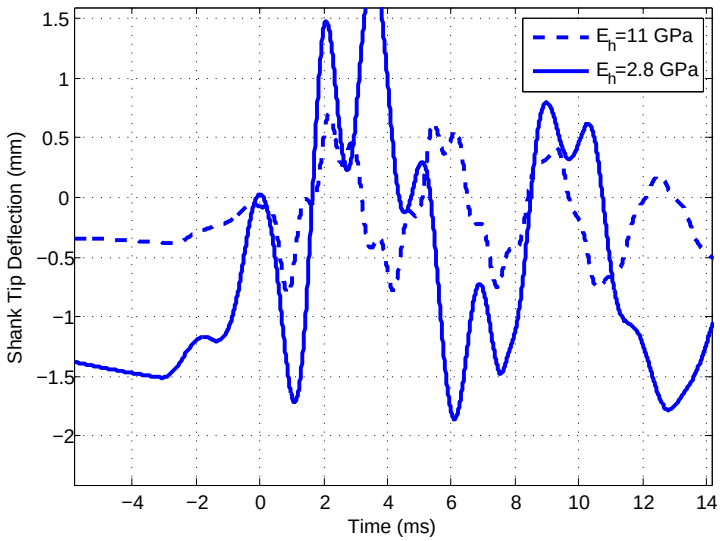

Figure 5.9: Vibration of hammer shank for normal ($E_h = 11\,\text{GPa}$) and highly flexible ($E_h = 2.8\,\text{GPa}$) hammer shanks. The coefficient of friction is 0.6. Zero time corresponds to the impact event in both cases.

contact. Consequently, it can be anticipated that the string shape (spectral content) after the hammer contact ends will also be affected by the hammer shank flexibility. This is demonstrated in the time domain plot of Figure 5.10 which shows the simulated string motion during and after impact for the two different shank flexibilities. To further demonstrate the effect of flexibility on the spectral content of the string, an explicit plot of the modal participation factors $\eta_j(t)$ taken immediately after hammer contact ends is shown in Figure 5.11. The spectra (in dB), calculated as the logarithm of the normalized absolute values $20\log\left(|\eta_j|\,/\max|\eta_j|\right)$, is shown for each of the 40 modes simulated in the string. As anticipated from the time domain string response in Figure 5.10, there are significant differences in the spectral content due to variation in the hammer shank flexibility. The fifth partial of the string is found to be very sensitive to a highly flexible hammer shank. A difference of 20 dB can be seen from Figure 5.11 with respect to a normal shank. The hammer shank vibration during the hammer-string interaction can influence the string shape at the end of hammer-string interaction, thus changing its spectral content. It will be interesting to further study in future the causal relationship between hammer shank flexibility and its influence on string spectra. Whether the observed differences in spectra would be audible cannot be ascertained from the simulated results due to the absence of damping and other relevant effects (nonlinear string motion, coupling effects between tri-chord strings, and

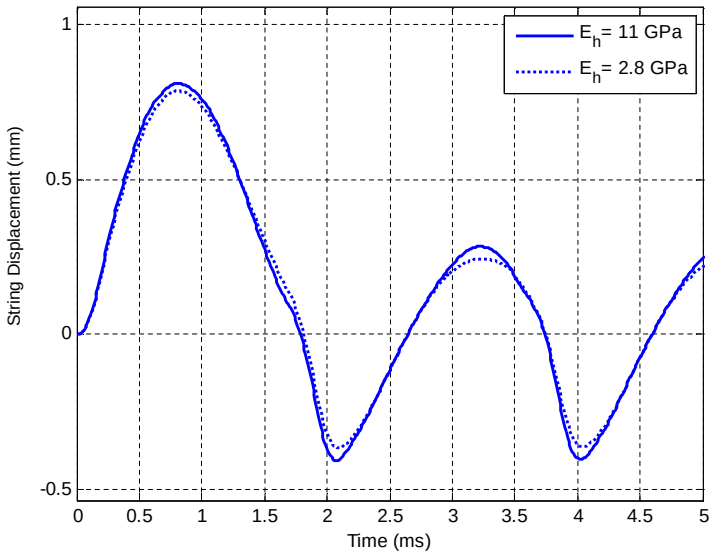

Figure 5.10: Transverse string displacement at $0.88L$ (close to the strike point) during and after hammer-string contact for normal ($E_h = 11\,\text{GPa}$) and highly flexible ($E_h = 2.8\,\text{GPa}$) hammer shanks. Time scales have been shifted for comparison; contact is initiated at the same $t = 0$ for both hammer shanks. String damping is neglected. The coefficient of friction is 0.6.

soundboard design) that could alter the perceived tonal quality in listening tests. The psychoacoustic question of spectral sensitivity is complex [16]. Differences in spectra occurring in the lower frequency portion of the response (where a distinct effect from hammer shank flexibility is observed in the simulations) are known to be more significant in the perception of tone quality [32].

This result also gives some insight into understanding the potential influence of touch on tone, which may be possible without overall change in the dynamic level by manipulating the flexural state of the hammer prior to contact. This proposed mechanism would require a reasonable degree of hammer shank flexibility and the ability to control hammer shank vibrations by touch variation.

5.3 Chapter conclusions

A dynamic model of a piano action mechanism with a flexible hammer shank and realistic compliant contacts between components has been integrated with an elastic stiff string model.

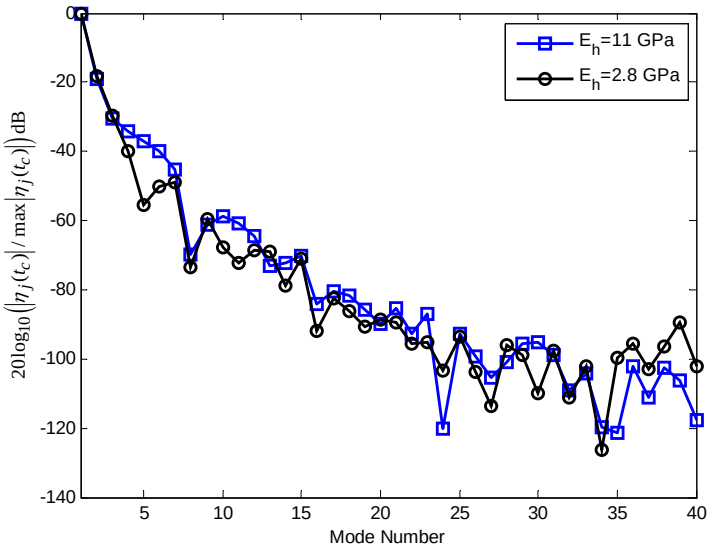

Figure 5.11: Normalized modal participation factors for the string immediately after contact for normal ($E_h = 11\,\text{GPa}$) and highly flexible ($E_h = 2.8\,\text{GPa}$) hammer shanks. The coefficient of friction is 0.6.

The effect of string motion on the mechanism has been investigated and compared to previously published results in which the hammer strikes a rigid stop. It was found that replacing the stop in the model with a string increased the extent of hammer scuffing during contact and reduced the predicted vibration of the hammer shank. Hammer shank tip deflection amplitude during contact was also reduced, while peak contact force decreased and hammer-string contact time increased. Introducing hammer-string friction into the simulations decreased the duration of contact and hammer head scuffing. Finally, simulations in which the hammer shank flexibility was increased by a factor of 4 without making any other changes to the model showed significant differences in the behaviour of the hammer and the string. For the highly flexible hammer shank, there were predicted differences in contact time, force, duration, hammer shank vibration, and scuffing motion on the string. Moreover, these differences were responsible for corresponding changes in the predicted spectral content initiated in the string by the hammer impact.

Chapter 6

Conclusions

This thesis presents new methods for modelling point and distributed contacts in continuous systems, and are applied to simulate and understand the tone generation mechanism in musical instruments. Although it is simple, the penalty method was found to be effective at simulating a wide variety of impact problems; however, it may not be the optimal choice when simulating limiting-case models such as infinite-stiffness or near-rigid impacts. We have studied the following problems related to impacts in continuous systems:

- Point impacts between a continuous system and a rigid or near-rigid obstacle without friction (Chapter 3);
- Distributed impacts in a continuous system, considering the distributed obstacle as both rigid and compliant (Chapter 4); and
- Point impacts between two continuous systems in presence the of friction (Chapter 5).

In Chapter 3, we have presented a new CoR approach for simulating impacts between a continuous system and a rigid obstacle. It was found that the existing collocation-based approaches systematically inject energy into the mechanical system that is being simulated. The proposed method based on the unit impulse response is energy-conserving, and gave results that are very close to those obtained using the penalty method. The proposed method was also found to be more computationally efficient than the penalty method, which is particularly useful when simulating near-rigid impact. The results obtained using the proposed method

were also compared to the existing experimental data from the literature; the model was found to accurately capture the qualitative behaviour of the system (period-1 motions).

In Chapter 4, we described the modelling of a distributed contact as a moving boundary problem. We analyzed a string vibrating against a rigid parabolic obstacle, which simulates the bridge-string interaction in a sitar. The moving boundary approach can effectively capture the complex shape of the string when wrapping around the bridge using only one modal coordinate (in addition to the differential equation governing the moving boundary). The method also captured the non-smooth string shape during phase-III motion. The same problem was also solved using the penalty approach, where at least 60 modes (60 differential equations) were needed to simulate the shape of the string. Once again, the approach adopted herein was found to be more computationally efficient than the existing approaches. The spectral content of the string was studied by projecting the shape of the string obtained using the moving boundary approach onto the normal modes of a classical string. Several high-frequency components were observed in the string shape. It was anticipated that these high-frequency components in the string would eventually violate the wrapping assumption, resulting in multiple impacts with the distributed bridge. The multiple impacts were believed to be the source of the characteristic buzzing tone of the sitar. To confirm the existence of multiple spatial impacts, the sitar bridge-string interaction was simulated using the penalty approach, which is more general and, therefore, is able to handle multiple spatial impacts. With a plucked initial condition, it was found that multiple impacts occur within the first few cycles (few milliseconds).

In Chapter 5, we presented a complete multibody dynamic model of a piano action mechanism with string contact. In modelling the piano hammer-string interaction, it is very important to model the finite contact time. The tone generated by the string is influenced by the contact force profile between the hammer and the string during impact. The penalty method was found to be an ideal candidate for the hammer-string interaction model, as the stiffness and damping of the piano hammer felt can be explicitly represented in the formulation. Several insights into the hammer-string interaction were obtained by replacing the rigid string in the existing action mechanism model with a flexible string, and by introducing friction. The flexible string impact was found to increase the contact duration, while the introduction of friction at the contact interface was found to decrease the amount of scuffing between the hammer and the

string during hammer-string interaction. Finally, it was shown that the frequency content of the string is significantly affected by changing the flexibility of the hammer.

6.1 Contributions

The major findings of this thesis are the following:

- A new and energy-consistent CoR-based methodology was developed for simulating point impacts in continuous systems.
- A new methodology for modelling multipoint contacts using a moving boundary formulation has been presented. The developed model was applied to study the mechanism behind tone generation in the sitar.
- For the first time, a complete multibody dynamic model for the piano action mechanism, including its interaction with a flexible string, has been developed. The developed model can be used as a tool for prototyping the piano action mechanism.

6.2 Recommendations for future work

The following are potential extensions for the research presented in this thesis:

- The coefficient of restitution method proposed in Chapter 3 can be extended to model impact between multiple continuous systems. Frictional effects can be included and the model can be used to simulate the impact between a continuous rotor and a rigid stator. The proposed model can be further extended to simulate simultaneous impacts with distributed obstacles.
- Parametric studies can be performed using the developed simulation model of a beam-stop system to predict zones of period-1 motions. Optimization studies can be done to predict the optimal coefficient of restitution that will maximize the energy dissipation. The results from the study can then be used in the design of impact dampers for continuous systems.

- The mathematical model presented in Chapter 4 can be extended to predict the 3D motion of a string. Friction between the bridge and the string can be included in the moving boundary and penalty formulations. The simulations from the resulting model can be used to understand the sitar dynamics in a more comprehensive way.

- The piano hammer-string interaction model presented in Chapter 5 can be refined in several ways. Nonlinear effects in string deformation can be included in order to predict coupling effects between the transverse and longitudinal modes. The excitation mechanism for longitudinal vibrations due to hammer-string friction can be studied. A soundboard and acoustical room model can be added to the simulation model to predict the perceived tone of the instrument.

References

[1] *DynaFlexPro User Manual, Maplesoft, Waterloo, Canada.*

[2] J Ahn. A vibrating string with dynamic frictionless impact. *Applied Numerical Mathematics*, 57:861–884, 2007.

[3] L Amerio and G Prouse. Study of the motion of a string vibrating against an obstacle. *Rend. Mat.*, 2:563–585, 1975.

[4] A Askenfelt. Measuring the motion of the piano hammer during string contact. *STL-QPSR (Deptartment for Speech, Music and Hearing KTH Sweden: Quarterly Progress and Status Report),*, 1991.

[5] A Askenfelt and E V Jansson. From touch to string vibrations II: The motion of the key and hammer. *Journal of Acoustical Society of America*, 93:2181–2196, 1993.

[6] B Balachandran. Dynamics of an elastic structure excited by harmonic and aharmonic impactor motions. *Journal of Vibration and Control*, 9:265–279, 2003.

[7] B Bank and L Sujbert. Generation of longitudinal vibrations in piano strings: From physics to sound synthesis. *Journal of Acoustical Society of America*, 117:2268–2278, 2005.

[8] Z Bao, S Goyal, L J Leu, and S Mukherjee. The role of beam flexibility and ground contact model in the clattering of deformable beams. *Journal of Dynamic Systems, Measurement, and Control*, 126:421–425, 2004.

[9] J Bensa, O. Gipouloux, and R. K Martinet. Parameter fitting for piano sound synthesis by physical modelling. *Journal of Acoustical Society of America*, 118:495–504, 2005.

[10] S Bilbao. Conservative numerical methods for nonlinear strings. *Journal of Acoustical Society of America*, 118:3316–3327, 2005.

[11] S R Bishop, M G Thompson, and S Foale. Prediction of period-1 impacts in a driven beam. *Proceedings: Mathematical, Physical and Engineering Sciences*, 452:2579–2592, 1996.

[12] R Burridge, J Kappraff, and C Morshedi. The sitar string, a vibrating string with a one-sided inelastic constraint. *SIAM Journal of Appied Mathematics*, 42:1231–1251, 1982.

[13] H. Cabannes. Motion of a string in the presence of a straight rectilinear obstacle. *C.R. Acad. Sc. Paris, Series II*, 295:637–640, 1982.

[14] H Cabannes. Motion of a vibrating string in the presence of a convex obstacle: A free boundary problem. *C.R. Acad. Se. Paris, Series II*, 301:125–129, 1985.

[15] H Cabannes. Presentation of software for movies of vibrating strings with obstacles. *Applied Mathematics Letters*, 10:79–94, 1997.

[16] A Caclin, S McAdams, B K Smith, and S Winsberg. Acoustic correlates of timbre space dimensions: A confirmatory study using synthetic tones. *Journal of Acoustical Society of America*, 118:471–482, 2005.

[17] A Chaigne and A Askenfelt. Numerical simulations of piano strings I. A physical model for a struck string using finite difference methods. *Journal of Acoustical Society of America*, 95:1112–1118, 1994.

[18] A Chaigne and A Askenfelt. Numerical simulations of piano strings II. Comparisons with measurements and systematic exploration of some hammer-string parameters. *Journal of Acoustical Society of America*, 95:1631–1640, 1994.

[19] S Cull and R Tucker. On the modelling of coulomb friction. *Journal of Physics. A*, 32: 2103–2113, 1999.

[20] J P Cusumano, M T M T Sharkady, and B W Kimble. Experimental measurements of dimensionality and spatial coherence in the dynamics of a fexible-beam impact oscillator. *Philosophical Transactions of the Royal Society of London Series A*, 347:421–438, 1994.

[21] E L B Van de Vorst, D H Van Campen, R H B Fey, and A DE Kraker. Periodic solutions of a multi-dof beam system with impacts. *Journal of Sound and Vibration*, 192:913–925, 1996.

[22] E L B Van de Vorst, M F Heertjes, D H Van Campen, A de Kraker, and R H B Fey. Experimental and numerical analysis of the steady state behaviour of a beam system with impact. *Journal of Sound and Vibration*, 212:321–336, 1998.

[23] E K Ervina and J A Wickert. Repetitive impact response of a beam structure subjected to harmonic base excitation. *Journal of Sound and Vibration*, 307:2–19, 2007.

[24] E K Ervina and J A Wickert. Experiments on a beam-rigid body structure repetitively impacting a rod. *Nonlinear Dynamics*, 50:701–716, 2007.

[25] W Fang and J A Wickert. Response of a periodical driven impact oscillator. *Journal of Sound and Vibration*, 170(3):397–409, 1994.

[26] K J L Fegelman and K Grosh. Dynamics of a flexible beam contacting a linear spring at low frequency excitation: Experiment and analysis. *ASME Journal of Vibrations and Acoustics*, 124:237–249, 2002.

[27] H Fletcher. Normal vibration frequencies of a stiff piano string. *Journal of Acoustical Society of America*, 36:203–209, 1964.

[28] CA Fulton. Playing the late medieval harp. In RW Duffin, editor, *A Performer's Guide to Medieval Music*, pages 346–354. Indiana University Press, Bloomington IN, 2002.

[29] RF Fung and YC Chen. Free and forced vibration of a cantilever beam contacting with a rigid cylindrical foundation. *Journal of Sound and Vibration*, 202:161–185, 1997.

[30] N Giordano and J P Winans. Piano hammers and their force compression characteristics: Does a power law make sense? *Journal of Acoustical Society of America*, 97:2577–2585, 1995.

[31] Y Gonthier, J McPhee, C Lange, and J C Piedboeuf. A regularized contact model with asymmetric damping and dwell-time dependent friction. *Multibody System Dynamics*, 11: 209–233, 2004.

[32] D Gunawan and D Sen. Spectral envelope sensitivity of musical instrument sounds. *Journal of Acoustical Society of America*, 123:500–506, 2008.

[33] S Yuksel M Gurgoze. On the flexural vibrations of elastic manipulators with prismatic joints. *Computers & Structures*, 62(5):897 – 908, 1997.

[34] D E Hall. Piano string excitation in the case of small hammer mass. *Journal of Acoustical Society of America*, 79:141–147, 1986.

[35] D E Hall. Piano string excitation II: General solution for a hard narrow hammer. *Journal of Acoustical Society of America*, 81:535–546, 1987.

[36] D E Hall. Piano string excitation III: General solution for a soft narrow hammer. *Journal of Acoustical Society of America*, 81:547–555, 1987.

[37] D E Hall. Piano string excitation VI: Nonlinear modelling. *Journal of Acoustical Society of America*, 92:95–105, 1992.

[38] D E Hall and A Askenfelt. Piano string excitation V: Spectra for real hammers and strings. *Journal of Acoustical Society of America*, 83:1627–1638, 1988.

[39] S M Han and M A Grosenbaugh. Non-linear free vibration of a cable against a straight obstacle. *Journal of Sound and Vibration*, 273:337–361, 2004.

[40] M Hirschkorn. Dynamic model of a piano action mechanism. Master's thesis, University of Waterloo, Canada, 2004.

[41] M Hirschkorn, J McPhee, and S Birkett. Dynamic model of a piano action mechanism. In *Proceedings of Fifth International Conference on Multibody Systems, Nonlinear Dynamics and Control (MSNDC), Long Beach CA, Sep 24-28, 2005*, pages DETC2005–84511: 12 pages, 2005.

[42] M Hirschkorn, J McPhee, and S Birkett. Dynamic modelling and experimental testing of piano action mechanism. *ASME Journal of Computational Nonlinear Dynamics*, 1(1): 47–55, 2006.

[43] K H Hunt and F R E Crossley. Coefficient of restitution interpreted as damping in vibroimpact. *ASME Journal of Applied Mechanics*, 42:440–445, 1975.

[44] A Izadbakhsh. Dynamics and control of a piano action mechanism. Master's thesis, University of Waterloo, Canada, 2006.

[45] A Izadbakhsh, J McPhee, and S Birkett. Dynamic modelling of a piano action mechanism with a flexible hammer shank. In *Proc. Fifth CCToMM Symposium on Mechanisms, Machines and Mechatronics (CSME Forum), Calgary AB, May 21-24, 2007*, pages CD–ROM: 12 pages, 2006.

[46] A Izadbakhsh, J McPhee, and S Birkett. Dynamic modeling and experimental testing of a piano action mechanism with a flexible hammer shank. In *Proc. 6th International Conference on Multibody Systems, Nonlinear Dynamics, and Control (MSNDC), Las Vegas, Nevada, Sep 4-7, 2007*, pages DETC2007–35351: 12 pages, 2007.

[47] A Izadbakhsh, J McPhee, and S Birkett. Dynamic modelling and experimental testing of piano action mechanism with a flexible hammer shank. *ASME Journal of Computational Nonlinear Dynamics*, 3(3):(031004) 1–10, 2008.

[48] J Knudsen and A R Massih. Vibro-impact dynamics of a periodically forced beam. *ASME Journal of Pressure Vessel Technology*, 122:210–221, 2000.

[49] A Krishnaswamy and J O Smith. Methods for simulating string collisions with rigid spatial obstacles. In *IEEE Workshop on Applications to Signal Processing to Audio and Acoustics. pp. 233-236*, 2003.

[50] W Lin, N Qiao, and H Yuying. Bifurcations and chaos in a forced cantilever system with impacts. *Journal of Sound and Vibration*, 296:1068–1078, 2006.

[51] J McPhee. Virtual prototyping of multibody systems with linear graph theory and symbolic computing. In *Virtual Nonlinear Multibody Systems*, pages 37–56. Kluwer Academic, 2003.

[52] J McPhee. Unified modelling theories for the dynamics of multidisciplinary multibody systems. In *Advances in Computational Multibody Systems*, pages 129–158. Springer-Verlag, 2005.

[53] Leonard Meirovitch. *Analytical Methods in Vibrations*. Prentice Hall, 1967.

[54] P Metallidis and S Natsiavas. Vibration of a continuous system with clearance and motion constraints. *International Journal of NonLinear Mechanics*, 35:675–690, 2000.

[55] F C Moon and S W Shaw. Chaotic vibration of a beam with non-linear boundary conditions. *International Journal of Nonlinear Mechanics*, 18:465–477, 1983.

[56] G O'Brien. *Ruckers – A Harpsichord and Virginal Building Tradition*. Cambridge University Press, Cambridge, England, 1990.

[57] A V Pesterev and L A Bergman. An improved series expansion of the solution to the moving oscillator problem. *Journal of Vibration and Acoustics*, 122:54–61, 2000.

[58] F Pfeiffer and C Glocker. *Multibody dynamics with unilateral contacts*. Wiley, New York, 1996.

[59] C V Raman. On some indian stringed instruments. *Proceedings of the Indian Association for the Cultivation of Science*, 7:29–33, 1922.

[60] M Schatzman. A hyperbolic problem of second order with unilateral constraints: the vibrating string with a concave obstacle. *Journal of Mathematical Analysis and Applications.*, 73:138–191, 1980.

[61] W Schiehlen and R Seifried. Three approaches for elastodynamic contact in multibody systems. *Multibody System Dynamics*, 12:116, 2004.

[62] L F Shampine, I Gladwell, and S Thompson. *Solving ODEs with MATLAB*. Cambridge University Press, Cambridge, 2003.

[63] S W Shaw. Forced vibrations of a beam with one-sided amplitude constraint: Theory and experiment. *Journal of Sound and Vibration*, 99(2):199–212, 1985.

[64] P Shi, J McPhee, and G Heppler. Polynomial shape functions and numerical methods for flexible multibody dynamics. *Mechanics of Structures and Machines*, 29:43–64, 2000.

[65] P Shi, J McPhee, and G Heppler. A deformation field for Euler-Bernoulli beams with applications to flexible multibody dynamics. *Multibody System Dynamics*, 5:79–104, 2001.

[66] H Suzuki. Model analysis of a hammer-string interaction. *Journal of Acoustical Society of America*, 82:1145–1151, 1987.

[67] T Taguti. Dynamics of simple string subject to unilateral constraint: A model analysis of sawari mechanism. *Acoustical science and technology*, 29:203–214, 2008.

[68] H C Tsai and M K Wu. Methods to compute dynamic response of a cantilever with a stop to limit motion. *Computers & Structures*, 58:859–867, 1996.

[69] J A Turner. Nonlinear vibrations of a beam with cantilever–hertzian contact boundary conditions. *Journal of Sound and Vibration*, 275:177–191, 2004.

[70] C Valette. The mechanics of vibrating strings. In J Kergomard and G Weinreich, editors, *Mechanics of Musical Instruments*, pages 115–183. Springer-Verlag, Vienna and New York, 1995.

[71] C P Vyasarayani, S Birkett, and J McPhee. Free vibration response of a plucked string impacting against a spatial obstacle. In *Proceedings of the International Conference on Theoretical, Applied, Computational and Expememental Mechanics, Kharagpur, India*, 2007.

[72] D J Wagg. A note on modelling multi-degree-of-freedom vibro-impact systems using coefficient of restitution models. *Journal of Sound and vibration*, 236(1):176–184, 2000.

[73] D J Wagg. A note on using the collocation method for modelling the dynamics of a flexible continuous beam subject to impacts. *Journal of Sound and Vibration*, 276:1128–1134, 2004.

[74] D J Wagg. A note on coefficient of restitution models including the effects of impact induced vibration. *Journal of Sound and Vibration*, 300:1071–1078, 2007.

[75] D J Wagg and S R Bishop. Application of non-smooth modelling techniques to the dynamics of a flexible impacting beam. *Journal of Sound and Vibration*, 256:803–820, 2002.

[76] D J Wagg, G Karpodinis, and S R Bishop. An experimental study of the impulse response of a vibro-impacting cantilever beam. *Journal of Sound and Vibration*, 228:243–264, 1999.

[77] C Wang and J Kim. New analysis method for a thin beam impacting against a stop based on the full continuous model. *Journal of Sound and Vibration*, 191:809–823, 1996.

[78] C Wang and J Kim. The dynamic analysis of a thin beam impacting against a stop of general three-dimensional geometry. *Journal of Sound and Vibration*, 203:237–249, 1997.

[79] C P K Wang and J Wei. Vibrations in a moving flexile robot arm. *Journal of sound and vibration*, 116:149–160, 1887.

[80] S Wolfenden. *A Treatise on the Art of Pianoforte Construction*. Gresham Books, 1916; Reprint 1975.

[81] W D Zhu and C D Mote. Dynamics of the pianoforte string and narrow hammers. *Journal of Acoustical Society of America*, 96:1999–2007, 1994.